Control of Active Nematics

Kristian Thijssen

St Hilda's College

University of Oxford

A thesis submitted for the degree of

Doctor of Philosophy

Hilary 2021

Abstract

Active matter describes systems, such as bacterial suspensions, cellular tissue or cytoskeleton biopolymers, that extract energy from their surroundings at the single-particle level and convert it into mechanical work. The resulting active work can be manifested in the form of self-propulsion and stress generation. The continuous injection of energy or activity may lead to complex, collective flow patterns and, for active materials composed of particles with nematic-like symmetry, this can produce orientational order and topological defects in the orientation field. These materials are commonly described as active nematics. An important theme in active nematic research is active turbulence, a steady-state in which hydrodynamic instabilities result in chaotic collective flows.

Using continuum simulations, we investigate how the surroundings can screen the hydrodynamics, which allows for the control of active nematics. First, by confining an active nematic between planar plates, we observe how point-like topological defects become topological disclination lines that eventually contort due to twist deformations driven by the active forces with increasing plate separation.

Another method to screen the hydrodynamics is through frictional damping of different substrates. We find the emergence of a laning state when the active nematic is subject to anisotropic friction. We show that the flow-aligning parameter, which determines reorientation to the self-generated shear flows, is important for the emergence of this flow state. We investigate the flow-aligning parameter further and uncover regimes where self-propelled defects are mutually bound. We also show that weak defect-defect ordering exists in active turbulence, and we demonstrate that defects can exhibit co-operative defect-defect interactions that span many defect pairs by varying global friction. Finally, we show that we can control the active material's defect, flow and concentration dynamics through position-dependent friction.

The work in this thesis will allow future research to extend knowledge on bulk active nematics to more complex biophysical systems.

This thesis is dedicated to my parents,
Judit and Stefan Thijssen.

Mum, I couldn't have done this without your support. I am so sorry for all the stress I have caused you. I truly appreciate and love you.
To my deceased father, I wish you could have been here. Your memory inspires me. I know if you were still here, you would have motivated me to produce even more high-grade work. You could always encourage me. And maybe you would even have tried to compete with me in obtaining your own Doctorate degree. I miss you.

Mam, zonder jou steun had ik dit niet kunnen doen. Het spijt me echt van alle stress die ik jou hebt veroorzaakt. Ik waardeer je echt en hou van je.
Aan mijn overleden vader, Ik wou dat je hier kon zijn. Mijn herinnering aan jou heeft mij enorm geïnspireerd. Ik weet dat als je hier nog was, dan zou jij mij hebben gemotiveerd om nog veel beter werk te leveren. Je bleef me altijd aanmoedigen. En mogelijk had je samen met mij geijverd voor je eigen doctoraat. Ik mis je zo.

Acknowledgements

In the first place, I would like to thank my supervisor Julia Yeomans for welcoming me into her research group, and for her continued guidance and support during all this time. Julia, thank you for taking a chance with me during my internship five years ago and for allowing me to grow as a researcher. I am grateful for all the opportunities you offered me, which allowed me to explore and develop my own research interests. It has been a privilege to know you, and work with you.

This thesis would not have been possible without Amin Doostmohammadi and Tyler Shendruk. Both of you pushed me forward and inspired me to stay in academia. Amin, you have provided me with countless ideas, and I always appreciated your viewpoint of my work. Tyler, you have encouraged me to trust my own judgement and help me put things into perspective. I am truly grateful to call both of you my friends.

I would also like to thank the members of the Yeomans group, particularly Luuk Metselaar, Rian Hughes, Saeed Mahdisoltani, Tunrayo Adeleke-Larodo, Guanming Zhang, Mehrana Nejad, Liam Ruske, Andrew Orr and Muriel van der Laan. I really enjoyed our social meetings and truly loved discussing science during the coffee breaks. A lot of the research in this thesis started from those fruitful discussions.

Thanks are also due to my collaborators and everyone in LubISS, particularly Doris Vollmer.

I would also like to thank all the people who proofread parts of this thesis. I am sorry for the quality you had to read and the work I made you do. My thesis's quality would not have reached its current level without the help of Rian Hughes, Mehrana Nejad, Liam Ruske, Saeed Mahdisoltani, Conor Wild, Sophia de Medeiros, Tom Gawne, Harry Anderton, Tyler Shendruk and Amin Doostmohammadi. I would also like to thank Julia Yeomans for her help. The most heartfelt appreciation goes to Henk van Leeuwen. Your immense help pushed me through the difficult parts of writing this thesis. I could not have done this without your support.

My time in Oxford would not have been the same without the friends I made through OURPGSoc. I enjoyed all the DnD and roleplaying, which gave my chaotic side a creative outlet. I think it was one of the few things that has kept me sane.

I want to thank Paul van der Schoot for introducing me to the field of soft matter all those years ago, which has kept me interested in physics.

Lastly, I would like to thank my family for supporting me, particularly my grandmother Berti Thijssen and my deceased grandfather Piet Thijssen.

Publications

Authored publications contributing to this thesis

- T.N. Shendruk*, K. Thijssen*, J.M. Yeomans, and A. Doostmohammadi (2018). Twist-induced crossover from two-dimensional to three-dimensional turbulence in active nematics, *Physical Review E*, 98 (1), 010601.
- K. Thijssen, J.M. Yeomans, L. Metselaar and A. Doostmohammadi (2020). Active nematics with anisotropic friction: the decisive role of the tumbling parameter, *Soft Matter*, 16 (8), 2065-2074.
- K. Thijssen, J.M. Yeomans, and A. Doostmohammadi (2020). Binding self-propelled topological defects in active turbulence, *Physical Review Research*, 2 (4), 042008.
- K. Thijssen, M.R. Nejad, and J.M. Yeomans (2020). Role of Friction in Multidefect Ordering, *Physical Review Letters*, 125 (21), 218004
- K. Thijssen*, D. Khaladj*, M.A. Gharbi, S. Fraden, J.M. Yeomans, L.S. Hirst, and T.N. Shendruk (In preparation). Submersed Micropatterned Structures Control Active Nematic Flow, Topology and Concentration.

* Denotes co-first authors

Contents

1 Introduction **1**

2 Passive and active nematic liquid crystals **9**

2.1 Liquid crystals . . . 10

2.1.1 Nematic order parameter . . . 10

2.1.2 Emergence of nematic ordering . . . 13

2.1.3 Biphasic liquid crystals . . . 17

2.1.4 Discontinuities in the orientation field . . . 18

2.2 Continuum model . . . 22

2.2.1 The convection-diffusion equation . . . 22

2.2.2 The Navier-Stokes equations . . . 23

2.2.3 The Cahn-Hillard equation . . . 24

2.2.4 Isotropic viscosity . . . 24

2.2.5 Implementation of the model . . . 25

2.3 Active nematics . . . 25

2.3.1 Individual swimmer . . . 26

2.3.2 Active stress . . . 27

2.3.3 Intrinsic nematic ordering . . . 28

2.3.4 Active nematic instabilities . . . 30

2.3.5 Active defects . . . 31

2.3.6 Active turbulence . . . 33

2.4 Conclusion . . . 35

3 Twist-induced crossover from two-dimensional to three-dimensional turbulence in active nematics **37**

3.1 Introduction . . . 37

3.2 Simulation method . . . 38

3.3 Quasi 2D active turbulence . . . 40

3.4 3D active turbulence . . . 41

3.5 Twist instability . . . 43

3.6 Energy competition . . . 45

3.7 Conclusion . . . 48

4 Active nematics with anisotropic friction: the decisive role of the flow-aligning parameter **49**
4.1 Introduction . . . 49
4.2 Simulation method . . . 50
4.3 Emergence of laning in the flow-aligning regime . . . 51
4.4 The flow-tumbling regime . . . 56
4.5 A state of oppositely-charged bound defect pairs . . . 59
4.6 Discussion . . . 61
4.7 Conclusion . . . 63

5 Binding self-propelled topological defects in active turbulence **65**
5.1 Introduction . . . 65
5.2 Simulation method . . . 66
5.3 Formation of full-integer vortex-like topological defects . . . 67
5.4 Formation of full-integer aster-like topological defects . . . 69
5.5 Quantifying full-integer defects . . . 70
5.6 Conclusion . . . 74

6 The role of friction in multi-defect ordering **75**
6.1 Introduction . . . 75
6.2 Simulation method . . . 76
6.3 Defect distributions . . . 77
6.4 Emergent defect ordering at low friction . . . 79
6.5 Defect lattices at high friction . . . 79
6.6 Conclusion . . . 83

7 Submersed micropatterned structures control active nematic flow, topology and concentration **85**
7.1 Introduction . . . 85
7.2 Simulation method . . . 86
7.3 Submersed trench . . . 88
7.4 Submersed stairway . . . 94
7.5 Submersed pillar . . . 96
7.6 Conclusion . . . 100

8 Discussion **101**
8.1 Summary . . . 101
8.2 Outlook . . . 103

Appendices

A The hybrid lattice Boltzmann method **109**
A.1 The hybrid lattice Boltzmann method . . . 109
A.2 Wall boundary conditions . . . 112
A.2.1 Flow field boundary conditions . . . 112
A.2.2 Director field boundary conditions . . . 113

B Defect detection **115**
B.1 Topological defects . . . 115
B.2 Disclination lines . . . 115

C Additional comments and measurements **117**
C.1 Inclusion of Landau-de Gennes free energy . . . 117
C.2 Flow field around bound defects . . . 118
C.3 Axis of flow deformation . . . 118
C.4 Dominant forces around bound defects . . . 121
C.5 Statistics of the orientation distribution function . . . 122
C.6 Finite-size effects of the orientation distribution function . . . 122
C.7 Additional depletion geometries . . . 123

Bibliography **125**

List of Figures

1.1 Schematic of the active microtubule system. 5

2.1 Schematic of various possible phases of matter. 11
2.2 Schematic representation of the three modes of bulk director deformations: bend, splay and twist. 16
2.3 Schematic representation of the planar projection of a disclination line to a normal plane. 18
2.4 Schematic illustration of topological defects in nematic liquid crystals. 19
2.5 Schematic of self-propelled particles. 27
2.6 The analytical local flow $\vec{v}$ (orange arrows) around half-integer defects in an extensile system for: 33
2.7 Snapshots of simulation results showing meso-scale turbulence in an extensile active nematic. 34

3.1 Transition to 3D active turbulence. 39
3.2 Comparison of turbulence properties in 2D and full 3D simulations. 41
3.3 Quantifying disclination line behaviour. 42
3.4 The average projected distance $\langle\sigma\rangle$ between the ends of the disclinations as a function of activity number A 43
3.5 The contortion of disclinations are highly correlated to twist deformations. 44
3.6 Schematic of a twisted disclination line. 47
3.7 The average projected distance $\langle\sigma\rangle$ between the ends of the disclinations as a function of modified activity number A' for varying twist K_{Twist} and bend/splay K elastic constants. 48

4.1 Emergence of laning with increasing friction in the flow-aligning regime. 52
4.2 Flow-aligning regime. 53
4.3 Characterising the laning state at intermediate friction 55
4.4 Varying the flow-aligning parameter. 57
4.5 Flow-tumbling regime. 58
4.6 Bound defect pairs at low activities. 60
4.7 Wind roses of the different states. 62

5.1 Emergence of bound defect pairs. 67
5.2 Analytical prediction of director reconfiguration in response to active flows of +1/2 defect pairs. 69
5.3 Numerical measurements of the bound defect density as a function of (a) activity and (b) flow-aligning parameter. 71
5.4 Stability diagram of bound defect density. 72
5.5 Further quantifying bound defect state. 73

6.1 Defect ordering in wet active turbulence. 77
6.2 Defect structures at intermediate friction. 80
6.3 Ordering around a +1/2 defect at high friction. 81
6.4 Ordering around a −1/2 defect at high friction. 83

7.1 Submersed micropatterns control active nematic dynamics. 87
7.2 Positive defects depleted at the trench interface. 89
7.3 Friction boundaries result in separate flow regions. 93
7.4 Submersed micropatterned stairway allows simultaneous coexistence of regions of separated active turbulence with differing defect densities. 95
7.5 Pillars cause local high friction regions which result in active matter depletion. 98

A.1 The lattice geometry and lattice vectors $\vec{e}_i$ (green arrows) for the D3Q15 grid used in our lattice Boltzmann model. 110
A.2 Schematic representation of the bounce-back algorithm. 112
A.3 Schematic representation of the full-slip boundary. 112

B.1 Detection of disclination lines. 116

C.1 The measured average flow profile around: 119
C.2 Analytical prediction of director reconfiguration in response to active flows of +1/2 defect pairs in the limit of $\nu \to \pm\infty$. 120
C.3 The average dominant forces around bound defects 121
C.4 Orientational distribution function S_{++} along the x-axis with the associated error for $F = 0.023$. 122
C.5 Nematic order of the defects S_d as a function of friction for different system sizes L. 123
C.6 Rectangular pillar causes depletion. 124
C.7 We consider a circular pit where frictional damping 124

They asked me how well I understood theoretical physics. I said I had a theoretical degree in physics. They said welcome aboard.

Fallout: New Vegas

1 Introduction

The world is filled with life forms that consume energy to move and exert forces on their surroundings. These living organisms are found over a diverse range of scales, extending from creatures like birds and fish, all the way to microscopic cells like bacteria and algae. While the living entities' propulsion method depends on their size [1], all these organisms are driven out-of-equilibrium, as they *actively* transform internal energy into motion.

The motion patterns of active organisms tend to be disordered, and they are often uncorrelated when diluted. On the other hand, when individuals are packed closely together, collective behaviour tends to emerge. These collective dynamics range over many times the individual particle size and are found at a plethora of length scales from macroscopic systems, *e.g.* flocks of birds [2] and schools of fish [3] to microscopic regimes, *e.g.* motile cells like *E. coli* [4–6], cellular monolayers [7–9] and subcellular filaments [10–13]. These living flows are also interesting as the collective dynamics emerge due to the individually active, constituent particles dissipating energy into the system. The resulting collective motion arises spontaneously without any external field or geometrical constraint guiding the process. It emerges as a consequence of the interactions between individuals, which cause spontaneous breaking of the continuous orientation symmetry. Condensed matter physicists describe this collective motion as an orientationally ordered phase of *active matter*.

In this collective motion, we find the emergence of non-trivial and novel flows, making active matter an exhilarating physical system for studying.

We find this symmetry-breaking on a variety of length scales. This suggests the existence of some universal features which cause the collective motion of active matter to emerge. These features are found in many different biological specimens, regardless of their individual-level details. This observation allows us to study many biophysical systems as active matter using a reductionist approach and leads to the creation of minimum models that can be applied to various biological systems to provide insight into their collective dynamics.

The Vicsek model was one of the earliest computer implementations of such an approach [14, 15]. This model was initially used to describe a macroscopic flock of birds using interacting particles. The particles have a fixed speed and prefer to align their velocity vectors parallel to their neighbours. Flocking can emerge in this model, capturing the collective behaviour of birds. Later, Toner and Tu used the symmetry rules of the Vicsek model to generate continuum equations of motion for general active matter [16–18]. Through this model, they studied the universal features of flocks driven by the individual particles' inertia. They captured the dynamic properties of active matter consisting of densely packed and self-propelling constituents, called *active fluids*.

However, the traditional Toner and Tu model operates on the macroscale where inertia dominates. At microscopic scales, the organisms experience a different Reynolds number as the fluid becomes viscously dominated. In order to propagate in this Stokes regime, swimmers have adopted temporally asymmetric means to propagate [1]. These propagation methods can result in far-field hydrodynamic interactions between the particles [19], which allow for distinct kinds of collective dynamics compared to the macroscale. While the far-field hydrodynamic flows complicate the equations of motion, they also justify the general study of microscopic active fluids. The far-field interactions allow us to ignore many of the microscopic details of the individual particles considered. This approach's generality and its independence of particle details allow us to apply lessons learned from microscopic

active fluids to many different biophysical systems. Hence, studying these active fluids is relevant for different fields, *e.g.* medical, food and microbial ecology sciences.

On a coarse-grained level, these hydrodynamic interactions lead to shear stresses that stir the active fluid [20]. The shear stresses result in instabilities that drive the active fluid to exhibit complex, collective flow patterns which also display local particle orientation [10, 21–23]. Indeed, an increasing number of biologically active systems including colonies of rod-shaped bacteria [4–6], cellular monolayers [7–9], and subcellular filaments [10–13] display orientational order and topological defects: singular points in the orientation field that resemble nematic liquid crystal features. These materials are commonly described as *active nematics* [18, 21, 24].

The topological defects are topologically protected structures, as no local rearrangement of the order parameter can remove them, similar to those found in passive nematics [25]. Despite this, the topological defects of these living biological materials show distinct dynamical behaviours compared to their non-living counterparts [18, 21, 24, 26, 27]. We see the proliferation of *half-integer* defects in active nematics [24], where microtubule-kinesin mixtures [28], bacteria [6, 29] and cell monolayers [30] share similar collective flow profiles around $\pm 1/2$ defects. We expect to find only half-integer defects in our active nematic film from a Ginzburg-Landau energy calculation as this shows that two half-integer defects have less elastic energy than one full-integer defect without any specified anchoring at the boundaries [25]. As such, any full-integer defect should be inherently unstable [31]. Strikingly, the active flows cause topological defects with broken symmetry ($+1/2$ defects) to be self-propelled [6, 10, 13, 32]. Intriguingly, the functional role of these topological defects in the orientation field has been identified in a growing number of biological processes. Notable examples are cytoskeletal topological defects that determine the animal Hydra's growth axis [33, 34], defects in cell orientation governing cell death and extrusion in epithelial tissues [8], defects in bacterial biofilms leading to layer formation [35] and defects as local hotspots of mound formation in neural stem cells [9]. Hence, studying (the control of) defects in active nematics gives us insight into many biophysical processes that exhibit similar symmetries.

Additionally, linear stability analysis predicts that in the absence of frictional damping and hydrodynamic screening, active nematic systems display bend and splay hydrodynamic instabilities [20, 36]. Experiments and numerical simulations have shown that as these instabilities grow, pairs of topological half-integer charged defects nucleate within the bulk of active nematics [10, 22, 37–40]. Recent work has demonstrated that positively charged half-integer topological defects stir the active fluid. Defects mix the active fluid causing chaotic advection [41]. Together with the hydrodynamic instabilities, this causes the formation of disordered collective flows. This state has been observed in experiments and is called *meso-scale* or *active* turbulence [37].

Even though the inertia is negligible at such microscopic scales, active turbulence is characterised by disordered, multiscale flow structures and a distribution of vortices that span many length scales, similar to traditional, scale-invariant, inertial turbulence [42]. However, active turbulence is distinct from inertial turbulence [43, 44] because meso-scale turbulence possesses a characteristic length scale, arising from the energy injection on the local level. Hence, active turbulence is a novel and distinct class of turbulence [39, 45, 46]. Previous studies have shown that by introducing friction [47, 48], rotors periodic in space [49] or geometrical constraints [50, 51], distinct flow profiles emerge as the surrounding environment screens the hydrodynamics. As there is an intrinsic length scale, we can characterise these control mechanisms as a competition between an extrinsic control length scale and the intrinsic active nematic length scale.

One way of introducing screening is by confining active matter into circular or rectangular channel geometries [37, 52, 53]. This confinement can result in orderly flows like oscillations [54–59] or unidirectional motion [50, 60–62]. While extensive research has been dedicated to understanding active nematics and topological defects in confined two-dimensional systems, basic defect properties and flow patterns are only starting to be explored in three-dimensions [63–66]. Recent experiments and simulations [62, 67] have demonstrated that three-dimensional confinement of isotropic active fluids can drive a transition from turbulent flow to a long-range

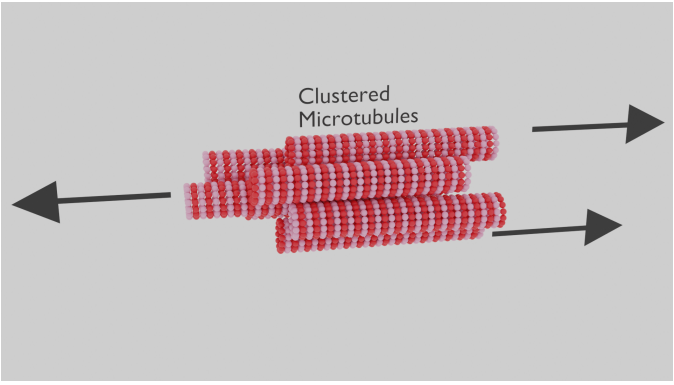

Figure 1.1: Schematic drawing of active microtubule system. Microtubules (drawn) are clustered together. Two microtubules are connected through two-headed kinesin motors (not shown). The motors push the microtubules in opposite directions (black arrows), resulting in collective shear flows.

coherent stream. This transition depends on the channel aspect ratio, showing that higher dimensionality does play a significant role in active fluid behaviour.

Moreover, it is also possible to introduce hydrodynamic screening through frictional damping between active materials and their surroundings. Linear stability analysis shows that frictional damping increases the activity threshold required for the emergence of hydrodynamic instabilities in unconfined systems [68]. Furthermore, numerical and experimental studies have shown that such frictional damping can stabilise active nematics into vortex-lattices [47] and control topological defects' alignment [69], resulting in long-range nematic ordering while retaining their motile nature [70]. Many of these experiments were performed in the system consisting of a suspension of microtubules propelled by two-headed kinesin motors [10] (**Fig. 1.1**). The microtubules assemble at the interface between two layers, *e.g.* an oil and an aqueous layer. The motors induce forces when Adenosine triphosphate (ATP) is added, inducing shear flows to create a two-dimensional active nematic system. Additionally, recent experiments have shown that interfacing microtubule-kinesin suspensions with anisotropic surfaces of smectic liquid crystals can streamline microtubules into a 'laning' state of jets flowing in alternating directions parallel to the smectic layers [12]. This suggests that isotropic or anisotropic environments that dissipate momentum can allow for the creation of highly ordered but dynamical systems.

The possible control of active nematics through the competition of a screening length scale versus the active length scale suggests that natural biological systems can be more complicated than bulk active nematics. Moving cells exist in complex environments with many different confining length scales and where the surroundings govern the hydrodynamic interactions. This complex environment can affect the collective motion [71], resulting in more ordered modes of collective transport. Examples include microorganisms like pathogenic *S. typhimurium*/*B. subtilis* moving in colonic/cervical mucus [72, 73], infiltration of *E. coli* into leaf stomata [74], *B. burgdorferi* escaping from host vasculature [75] or soil-dwelling *M. xanthus* swarming [76]. Thus, to extend research on bulk active nematics [24, 37] to more complex biophysical systems, we need to understand how *active nematics can be controlled* through their surroundings.

We first investigate the transition to three-dimensional active turbulence in Chapter 3. We model an active nematic system between two planar plates with adjustable separation. Point-like defects become disclination lines, but the active nematic still behaves like a quasi-two-dimensional system for small interplate distances. We only observe the contortion of disclination lines into the third dimension after an interplate distance threshold has been reached. We show that this instability is governed by twist deformations around the disclinations, a deformation mode that only becomes accessible in the third dimension [25].

In Chapter 4, we numerically investigate the impact of anisotropy by subjecting an active nematic film to anisotropic frictional damping. By systematically varying the strength of the anisotropy, we obtain the laning state observed in the experiments on microtubule-kinesin motor mixtures [12]. The flow-aligning parameter sets the particles' response to shear flows, and we find that the laning state is only accessible when the particles align to shear flows. Moreover, by changing the flow-aligning parameter to values where anisotropic particles tumble in shear flows, we observe significant changes in the active nematic behaviour. We observe an alignment of topological defects and a state of bound, oppositely charged, defect pairs that navigate through the system leaving behind long-lived distortions within the active

nematic. We find a direct response between the half-integer defect dynamics and the flow-aligning parameter, something that has mostly been overlooked in previous studies.

In Chapter 5, we further investigate the effect of the flow-aligning parameter on bulk active nematics. We show that in active nematics, self-propelled $+1/2$ defects can come together to form full-integer defects. This behaviour emerges in bulk active turbulence [37] and in the absence of any hydrodynamic screening. We show that in addition to activity, the flow-aligning behaviour of active particles is the determining factor in the binding of two $+1/2$ defects into stable full-integer defect structures. These structures' formation is unexpected since the emergence of full-integer topological defects in two dimensions has only been associated with polar symmetry systems [77–80], confined systems subject to strong anchoring conditions [7, 57, 81, 82] or with externally applied stresses [83].

To further clarify how defects order in wet active nematics, we perform large scale continuum simulations in Chapter 6 to measure both the positional and the orientational order of topological defects with varying friction between the active nematic layer and the surrounding substrate. We show that $+1/2$ defects prefer to position themselves side by side and align anti-parallel [13, 84], while the $-1/2$ defects prefer to impose a three-fold symmetry on their surroundings. Increasing friction decreases the hydrodynamic screening length, which determines the competition between viscosity and friction. The friction increases the defect-defect interactions' effectiveness, and the defects start to form dynamically evolving orientationally and positionally ordered structures even in the regime where defects are still motile. The range of the ordering increases with increasing friction until active turbulence is destroyed.

While these phenomena suggest ways for controlling active nematics, they require uniform direct contact with an active fluid, and they do not allow for local control of the active nematic film. In Chapter 7, we propose a new micropatterned method for controlling active nematics without contiguous contact with the active layer. By patterning the solid substrate below the active nematic with geometrical structures

of differing height, experiments can tune the depth of the oil layer beneath the active film. This locally adjusts the dissipation rate within the adjacent active film, which results in a local variation of frictional damping in the active layer. We achieve effective hydrodynamic boundaries within an active nematic film with these varying friction regions that control topological defect populations, collective flow, and active material concentration.

This thesis's content demonstrates how the underlying geometry, activity, particle response to shear flows, and effective friction all have pronounced effects on active dynamics and the topological defects. It provides us with insights into how a complex biological system could control the collective shear stress so that it can establish collective flow profiles that are dynamical but ordered.

Of course I've gone mad with power! Have you ever tried going mad without power? It's boring and no one listens to you!

Matt Groening

2

Passive and active nematic liquid crystals

This chapter gives the theoretical framework on which the rest of this thesis is built. As discussed in the introduction, we investigate active fluids which consist of constituents that are self-propelled or exert mechanical forces [18]. We focus on systems of microscopic particles that move together on scales significantly larger than the size of an individual. This thesis concentrates on systems where the collective dynamics manifest nematic flow symmetries, called active nematics. These active nematics display chaotic flows in bulk due to collective hydrodynamic stress that the active swimmers generate. The goal is to investigate how we can control the collective motion through their surroundings and tame the active turbulence.

To describe these vastly different biological systems' collective motion, we need to understand the flow symmetries. This knowledge allows us to model different biophysical systems using the framework of continuous equations that we present here. We start this chapter by introducing nematic liquid crystals and the nematic orientation field, which we describe with a tensor order parameter. We use the symmetry of this tensor order parameter to construct a Landau-de Gennes free energy [25]. We introduce long-range continuous deformation modes which we penalise with additional terms in the free energy. Lastly, we describe discontinuities in the orientation field. This framework allows us to describe the rich interplay

between the orientational structure, topology and flow of active nematic systems, which we will be modelling using continuum dynamics.

Then we introduce the properties of active materials and show how the far-flow field of an individual swimmer, and therefore the active stress has nematic symmetry. We explain how the active stress results in hydrodynamic instabilities. This affects the orientation field deformations and defect dynamics and yields chaotic collective flows in bulk: active turbulence.

2.1 Liquid crystals

Liquid crystals are phases of matter in between the crystalline and liquid phase. Crystals have long-range positional and orientational order (**Fig. 2.1**a). In the liquid state, the positions of the particles are disordered with only short-range correlations (**Fig. 2.1**b). Liquid crystal phases sit between these two regimes and typically consist of long, thin, rod-like particles (**Fig. 2.1**c). These liquid crystals possess solid-like properties, *e.g.* elasticity, but also have liquid-like properties, *e.g.* fluidity and the inability to support shear [25]. There have been ample experimental observations of the liquid crystal state [25, 85, 86] with the first report of a liquid crystal in 1888 by Reinitzer [87]. Historically, Friedel proposed the classification of liquid crystals based on their structural properties [88], with liquid crystals typically being in a nematic state, in which rod-like particles locally align with each other. In this regime, liquid crystals have long-range orientational order and are characterised by an orientation field, which is one of the coarse-grained variables we use throughout this thesis to describe the anisotropic structure.

2.1.1 Nematic order parameter

The orientation of an anisotropic particle can be labelled by unit vector $\vec{b}$ along its symmetry axis. In a coarse-grained description, the average orientation of these particles is described by the director field $\boldsymbol{n}$ (**Fig. 2.1**c). This director is, by definition, the orientation along which particles preferentially align locally. We point out that this director is not a standard vector field as $\boldsymbol{n}$ and $-\boldsymbol{n}$ are

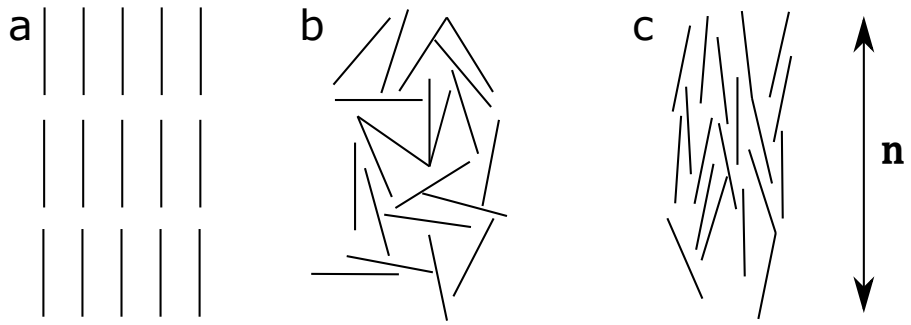

Figure 2.1: Schematic of various possible phases of matter. (a) Crystalline solid with a fixed distribution of particle positions and orientations. (b) Isotropic liquid with a random distribution of particle positions and orientations. (c) Nematic liquid crystal with a random distribution of particle positions, but with a preference of orientation along a common axis called the director $\boldsymbol{n}$. This director $\boldsymbol{n}$ represents the local average orientation of the liquid crystal.

indistinguishable under nematic symmetry. The director field in a nematic is apolar and has head-tail symmetry. This head-tail symmetry means that the director angle θ is identical under rotation by $\theta = \theta + \pi$, unlike a normal vector where the vector is unchanged if $\theta_p = \theta_p + 2\pi$ [25]. To emphasise this difference, we use a different vector notation for the director field than for other vectors. Following the usual convention in the literature [25], the director will be treated as a standard vector field, and head-tail symmetry will be imposed by hand when applicable. Similarly, we fix the director's magnitude to unity as it describes a direction in orientation space [25]. Hence, it cannot be used as an order parameter to describe the local particles' ordering and distinguish isotropic from nematic liquids.

To define the magnitude of particle alignment, we take an average of the multipole expansion of the local particle orientation $\vec{b}$. If $\boldsymbol{n}$ points along the z-axis, $\vec{b}$ can be defined by spherical coordinates in relation to $\boldsymbol{n}$ as $(\sin\theta_b \cos\phi_b, \sin\theta_b \sin\phi_b, \cos\theta_b)$. A probability distribution $f(\theta_b, \phi_b)d\Omega$ describes the average local rod alignment. We assume the system to have cylindrical symmetry around $\boldsymbol{n}$. Thus $f(\theta_b, \phi_b)d\Omega$ is independent of ϕ_b. Systems without cylindrical symmetry around $\boldsymbol{n}$ are called biaxial [25] and are outside the scope of this thesis. Additionally, we recall that $\boldsymbol{n} = -\boldsymbol{n}$ with $f(\theta_b) = f(\pi - \theta_b)$ and use Legendre polynomials for the multipole expansion

in θ_b. The first non-zero term in the multipole expansion is the quadrupole term

$$q = \frac{1}{N}\sum_{\alpha}\left(\frac{3}{2}\cos^2\theta_b^{(\alpha)} - \frac{1}{2}\right) = \int f(\theta_b)\left(\frac{3}{2}\cos^2\theta_b - \frac{1}{2}\right)d\Omega, \tag{2.1}$$

with q a scalar value. The sum over a local number of particles N with individual directions $\vec{b}^{(\alpha)}$ in the second term is replaced with the angle distribution function $f(\theta_b)$ to write the third term in **Eq. 2.1**. In the nematic case, $f(\theta_b)$ is sharply peaked around $\theta_b = 0$. Hence, we find $q = 1$ from **Eq. 2.1**, if there is strong nematic ordering. On the other hand, when the particle angles are randomly distributed, we get an isotropic liquid with $q = 0$. This dependence shows that the order parameter q is a scalar measurement of the magnitude of alignment.

However, q does not carry any information about the direction of particles, which is characterised by the director $\boldsymbol{n}$. To describe both the isotropic-nematic transition and the local orientation, we define a single tensor order parameter $\boldsymbol{Q}$. It is derived in the same way as the scalar order parameter q, via a quadrupole expansion [25, 46],

$$\boldsymbol{Q} = \frac{1}{N}\sum_{\alpha}\left(\vec{b}^{(\alpha)}\vec{b}^{(\alpha)} - \frac{1}{3}\boldsymbol{I}\right), \tag{2.2}$$

with $\boldsymbol{I}$ the unit tensor. The tensor $\boldsymbol{Q}$ is symmetric and traceless. Hence, the three-dimensional tensor $\boldsymbol{Q}$ has rank two and only contains five independent components defined in terms of the individual particle alignments $\vec{b}^{(\alpha)}$.

Often it is desirable to rewrite $\boldsymbol{Q}$ in terms of the nematic director $\boldsymbol{n}$. This rewriting can be done by choosing the coordinate system in which $\boldsymbol{Q}$ is diagonal $\boldsymbol{Q} = \mathrm{diag}(\lambda_1, \lambda_2, -\lambda_1 - \lambda_2)$ with $\lambda_{1,2}$ being the tensor's eigenvalues. The eigenvector with the largest eigenvalue is now the director $\boldsymbol{n}$, and the corresponding eigenvalue is connected to the scalar order parameter q [25], and we can write the tensor order parameters as

$$\boldsymbol{Q} = \frac{3q}{2}\left(\boldsymbol{nn} - \frac{1}{3}\boldsymbol{I}\right). \tag{2.3}$$

This tensor order parameter allows us to describe the evolution of the coarse-grained local director $\boldsymbol{n}$ and scalar nematic order q. Another major advantage of using the tensor order parameter $\boldsymbol{Q}$ is that we do not need to manually input the

director's head-tail symmetry. The tensor product of the director $\boldsymbol{nn}$ is equivalent to the tensor product composed of the vector field term $\vec{n}\vec{n}$. Hence, mathematically we can treat $\boldsymbol{n}$ as a polar vector field without any manual corrections, as long as we work with the tensor order parameter $\boldsymbol{Q}$.

2.1.2 Emergence of nematic ordering

In the previous subsection 2.1.1, we defined nematic symmetry and a measurement of the orientational order. We now summarise the theories of the emergence of nematic ordering. Passive nematic liquid crystals can in be classified as either thermotropic [85] or lyotropic [86], where the transition to the nematic state is set by temperature or anisotropic particle density, respectively. One of the earliest attempts to model the emergence of liquid crystals is the Onsager theory. This theory describes the emergence of a lyotropic nematic liquid crystal as a function of particle density [89].

The Onsager theory is a hard-rod model where rods align to minimise other rods' excluded volume. When rod-like particles point in the same direction, there is very little excluded volume due to their anisotropy. However, if rods lie at some angle to each other, they impose a large excluded volume around themselves felt by the other particles. As a result, reorientation of particles into a nematic state can decrease the positional entropy at high particle densities. This makes the nematic state a free energy minimum for high densities in lyotropic liquid crystals. However, the realignment is often not purely dictated by steric interactions but includes contributions from other interactions, *e.g.* attractive intermolecular interactions. In that case, the transition from the isotropic to the nematic state depends on temperature (thermotropic liquid crystal) as there is a competition between energy and entropy [90].

Regardless of the actual nematic system, isotropic and nematic states are minima of a free energy $\mathcal{F}$ in thermodynamic equilibrium. A Ginzburg-Landau free energy can be constructed based on the symmetry of $\boldsymbol{Q}$, where the free energy is the volume integral of a local function of $\boldsymbol{Q}$ and its derivatives. This free energy is called a Landau-de Gennes free energy in nematic liquid crystals [25]. The isotropic-nematic

transition is only weakly first-order [91], and this expansion works surprisingly well in the nematic phase, as shown by experiments [92]. Strictly speaking, the minimum free energy description corresponds to a system in thermodynamic equilibrium, but it is also useful to describe the relaxation dynamics of out-of-equilibrium systems [24]. Hence, we introduce the free energy to define the ground state (either isotropic or nematic) in the absence of collective shear flows.

Two parts of the Landau-de Gennes expansion can be distinguished: terms containing expansions of $\boldsymbol{Q}$, which make up the bulk free energy density $\mathcal{F}_b$ and expansions in derivatives of $\boldsymbol{Q}$, which make up the gradient free energy density $\mathcal{F}_g$. The only rotationally invariant functions of a traceless three-dimensional tensor are $tr(\boldsymbol{Q}^2)$ and $tr(\boldsymbol{Q}^3)$ [25]. Hence, the bulk free energy can be written as

$$\mathcal{F}_b = \frac{\mathcal{A}}{2} tr(\boldsymbol{Q}^2) + \frac{\mathcal{B}}{3} tr(\boldsymbol{Q}^3) + \frac{\mathcal{C}}{4} (tr(\boldsymbol{Q}^2))^2, \tag{2.4}$$

with $\mathcal{A}, \mathcal{B}$ and $\mathcal{C}$ called Landau-de Gennes coefficients. The expansion is taken to the fourth-order to ensure thermodynamic stability, and we have omitted constant terms as they do not affect the minima. To achieve stability against unbounded growth of the scalar order parameter q, we take $\mathcal{C}$ as a positive value. By altering $\mathcal{A}, \mathcal{B}$ and $\mathcal{C}$, we can set the isotropic or nematic state as the global ground state. We note that the tensor dimension choice affects the free energy and the transition from an isotropic to nematic liquid. The $tr(\boldsymbol{Q}^3)$ term is only allowed when considering a tensor of dimension three. In a tensor with dimension two, this term disappears due to symmetry [25] and the transition from isotropic to nematic is continuous without this term [93].

In this thesis, we use the tensor order parameter $\boldsymbol{Q}$ with dimension three to investigate both two and three-dimensional systems. This allows us to use the same set of equations in every chapter. This choice of tensor dimension allows the director to develop out-of-plane components when modelling a two-dimensional nematic film. However, the system will be chosen such that the director (and velocity) remain in the xy-plane when appropriate [39, 53]. We guarantee this by setting the number of discretised grid points along the z-axis to one and applying periodic

boundary conditions. This results in no z-components in the evolution equations and nothing will drive the director to go into the third dimension. Comparison of this approach to strictly two-dimensional simulations has confirmed the qualitative agreement of the two methods [46].

The scalar order of the ground state is found by rewriting **Eq. 2.4** for a homogenous degree of nematic order q as [25]

$$\mathcal{F}_b = \frac{3\mathcal{A}}{4}q^2 + \frac{\mathcal{B}}{4}q^3 + \frac{9\mathcal{C}}{16}q^4. \tag{2.5}$$

This free energy is minimised to find the nematic ordering of the ground state

$$q_0 = -\frac{\mathcal{B}}{6\mathcal{C}} \pm \sqrt{(\frac{\mathcal{B}}{3\mathcal{C}})^2 - \frac{8\mathcal{A}}{16\mathcal{C}}}, \tag{2.6}$$

and trivially the isotropic value $q_0 = 0$ [25].

A common method to define the transition from isotropic to nematic is to make $\mathcal{A}, \mathcal{B}$ and $\mathcal{C}$ dependent on one parameter. In this thesis, we use the parameter ϵ, which is related to the orientation-dependent interactions and the concentration of the nematogens: [94]

$$\mathcal{F}_b = \mathcal{A}_0 \left(\frac{1}{2}\left(1 - \frac{\epsilon}{3}\right) tr(\boldsymbol{Q}^2) - \frac{\epsilon}{3}(tr\boldsymbol{Q}^3) + \frac{\epsilon}{3}(tr(\boldsymbol{Q}^2))^2 \right). \tag{2.7}$$

Here $\mathcal{A}_0$ is a positive constant with units of energy per volume. The ϵ parameter sets the transition from the isotropic to the nematic state (which happens at $\epsilon = 2.7$) and is often called an effective temperature to connect it to thermotropic models.

The gradient free energy density $\mathcal{F}_g$ is an expansion in derivatives of $\boldsymbol{Q}$. The lowest order rotationally invariant derivatives are

$$\mathcal{F}_g = \frac{L_1}{2}\partial_k Q_{ij}\partial_k Q_{ij} + \frac{L_2}{2}\partial_k Q_{kj}\partial_i Q_{ij}, \tag{2.8}$$

with L_i being tensor elastic constants. There is a third rotationally invariant quantity up to second order in derivatives, $\partial_i Q_{jk}\partial_j Q_{ik}$. However, this term only gives a surface contribution when integrated. It is disregarded in this thesis as we assume that surface effects in the gradient free energy are small compared to bulk effects, as is commonly done for nematics [95].

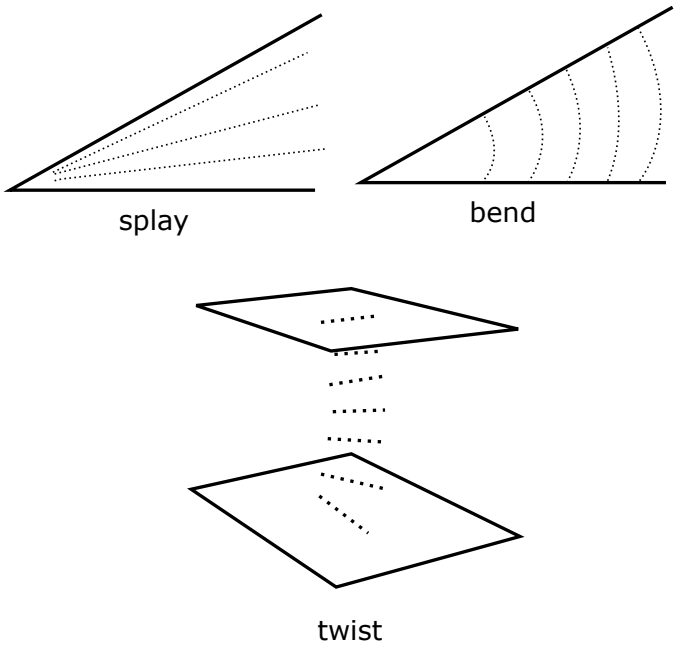

Figure 2.2: Schematic representation of the three modes of bulk director deformations: bend, splay and twist. The dotted lines represent the director between surfaces (solid lines).

The tensor elastic deformations can be mapped to the more well-known bend, twist and splay bulk deformations of the director field $\boldsymbol{n}$,

$$\mathcal{F}_g = \frac{1}{2}\left[K_{\text{Splay}}(\vec{\nabla}\cdot\boldsymbol{n})^2 + K_{\text{Bend}}(\boldsymbol{n}\times(\vec{\nabla}\times\boldsymbol{n}))^2 + K_{\text{Twist}}(\boldsymbol{n}\cdot(\vec{\nabla}\times\boldsymbol{n}))^2\right], \quad (2.9)$$

with corresponding deformations illustrated in **Fig. 2.2** [25]. The Frank elastic constants K_i are found through the relations [96]

$$\begin{aligned}\frac{2K_{\text{Bend}}}{9q_0^2} &= L_1 + \frac{L_2}{2},\\ \frac{2K_{\text{Twist}}}{9q_0^2} &= L_1,\\ \frac{2K_{\text{Splay}}}{9q_0^2} &= L_1 + \frac{L_2}{2}.\end{aligned} \quad (2.10)$$

We take K_i to be positive as deformations must be unfavourable in the nematic system [25]. Following common practice [24], the one-constant approximation,

$$\mathcal{F}_g = \frac{1}{2}K\left[\left|\vec{\nabla}\cdot\boldsymbol{n}\right|^2 + \left|\vec{\nabla}\times\boldsymbol{n}\right|^2\right], \quad (2.11)$$

is used in most of this thesis, where all Frank elastic constants are set to $K_i = K$, corresponding to L_1 being the only non-zero tensor elastic constant in the gradient free energy density (**Eq. 2.8**).

2.1.3 Biphasic liquid crystals

The free energy description presented in subsection 2.1.2 describes a liquid crystal where the nematic state is the ground state throughout the entire system. This description allows us to study the control of the collective orientation field in active nematics. This is a necessary step to understanding the collective flow fields observed in many biophysical systems. In addition to orientation and flow fields, we may want to study variations in the concentration of active materials. Evolving the active particle concentration is interesting as there are many biophysical problems driven by active migration, *e.g.* microorganisms like pathogenic *S. typhimurium*/*B. subtilis* penetrating colonic/cervical mucus [72, 73], infiltration of *E. coli* into leaf stomata [74], or tumour cells migration [97].

To model the varying concentration of active particles, we introduce a phase-field parameter ϕ. The free energy is expanded to include the additional order parameter. The free energy contributions are a homogeneous term that describes the possible phase separation into a region of high ($\phi = 1$) and low ($\phi = 0$) concentration of active material. In addition, the free energy contains a contribution from gradients in the ϕ field.

For the homogeneous term, any possible shape of a double-well potential is allowed [98]. In this thesis, the choice is

$$\mathcal{F}_{\mathrm{b},\phi} = \frac{\mathcal{A}_\phi}{2}\phi^2(1-\phi)^2, \tag{2.12}$$

where $\mathcal{F}_\phi$ is a positive constant. The gradient term,

$$\mathcal{F}_{\mathrm{g},\phi} = \frac{K_\phi}{2}(\vec{\nabla}\phi)^2, \tag{2.13}$$

is included (with K_ϕ a positive constant) to ensure a smooth concentration profile across an interface. This combination (**Eq. 2.12** and **Eq. 2.13**) results in a non-zero interfacial tension. This description of the binary fluid also results in a finite interface width between regions of different concentration [98]. We do not include any additional couplings between the nematic tensor parameter $\boldsymbol{Q}$ and concentration ϕ. Hence, the equilibrium properties of the two binary fluids are identical.

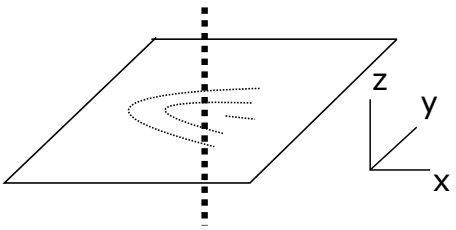

Figure 2.3: Schematic representation of the planar projection of a disclination line to a normal plane. In the two-dimensional plane, we find a point-like topological defect where we cannot define the local orientation. The straight, dashed line represents the disclination line, and the dotted lines indicate the local director in a plane normal to the disclination line.

2.1.4 Discontinuities in the orientation field

In subsection 2.1.2, we introduced continuous smooth distortions in the orientation field as deformations in the director $\boldsymbol{n}$. However, there can be points in the orientation field, where the director is not a smooth function. These discontinuities can be located at points (point defects), on a line (disclination lines), or over an area (walls) in three-dimensional liquid crystals. These singularities can have long-range interactions [99] and create long-range orientational structure, *e.g.* Schlieren structures [100], so we need to be able to distinguish the discontinuities.

In nematic liquid crystals, discontinuous walls are inherently unstable [25], as localised discontinuous wall kinks are energetically unfavourable compared to gradual smooth variations in orientation [25]. Because walls are not topologically protected, the deformations smear out to smooth continuous distortions with specific widths, similar to ferromagnetic domain walls. Thus in nematics, we only detect point defects and disclination lines.

This thesis will mostly be on two-dimensional nematic films, where topological defects can be seen as planar projects of disclination lines (**Fig. 2.3**). Hence, in two-dimensions discontinuities will always appear as points.

If the director field remains in the two-dimensional plane, we cannot define the local orientation at the point singularities. These objects are called topological defects. We characterise these defects with a strength or charge. The charge measures how many times the director winds along a contour taken around the

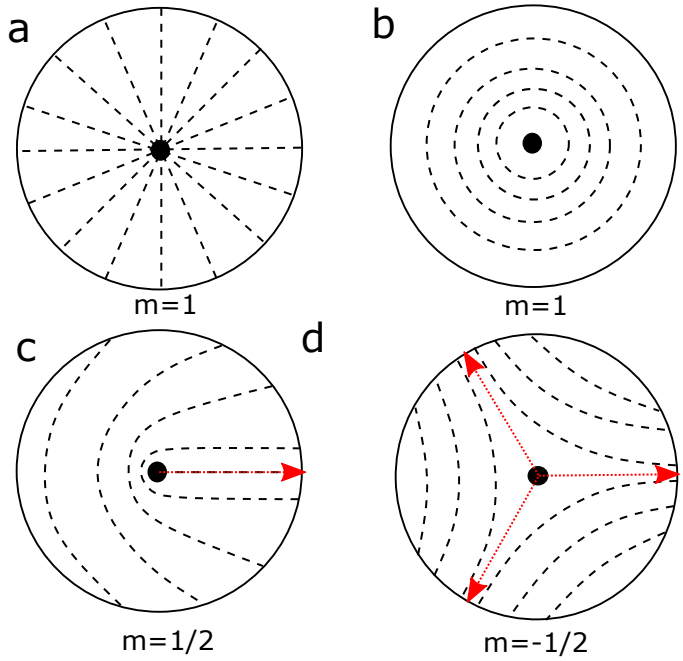

Figure 2.4: Schematic illustration of topological defects in nematic liquid crystals. The director field (dashed line) around topological defects (black points) as defined in **Eq. 2.16** for (a) $m = 1$ splay-type defect with $\theta_0 = 0$, (b) $m = 1$ bend-type defect with $\theta_0 = \pi/2$, (c) $m = 1/2$ with $\theta_0 = 0$ and (d) $m = -1/2$ with $\theta_0 = 0$. The half-integer charged defects have symmetry axes and thus a defect orientation $\vec{p}$ (red arrows).

topological defect. By expressing the director as

$$\mathbf{n} = [\cos\theta, \sin\theta] \tag{2.14}$$

with the director angle θ, we can define the charge m as

$$m = \frac{1}{2\pi} \oint d\theta, \tag{2.15}$$

where the line integral is taken around the defect core. The possible director configurations around isolated topological defects are solutions that minimise **Eq. 2.11**. The general solution is

$$\mathbf{n} = [\cos(m(\varphi + \theta_0)), \sin(m(\varphi + \theta_0))], \tag{2.16}$$

where φ is a polar angle to the x-axis, and θ_0 is an off-angle representing the charge m defect's possible configurations. Different topological defects are shown in **Fig. 2.4**.

Because the nematic director is apolar, θ is invariant under rotation by $\theta \to \theta + \pi$. Hence, m can take values in increments of $\pm 1/2$, instead of the ± 1 increments

found in polar liquids. Once topological defects have emerged, they cannot be resolved through a smooth reorientation of the director field $\boldsymbol{n}$. The only way defects can be added or removed is by creation or annihilation with other defects, where the total charge m is conserved [25].

Additionally, we can define the orientation of half-integer topological defects with a vector coordinate $\vec{p}$ as half-integer defects have symmetry axes (**Fig. 2.4**c,d). The vector coordinate $\vec{p}$ is defined as [11]

$$\vec{p} = [\cos\psi, \sin\psi]\,, \tag{2.17}$$

with

$$\psi = \frac{m}{1-m}\left[\frac{\langle \mathrm{sgn}(m)\partial_x Q_{xy} - \partial_y Q_{yy}\rangle}{\langle \partial_x Q_{xx} + \mathrm{sgn}(m)\partial_y Q_{xy}\rangle}\right], \tag{2.18}$$

where $\langle\rangle$ denotes an average along the shortest available loop enclosing the topological defect, and $\mathrm{sgn}(m)$ means the sign of charge m. We point out that the $-1/2$ defect is only uniquely defined in $\psi \in \left[\frac{-\pi}{3}, \frac{\pi}{3}\right]$ due to its three-fold symmetry. A $-1/2$ defect has three axes that define it and a $+1/2$ defect only has a single axis.

We reiterate that the introduced angles φ, ψ, θ_0 and θ are different angles. φ is a general polar coordinate angle with respect to the x-axis. ψ is the angle of the vector orientation $\vec{p}$ of a half-integer topological defect (**Eq. 2.17**). θ_0 is the off-angle which describes the configuration for any defect (**Eq. 2.16**). For a half-integer defect, θ_0 and ψ can be mapped to each other. Lastly, θ is the angle of the director field $\boldsymbol{n}$ (**Eq. 2.14**).

Using the director description around an individual defect (**Eq. 2.14**), we can approximate its elastic energy cost by integrating **Eq. 2.11** around a defect from a near-zero distance d to a boundary distance R,

$$E_{\mathrm{Self}} = \pi K m^2 \ln(R/d). \tag{2.19}$$

We remark that this energy is per unit length, as we are calculating the energy of a three-dimensional object over a two-dimensional surface. We introduce a long-distance cut-off R in **Eq. 2.19**, typically taken as the distance to boundaries

or other topological defects [25]. We also use a cut-off core distance d, which is the defect core size where the orientation is ill-defined and corresponds to an isotropic state at the defect core. Thie contribution of the inner isotropic core region ($< d$) is not included in **Eq. 2.19**, but can be estimated as a slight modification of the logarithm [25]. We notice that without this core region d, the energy cost of a defect goes to infinity. The issue of avoiding infinite energy in the orientation description is resolved by letting the scalar order parameter q go to zero at the defect's core. This melting is automatically captured with the tensor order parameter $\boldsymbol{Q}$ framework [25].

We can also estimate the elastic interaction between two defects with charges m_1 and m_2 located at $\vec{r}_1$ and $\vec{r}_2$ by integrating **Eq. 2.11**. We find an estimate for the elastic potential between defects as [25]

$$E_{\text{Pair}} = 2\pi m_1 m_2 K \left[\log \frac{|\vec{r}_1 - \vec{r}_2|}{d}\right]. \tag{2.20}$$

Similar to **Eq. 2.19**, we omitted the defect core cost in **Eq. 2.20**. We find a repulsive (attractive) force for same (oppositely) charged defects by taking the derivative of this potential ($-\frac{dE_{\text{Pair}}}{d\vec{r}}$) [25]. This shows that oppositely charged defects are attractive and tend to annihilate to minimise the elastic energy cost. In passive nematic systems, this causes the defect population to gradually reduce to zero.

When describing disclination lines in three dimensions, we can still define a contour around the disclination line and determine the line segment's charge using **Eq. 2.15**. Similar to their planar point projections, we find that disclination lines have charges of $\pm 1/2$ incremental values. Hence, there are half-integer strength disclination lines. The director configurations around these disclination lines will be a combination of the planar projections of $\pm 1/2$ defects (**Fig. 2.4**) and the director twisting parallel to the disclination line. Lastly, point defects can be found in three-dimensional nematics and have charges in ± 1 incremental values [25] and are energetically unfavourable compared to disclination lines with charges $\pm 1/2$. In Appendix B, we explain how defects are detected from the orientation tensor $\boldsymbol{Q}$.

2.2 Continuum model

To study active nematics, we choose to solve the continuum equations that describe the evolution of the continuous fields, *i.e.* fluid density ρ, collective fluid velocity $\vec{u}$, orientation tensor $\boldsymbol{Q}$ and concentration ϕ. The framework described in this section is called nematohydrodynamics [101].

2.2.1 The convection-diffusion equation

We first introduce the evolution of the orientation tensor $\boldsymbol{Q}$. The continuum equation we use to describe the nematic tensor dynamics is the Beris-Edwards equation [101]

$$\left(\partial_t + \vec{u}\cdot\vec{\nabla}\right)\boldsymbol{Q} - \boldsymbol{S} = \Gamma\boldsymbol{H}, \tag{2.21}$$

where Γ is a rotational diffusivity and $\boldsymbol{S}$ is the co-rotational advection term. $\boldsymbol{S}$ accounts for tensor $\boldsymbol{Q}$ reorientations due to flow gradients $\vec{\nabla}\vec{u}$. The strain tensor $\boldsymbol{E} = (\vec{\nabla}\vec{u}^T + \vec{\nabla}\vec{u})/2$ and vorticity tensor $\boldsymbol{\Omega} = (\vec{\nabla}\vec{u}^T - \vec{\nabla}\vec{u})/2$ characterise these flow gradients. The co-rotational advection term has the form

$$\boldsymbol{S} = (\lambda\boldsymbol{E} + \boldsymbol{\Omega})\cdot\left(\boldsymbol{Q} + \frac{1}{3}\boldsymbol{I}\right) + \left(\boldsymbol{Q} + \frac{1}{3}\boldsymbol{I}\right)\cdot(\lambda\boldsymbol{E} - \boldsymbol{\Omega}) - 2\lambda\left(\boldsymbol{Q} + \frac{1}{3}\boldsymbol{I}\right)\mathrm{tr}\left(\boldsymbol{Q}\cdot\vec{\nabla}\vec{u}\right) \tag{2.22}$$

in which we introduce a flow-aligning parameter λ [102].

The flow-aligning parameter λ describes the particles' alignment with respect to the velocity gradients' extensional $\boldsymbol{E}$ and rotational $\boldsymbol{\Omega}$ components. The flow-aligning parameter depends on the scalar nematic order parameter q. If the condition

$$|\lambda| \,/\, \left|\frac{9q}{3q+4}\right| > 1 \tag{2.23}$$

is satisfied, the director $\boldsymbol{n}$ aligns at a stable Leslie angle θ_L to the principal axis of flow deformation [103, 104]. This Leslie angle is

$$\theta_L = \frac{1}{2}\sin^{-1}(1/\nu), \tag{2.24}$$

with a normalised flow-aligning parameter $\nu = \lambda/\frac{9q}{3q+4}$ and the principal axis of flow deformation is defined as

$$\theta_P = \frac{1}{2}\tan^{-1}\left(\frac{2E_{xy}}{E_{xx} - E_{yy}}\right), \tag{2.25}$$

based on the strain tensor $\boldsymbol{E}$ in two-dimensions [52]. If **Eq. 2.23** is not satisfied, the nematic is said to be in the flow-tumbling regime, and the director continuously tumbles in shear flows.

In subsection 2.1.2, we introduced free energy terms (**Eq. 2.4** and **Eq. 2.8**) to define the ground state of the system. The orientation relaxation is controlled through the total free energy $\mathcal{F}$ (sum of **Eq. 2.4** and **Eq. 2.8**) and the molecular field $\boldsymbol{H}$, with

$$\boldsymbol{H} = -(\frac{\delta \mathcal{F}}{\delta \boldsymbol{Q}} - \frac{1}{3}\boldsymbol{I}\ \mathrm{Tr}\frac{\delta \mathcal{F}}{\delta \boldsymbol{Q}}). \tag{2.26}$$

The molecular field $\boldsymbol{H}$ ensures that the $\boldsymbol{Q}$ evolves towards the minimum of the free energy $\mathcal{F}$ in the absence of collective flows. This allows us to define the nematic relaxation time by modifying the rotational diffusivity Γ [101].

2.2.2 The Navier-Stokes equations

Simultaneously to the evolution of the orientation tensor $\boldsymbol{Q}$, the density ρ and collective velocity $\vec{u}$ obey the Navier-Stokes equations [102]

$$\frac{\partial \rho}{\partial t} + \vec{\nabla} \cdot (\rho \vec{u}) = 0, \tag{2.27}$$

$$\rho \left(\partial_t + \vec{u} \cdot \vec{\nabla}\right) \vec{u} = \vec{\nabla} \cdot \boldsymbol{\Pi} - \boldsymbol{f} \cdot \vec{u}. \tag{2.28}$$

The Navier-Stokes equations are the conservation of mass and momentum equations, respectively. This set of equations is complicated due to additional momentum dissipation terms resulting from modelling a complex fluid. These terms appear on the right side of **Eq. 2.28**.

The $\boldsymbol{\Pi}$ is a generalised stress tensor. The stress includes the isotropic viscous stress $\boldsymbol{\Pi}_{\mathrm{Visc}} = 2\eta \boldsymbol{E}$ and an elastic stress due to the reorientations of the nematic,

$$\begin{aligned}\boldsymbol{\Pi}_{\mathrm{Elastic}} = &-P\boldsymbol{I} + 2\lambda \left(\boldsymbol{Q} + \frac{1}{3}\boldsymbol{I}\right)(\boldsymbol{Q} : \boldsymbol{H}) - \lambda \boldsymbol{H} \cdot \left(\boldsymbol{Q} + \frac{1}{3}\boldsymbol{I}\right) - \lambda \left(\boldsymbol{Q} + \frac{1}{3}\boldsymbol{I}\right) \cdot \boldsymbol{H} \\ &- \vec{\nabla}\boldsymbol{Q} : \frac{\delta \mathcal{F}}{\delta \vec{\nabla}\boldsymbol{Q}} + \boldsymbol{Q} \cdot \boldsymbol{H} - \boldsymbol{H} \cdot \boldsymbol{Q},\end{aligned} \tag{2.29}$$

where P denotes pressure and the operator : in the term $-\vec{\nabla}\boldsymbol{Q} : \frac{\delta \mathcal{F}}{\delta \vec{\nabla}\boldsymbol{Q}}$ denotes the tensor operation $\nabla_i Q_{kl} \frac{\delta \mathcal{F}}{\delta \nabla_j Q_{kl}}$ [102]. The stress tensor $\boldsymbol{\Pi}$ can also contain a

stress due to concentration differences $\mathbf{\Pi}_\phi$ and an active stress $\mathbf{\Pi}_{\text{Act}}$, which will be introduced in subsection 2.2.3 and 2.3.2, respectively.

Additionally, the $\boldsymbol{f}$ is a constant diagonal tensor that describes the friction between the nematic and its surroundings. The friction corresponds to situations where the underlying substrate or the surrounding medium extracts momentum from the nematic layer [68]. In our model, the friction depends on the velocity direction.

2.2.3 The Cahn-Hillard equation

Lastly, we can expand our set of continuum equations to allow for varying nematic particle concentrations. We evolve the concentration field ϕ according to a Cahn-Hillard convection-diffusion model [98]. We assume that the particle concentration ϕ does not impact fluid density ρ. In that case, the continuum equation is

$$\partial_t \phi + \vec{\nabla} \cdot (\vec{u}\phi) \quad = \quad \Gamma_\phi \vec{\nabla}^2 \mu, \tag{2.30}$$

where $\mu = \frac{\delta \mathcal{F}}{\delta \phi} - \vec{\nabla} \cdot \left(\frac{\delta \mathcal{F}}{\delta \vec{\nabla} \phi} \right)$ is the chemical potential and Γ_ϕ is a mobility coefficient. The free energy $\mathcal{F}$ now includes the additional free energy terms **Eq. 2.12** and **Eq. 2.13** to allow for possible phase separation into different concentrations ϕ. If the chemical potential μ is non-zero, we have concentration imbalances. The right side of **Eq. 2.30** describes concentration currents to oppose these imbalances. Lastly, a difference in concentration induces an additional stress in the momentum dissipation terms of **Eq. 2.28**. This stess $\mathbf{\Pi}_\phi$ is [5]

$$\mathbf{\Pi}_\phi = (\mathcal{F} - \mu\phi)\boldsymbol{I} - \vec{\nabla}\phi \left(\frac{\delta \mathcal{F}}{\delta \vec{\nabla} \phi} \right). \tag{2.31}$$

2.2.4 Isotropic viscosity

In the equations **Eq. 2.21**, **Eq. 2.27** and **Eq. 2.28**, we made the explicit assumption that we only have the isotropic viscosity and no anisotropic viscosities. Originally, the hydrodynamic equations of liquid crystals in terms of the director $\boldsymbol{n}$ and the velocity field $\vec{u}$ were derived by Erickson [105, 106] and later developed by Leslie [107, 108]. Their equations identified six Leslie-Erickson parameters, which establish viscous dissipation in the anisotropic liquid crystal and an orientation realignment

through shear flows. Parodi expanded upon this by identifying that there were only five independent Leslie-Erickson parameters [109]. Afterwards, Edwards, Beris and Grmela [101, 110] developed this framework further to describe the relationship between the flow field $\vec{u}$ and the tensor order parameter $\boldsymbol{Q}$, which allows for varying nematic order q. In the Edwards-Beris-Grmela framework, there are eight viscous parameters where only six are independent [101].

The choice of only including an isotropic viscosity is a common simplification in the study of nematics [8, 11, 45, 46, 102, 111]. This simplification reduces the number of independent dynamic parameters to three: the isotropic viscosity η, the flow-aligning parameter λ and the rotational diffusivity Γ [102].

2.2.5 Implementation of the model

To solve the set of coupled equations **Eq. 2.21**, **Eq. 2.30**, **Eq. 2.27** and **Eq. 2.28**, we use a combination of a lattice Boltzmann (LB) and a finite difference method [102]. The Navier-Stokes equations **Eq. 2.27** and **Eq. 2.28** are solved with a lattice Boltzmann scheme. We employ an BGK collision operator [112] with an extension to include additional stresses and forces (friction) [102]. As we are using an BGK LB scheme, we solve the full Navier-Stokes equations in the weakly compressible limit with only small fluctuations around density $\rho = 1$ [112]. Additionally, the time and spatial grid sizes are set to one as is traditional in LB simulations. This allows us to normalise all other parameters with respect to density, time step and spatial grid size. The Cahn-Hillard equation (**Eq. 2.30**) and convection-diffusion equation (**Eq. 2.22**) are solved using an RK4 iteration scheme [46]. Implementation details of the hybrid scheme are given in Appendix A. This hybrid scheme's computational speed is fast, but it still retains a high enough accuracy to capture the nematic behaviour [102].

2.3 Active nematics

In this thesis, we study the dynamics of active systems and investigate methods to control them. We focus on the emergent, collective motion of active particles in a fluid, *e.g.* self-propelled swimmers. These swimmers induce far-field hydrodynamic

flows that have nematic symmetry and affect the behaviour of other active particles [113]. This is often called the wet limit of active nematics [24]. The hydrodynamic interactions result in chaotic collective flows, and throughout the thesis, we investigate ways to control these collective flows using their surroundings.

In this section, we introduce the active hydrodynamic stress resulting in the collective dynamics. We start by describing individual active particles as dipole forces. We then derive the active stress from coarse-graining the forces. We demonstrate that this active stress induces a flow with nematic symmetry, plus we show that the stress causes hydrodynamic instabilities, resulting in long-range deformations and nucleation of topological defect pairs. In addition, the active stress and the hydrodynamic instabilities mix the active fluid, resulting in chaotic collective flows. This steady-state is termed active or meso-scale turbulence. We observe the emergence of an intrinsic length scale and mention that this length scale characterises meso-scale turbulent flow and orientation structures. This section helps us understand the emergence of active turbulence and gives us the necessary framework to study the *control* of active nematics.

2.3.1 Individual swimmer

Microscopic organisms swim in the Stokes limit [1]. The forces of a self-propelled particle on the surrounding fluid and vice versa are equal and opposite due to Newton's third law [20]. Hence, in the equation of motion the total momentum density must integrate to zero. The simplest model to describe a swimmer's far-field is by simplifying it as a point that generates dipole forces, which induce a flow field [114].

We can define two basic types of swimmers (**Fig. 2.5**). A pusher-type (**Fig. 2.5**a) effectively pushes liquid forward with its head and backwards with its tail. The associated dipole forces point outwards. To conserve liquid mass, the swimmer sucks in liquid along its waist. Examples of pushers are *E. coli* bacteria [115]. The flows they generate are called *extensile* flows.

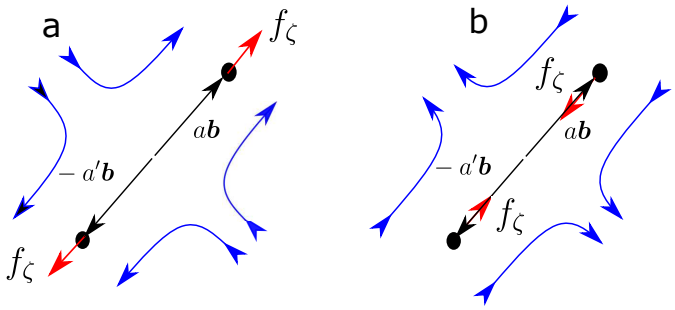

Figure 2.5: Schematic of self-propelled particles. The swimmer is called (a) a pusher particle or (b) a puller particle. To lowest force expansion, a swimmer can be represented as a dipole with two monopole forces $f_\zeta \vec{b}$ (red arrows) at positions $a\vec{b}$ and $a'\vec{b}$ from the centre (black arrows). The flow the swimmer generates around itself is illustrated with blue lines. (a) An example of an extensile system. (b) An example of a contractile system.

A puller-type (**Fig. 2.5**b) pulls liquid in towards its body with their flagella and pushes the fluid outwards along its waist. The dipole forces point inwards. Examples of puller-types are *Chlamydomonas* algae [116]. The flows they generate are called *contractile* flows.

2.3.2 Active stress

The flow generated by a swimming particle is also felt by other swimmers. In the Stokes limit, an active particle's movement will respond to the flow generated by the summation of all the active forces. Hence, we can derive the active stress from coarse-graining the dipole forces of individual swimmers.

We describe an individual swimmer's dipole forces as a sum of two equal magnitude f_ζ forces directed along $\vec{b}$ in opposite directions to satisfy Newton's third law (**Fig. 2.5**). For a collection of self-propelled swimmers with centres of mass at $\vec{r}^{(\alpha)}$ with forces at $\vec{r}^{(\alpha)} + a\vec{b}^{(\alpha)}$ and $\vec{r}^{(\alpha)} - a'\vec{b}^{(\alpha)}$, this yields a force density [20]

$$\vec{\nabla} \cdot \Pi_{\mathrm{Act,f}}(\vec{r}) = \vec{f}_{\mathrm{Act,f}}(\vec{r}) = f_\zeta \sum_\alpha \vec{b}^{(\alpha)} \left(\delta[\vec{r} - \vec{r}^{(\alpha)} + a\vec{b}^{(\alpha)}] - \delta[\vec{r} - \vec{r}^{(\alpha)} - a'\vec{b}^{(\alpha)}] \right). \tag{2.32}$$

We can describe apolar and polar particles by setting $a = a'$ and $a \neq a'$, respectively. If a equals a', the Stokes flow generated at the swimmer's centre of mass $\vec{r}^{(\alpha)}$ by the two monopoles is zero and the individual particle is apolar. Otherwise, there is a self-propelled velocity at the centre of mass $\vec{r}^{(\alpha)}$ and the swimmer is polar.

We expand the delta function in **Eq. 2.32** around $\vec{r}^{(\alpha)}$. This expansion gives [20]

$$\vec{f}_{\mathrm{Act,f}}(\vec{r}) \simeq \frac{a+a'}{2} f_\zeta \vec{\nabla} \sum_\alpha \vec{b}^{(\alpha)} \vec{b}^{(\alpha)} \delta(\vec{r} - \vec{r}^{(\alpha)}) + O(\nabla\nabla) \tag{2.33}$$

for the far-field behaviour, and we recognise the tensor order parameter $\boldsymbol{Q}$ definition of **Eq. 2.2**. We can rewrite **Eq. 2.33** similar to **Eq. 2.3** with a coarse-grained description of the director $\boldsymbol{n}$,

$$\boldsymbol{\Pi}_{\mathrm{Act,f}}(\vec{r}) = -\frac{a+a'}{2} c(\vec{r}) f_\zeta \left(\boldsymbol{nn} - \frac{1}{3}\boldsymbol{I} \right) + O(\nabla), \tag{2.34}$$

where $c(\vec{r})$ contains information about the local concentration and ordering of self-propelled particles. This $c(\vec{r})$ will scale with the scalar order parameter q and concentration ϕ in our framework. We realise that the prefactor $a + a'$ in the leading term of **Eq. 2.34** is the same for polar and apolar particles. This explains the emergence of nematic symmetry in many active systems, even though many individual active particles are polar themselves.

We include this active stress in the momentum conservation equation (**Eq. 2.28**) as

$$\boldsymbol{\Pi}_{\mathrm{Act}} = -\zeta \phi \boldsymbol{Q}, \tag{2.35}$$

where we combine the different prefactors in **Eq. 2.34** to one phenomenological parameter called the activity ζ for simplicity. In most of the following derivations and equations, we omit ϕ from **Eq. 2.35** as we often work with a homogenous fluid, *i.e.* a constant ϕ field. The active particle concentration ϕ is then absorbed into the activity ζ. The parameter ζ determines the phenomenological strength of the active stress with positive and negative values denoting extensile and contractile activities, respectively [24, 39, 53, 56].

2.3.3 Intrinsic nematic ordering

In subsection 2.3.2, we derived the active stress (**Eq. 2.35**), which showed that the flow symmetry is nematic. However, this active stress will be neglectable if the individual dipole directions $\vec{b}^{(\alpha)}$ do not align as $c(\vec{r})$ will be close to zero in that case. Luckily, we can show that the active shear flows induce an intrinsic nematic ordering.

If we assume that the elastic stress is negligible compared to the active stress and that pressure gradients are negligible (compressible limit), we can balance the viscous stress with the active stress and write [117]

$$2\eta \boldsymbol{E} \approx \zeta \boldsymbol{Q}. \tag{2.36}$$

Doing the calculation in the incompressible limit would add additional terms to **Eq. 2.36** and the following equations, but they will not modify this subsection's central message: that active shear flows induce nematic ordering. For simplicity of the presented argument, we have not included the additional terms.

Using **Eq. 2.36** as an equality, we can write **Eq. 2.21** as

$$\left(\partial_t + \vec{u} \cdot \vec{\nabla}\right) \boldsymbol{Q} - \boldsymbol{\Omega} \cdot \boldsymbol{Q} + \boldsymbol{Q} \cdot \boldsymbol{\Omega} = \Gamma \boldsymbol{H}_{\text{Eff}}, \tag{2.37}$$

where $\boldsymbol{H}_{\text{Eff}}$ is the effective molecular field modified by the active flows. We have used two-dimensional symmetry for the derivation of **Eq. 2.37** as this simplifies the presented terms. The corresponding modified effective free energy is

$$\mathcal{F}_{\text{Eff}} = \mathcal{F}_b + \mathcal{F}_g + \frac{1}{2}\left[\frac{\lambda\zeta}{6\mu\Gamma} tr(\boldsymbol{Q}^2) - \frac{\lambda\zeta}{3\mu\Gamma} tr(\boldsymbol{Q}^3) + \frac{\lambda\zeta}{4\mu\Gamma} tr(\boldsymbol{Q}^2)^2\right], \tag{2.38}$$

where $\mathcal{F}_b$ is the equilibrium Landau-de Gennes bulk free energy (**Eq. 2.4**) and $\mathcal{F}_g$ is the distortion energy (**Eq. 2.8**). The last three terms are effective free energy terms due to the active shear flows. As these terms have the same symmetry as the Landau-de Gennes bulk free energy $\mathcal{F}_b$, we see that the active shear flows modify the magnitude of nematic ordering q (**Eq. 2.6**) [117]. If the passive system is in the isotropic state (by modifying the prefactors in **Eq. 2.4**), extensile systems ($\zeta > 0$) with a positive flow-aligning parameter ($\lambda > 0$) can even induce nematic ordering. Similarly, nematic ordering can be induced by flows in contractile systems ($\zeta < 0$) with a negative flow-aligning parameter ($\lambda < 0$). Even though the active shear flows intrinsically induce nematic ordering, we include the extrinsic Landau-de Gennes free energy $\mathcal{F}_b$ (**Eq. 2.4**) throughout this thesis. If we do not include $\mathcal{F}_b$, the relaxation dynamics become ill-defined. See Appendix C.1 for an in-depth justification.

2.3.4 Active nematic instabilities

The intrinsic free energy in **Eq. 2.38** shows that active shear flows can induce nematic ordering and alter the scalar order parameter q. However, this calculation does not indicate what the preferred orientation of the director $\boldsymbol{n}$ is, when nematic order ($q > 0$) is present. As it turns out, the director orientation is inherently unstable to bend and splay deformations (**Fig. 2.2**) when the active stress (**Eq. 2.35**) is included in **Eq. 2.28** [36] in the absence of friction [118].

The hydrodynamic instabilities can be easily illustrated in the compressible limit, where pressure gradients can be ignored. Similar to subsection 2.3.3, we can then assume that we have a balance between active and viscous stresses in **Eq. 2.28**. The instabilities can then be found by assuming that the system is quiescent ($\vec{u} = 0$) and uniformly aligned along the y-axis. We can define a bend perturbation in the director field, moving along the y-axis and generating a flow $\vec{u} = u(y)\vec{x}$. By inserting the solution of the flow $\vec{u}$ into **Eq. 2.21**, we can find to lowest order in wavenumber that the perturbation grows as [36]

$$\partial_t Q_{xy} = \frac{\beta\zeta}{\eta} Q_{xy}. \tag{2.39}$$

The prefactor $\beta > 0$ depends on the scalar nematic order parameter q and flow-aligning parameter λ. Similarly, we can define a splay perturbation moving along the x-axis and generating a flow $\vec{u} = u(x)\vec{y}$, which results in the perturbation growing to lowest order in wavenumber as

$$\partial_t Q_{xy} = -\frac{\beta\zeta}{\eta} Q_{xy}. \tag{2.40}$$

Eq. 2.39 and **Eq. 2.40** illustrate that initial bend (splay) deformations will keep growing for an extensile (contractile) system. For the full derivation of the instabilities in the incompressible limit, we refer to [118].

These deformations eventually grow and localise into wall-like regions of high director distortion [45]. The walls emerge throughout the system with a characteristic spacing between them. This length scale $l_\zeta \sim \sqrt{\frac{K}{\zeta}}$ is due to the injection of energy on the local level, resulting in a balance between activity ζ which wants to

deform the director field and elasticity K which wants to restore it. The derivation of this length scale from the perturbation analysis is quite involved, and beyond the scope of this chapter, but for the interested reader we refer to [36, 118].

2.3.5 Active defects

As the instabilities mentioned in subsection 2.3.4 grow, wall disturbances become confined to thinner interfaces with larger distortions. Due to the localised high distortions, it becomes energetically favourable for the walls to nucleate point discontinuities, creating oppositely charged topological defect pairs that unravel the wall distortions [40].

From the elastic potential between two defects E_{Pair} (**Eq. 2.20**), we would expect it energetically favourable for these oppositely charged defects to immediately annihilate upon creation due to their energy costs. However, in addition to the elastic forces (derivatives of the elastic potential E_{Pair}), topological defect motion is also governed through the active stress (**Eq. 2.35**) in active nematics, which makes defect dynamics non-trivial. The defect dynamics can be described in the form of an overdamped equation of motion if a topological defect is isolated or sufficiently far apart from other defects. The equation of motion for a $+1/2$ defect is then [25]

$$\xi_t \left(\frac{d\vec{r}}{dt} - \vec{v} \right) = -\frac{dE_{\text{Pair}}}{d\vec{r}}, \tag{2.41}$$

with an effective friction coefficient ξ_t and an active backflow $\vec{v}_0$ at the defect centre due to the active stress.

When the flow dynamics are much faster than the orientational dynamics of the director, we can estimate the local flow $\vec{v}$ by realising that it has to obey the Stokes equations [32]

$$\eta \vec{\nabla}^2 \vec{v}_0 - \vec{\nabla} P + \vec{f}_{\text{Act}} = -0, \tag{2.42a}$$

$$\vec{\nabla} \cdot \vec{v} = 0. \tag{2.42b}$$

We assume that the active forces $\vec{f}_{\text{Act}}$ are dominant and are balanced by viscosity dissipation $\eta \vec{\nabla}^2 \vec{v}$ and pressure gradients $\vec{\nabla} P$. The flow for an individual defect

can then be calculated with the Green's function $\boldsymbol{G}$,

$$\vec{v}\,(\vec{r}) = \int dA' \boldsymbol{G}\,(\vec{r},\vec{r}')\,\vec{f}_{\mathrm{Act}}(\vec{r}'). \tag{2.43}$$

In the case of an unconfined 2D system, the Green's function is the two-dimensional Oseen tensor [119].

From the active stress (**Eq. 2.35**), we calculate the active forces for unperturbed $+1/2$ and $-1/2$ defects (**Eq. 2.16**) as

$$\vec{f}_{\mathrm{Act}}(\vec{r}) = \frac{\zeta q m}{r}\begin{bmatrix}\cos\left(\varphi - 2m\varphi\right)\\ -\sin\left(\varphi - 2m\varphi\right)\end{bmatrix}, \tag{2.44}$$

where we set the defect orientation $\vec{p}$ along the x-axis. Inserting the active forces (**Eq. 2.44**) into the solution of the Stokes equation **Eq. 2.43**, yields the velocity profiles

$$\vec{v}_{+1/2}(\vec{r}) = -\frac{\zeta}{12\eta}\begin{bmatrix}3(R-r) + r\cos 2\varphi\\ r\sin 2\varphi\end{bmatrix} \tag{2.45}$$

and

$$\vec{v}_{-1/2}(\vec{r}) = -\frac{\zeta r}{12\eta R}\begin{bmatrix}(\frac{3}{4}r - R)\cos 2\varphi - \frac{R}{5}\cos 4\varphi\\ (-\frac{3}{4}r - R)\sin 2\varphi - \frac{R}{5}\sin 4\varphi\end{bmatrix} \tag{2.46}$$

around unperturbed $+1/2$ and $-1/2$ topological defects, respectively. Here, R is a length scale set to recover the desired behaviour at the boundaries [32]. The analytical flow profiles (**Eq. 2.45** and **Eq. 2.46**) in active nematics are illustrated in **Fig. 2.6**. Experiments in different biological systems including microtubule-kinesin mixtures [28], bacteria [6, 29] and cell monolayers [30] have observed similar collective flow profiles around half-integer topological defects. These similarities indicate that the active stress and forces proposed in subsection 2.3.2 are indeed the dominant terms driving collective dynamics.

We point out that we have a non-zero velocity

$$v_0 = \frac{\zeta R}{4\eta}, \tag{2.47}$$

for a $+1/2$ defect at the defect core ($r = 0$), moving in opposite direction or along the defect vector $\vec{p}$ (**Fig. 2.6**) for extensile or contractile systems, respectively.

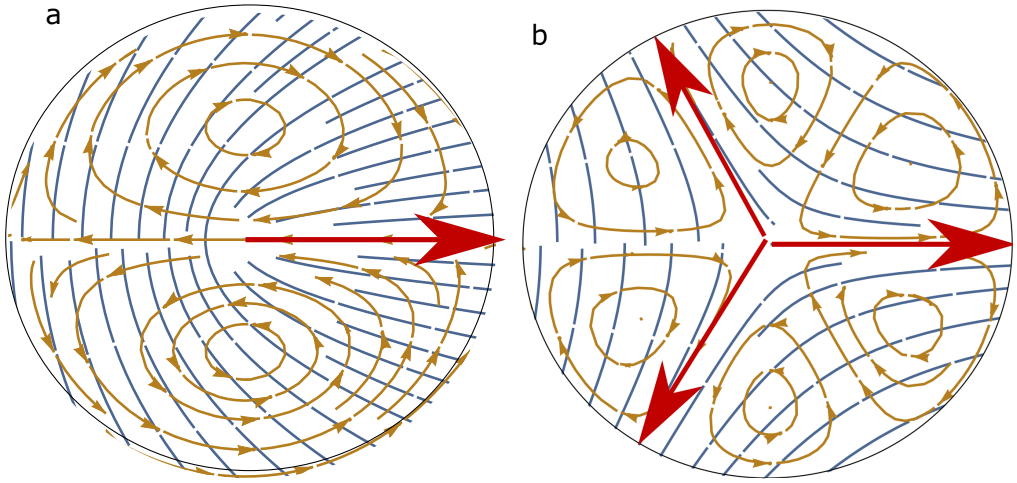

Figure 2.6: The analytical local flow $\vec{v}$ (orange arrows) around half-integer defects in an extensile system for: (a) a $+1/2$ defect and (b) a $-1/2$ defect. The director is drawn with blue lines, and the defect orientation $\vec{p}$ is given with the red arrows. Notice that $\vec{p}$ is not uniquely defined for the $-1/2$ defect.

Different boundary conditions do not affect the shape of this self-propelled velocity, $v_0 \sim \frac{\zeta R}{\eta}$, and this self-motility of $+1/2$ defects is an intrinsic property of active nematics [32]. Depending on the relative orientation, self-motility can overcome the elastic forces between defects ($-\frac{dE_{\text{Pair}}}{d\vec{r}}$), resulting in the possible unbinding of defect pairs and consequently the proliferation of defects in active nematics as they are continously created and annihilated [120].

2.3.6 Active turbulence

On top of the ongoing creation and annihilation of topological defects, the hydrodynamic instabilities lead to chaotic flow patterns with vortices, swirls and velocity jets that are continuously created and destroyed (**Fig. 2.7**). This state is called *active or meso-scale turbulence* [37]. The active turbulent state is highly chaotic and disordered, but the flow and orientation structures scale with the intrinsic active length scale l_ζ [45] mentioned in subsection 2.3.4. This is because energy input happens at the individual particle scale, which is the smallest length scale in the system. This length l_ζ scales with $\sqrt{\frac{K}{\zeta}}$, as activity ζ deforms the director field and elasticity K restores it. This makes active turbulence distinct from traditional high

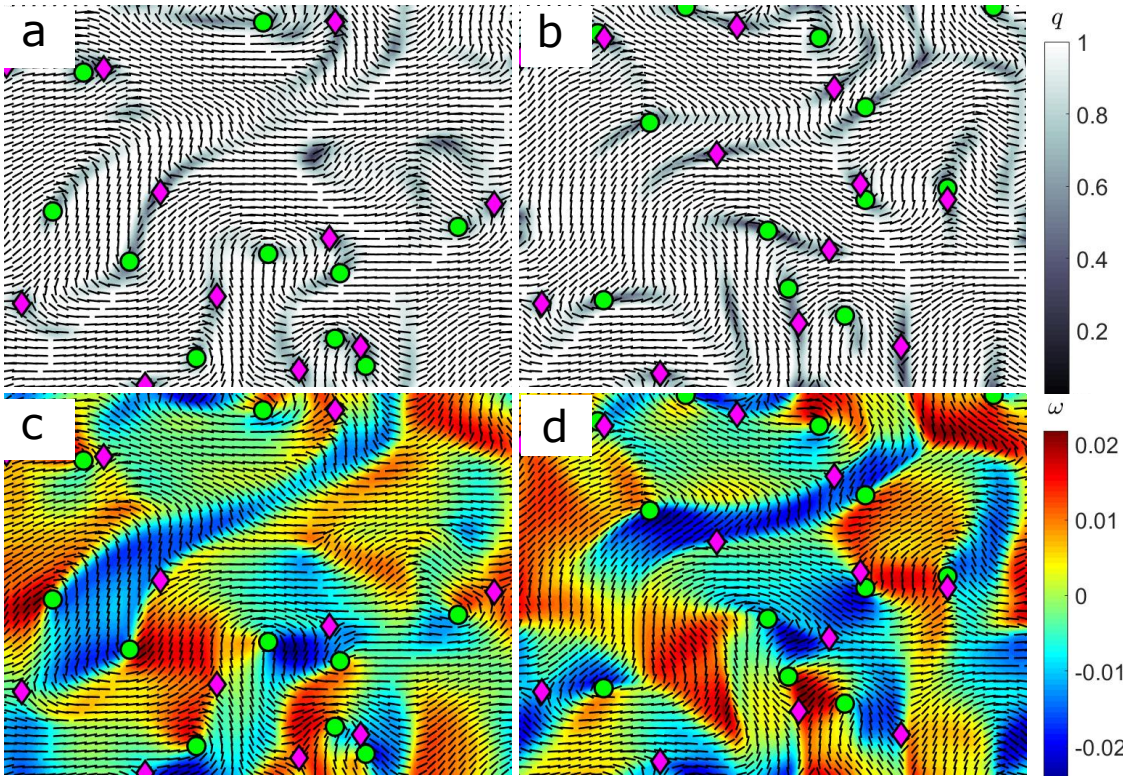

Figure 2.7: Snapshots of simulation results showing meso-scale turbulence in an extensile active nematic. (a,b) Snapshots of the scalar order parameter q at two different time steps in active turbulence. (c,d) Snapshots of the vorticity ω (the curl of the flow field) at two different time steps in active turbulence. The black lines indicate the local director $\boldsymbol{n}$. The green circles (magenta diamonds) mark the $+1/2$ ($-1/2$) topological defects.

Reynolds number turbulence in which energy is injected into the system on the largest length scale, and there is a cascade of length scales [121].

The formation of active turbulence can be suppressed by boundaries [37, 52, 53] or other hydrodynamic screening mechanisms [68]. As flow structures in active turbulence scale with the intrinsic active length scale, we can describe the control and suppression of active turbulence with a dimensionless number. The dimensionless number is a ratio which compares an external hydrodynamic screening length to the intrinsic active length scale, allowing us to describe universal control properties of active turbulence. Taming active turbulence is an active research topic as harnassing the collective dynamics would allow for the creation of microfluidic devices like self-driven micropumps. Additionally, many biological systems that exhibit collective dynamics are not in the bulk active turbulent state, due to

complex surroundings which govern the hydrodynamic interactions. Understanding possible routes for control of active nematics is necessary to understand these complex biological systems.

2.4 Conclusion

In this chapter, we presented the theoretical framework necessary to understand active nematics. We introduced nematic symmetry, described the tensor order parameter $\boldsymbol{Q}$, and summarised topological defects' properties. We described the continuum nematohydrodynamic equations that evolve the nematic tensor order parameter $\boldsymbol{Q}$, the fluid density ρ, collective velocity $\vec{u}$, and active material concentration ϕ.

We then introduced self-propelled particles. We showed that the far-flow field of an individual swimmer has nematic symmetry, and therefore the coarse-grained active stress also has this symmetry. This active stress causes active nematic instabilities, which results in the creation of topological defects and we derived that $+1/2$ defects are self-propelled in active nematics. The instabilities grow with an intrinsic length scale $l_\zeta \sim \sqrt{\frac{K}{\zeta}}$. This intrinsic active length scale results from the competition between activity ζ, which deforms the director field and elasticity K, which restores long-range orientation. In addition, the active hydrodynamic instabilities result in disordered collective flow patterns. This steady state is called active turbulence where the flow structures scale with this intrinsic active length scale (**Fig. 2.7**). We also mentioned that we could characterise the screening of hydrodynamic interactions to suppress active turbulence formation with a ratio between this intrinsic active length scale and an external screening length. This allows us to describe universal control properties of active turbulence.

It's a funny thing, ambition. It can take one to sublime heights or harrowing depths. And sometimes they are one and the same.

Dishonored

3

Twist-induced crossover from two-dimensional to three-dimensional turbulence in active nematics

3.1 Introduction

In Section 2.3, we illustrated that active turbulence emerges in two-dimensional (2D) wet active nematics due to bend or splay instabilities for extensile or contractile systems, respectively [37, 52, 53]. The hydrodynamic instabilities cause deformations in the nematic orientation field to grow, resulting in the emergence and unbinding of point-like topological defects. These point-like defects have chaotic trajectories in active nematics and act as virtual stirring rods in active turbulence [41]. Defect dynamics becomes more complicated in three-dimensional (3D) active turbulence, where the two-dimensional point-like defects extend into the third dimension, thereby forming disclination lines. Recent work has begun classifying active nematics in 3D, where they found the emergence of disclination lines that could contort due to twist deformations driven by active forces [65]. These disclinations can display complex patterns in spherical confinement due to surface and bulk dynamics [63, 64] and are important in the deformation of active droplets [66]. Experiments and simulations

have illustrated that the ratio of higher dimensionality (the aspect ratio of a three-dimensional channel) can significantly alter the dynamics in active fluids [62, 67].

As a step towards further characterising active turbulence in three dimensions, we numerically study in this chapter the crossover from 2D to 3D structures by considering an active nematic fluid confined between two parallel plates (**Fig. 3.1**). We do this by simulating a 3D active nematic between two planar walls with varying interplate distances. As we start to relax the confinement along the third dimension, we find a regime where the active nematic film has a finite thickness, but still behaves like a quasi-2D system. For larger plate separations, we uncover activity-driven twist instabilities in the disclination lines at which the system starts to show 3D properties. This transition occurs at a critical ratio between the intrinsic length scale l_ζ and the plate separation. We show that this critical dimensionless number is independent of the boundary conditions on the surfaces, and argue that the bulk twist deformations drive the transition from quasi-2D dynamics to 3D active turbulence.

3.2 Simulation method

To simulate the crossover from 2D to 3D active turbulence, we solve the nemato-hydrodynamic equations **Eq. 2.21**, **Eq. 2.27** and **Eq. 2.28** that evolve the density ρ, the velocity $\vec{u}$ and the tensor order parameter $\boldsymbol{Q}$ for a weakly compressible active nematic confined between two parallel planar surfaces separated by a varying distance H. In this chapter, the relevant parameter set is the rotational diffusivity $\Gamma = 0.34$, Landau-de Gennes coefficients $\mathcal{A} = 0, \mathcal{B} = -0.3$ and $\mathcal{C} = 0.3$, flow-aligning parameter $\lambda = 0.3$ and viscosity $\eta = 2/3$, which can be mapped to the microtubule-kinesin bundles system [10]. This experimental set-up was mentioned in Chapter 1. A similar parameter regime has been used to study extensile active nematics in 3D microchannels [67]. We focus on extensile active fluids ($\zeta > 0$), relevant to these microtubule-kinesin bundles [10, 12] within the range $\zeta = [0.01, 0.05]$. Unless otherwise stated, we use the one-constant approximation (**Eq. 2.11**), in which all Frank elastic constant values are $K_i = K$, and are varied over the range

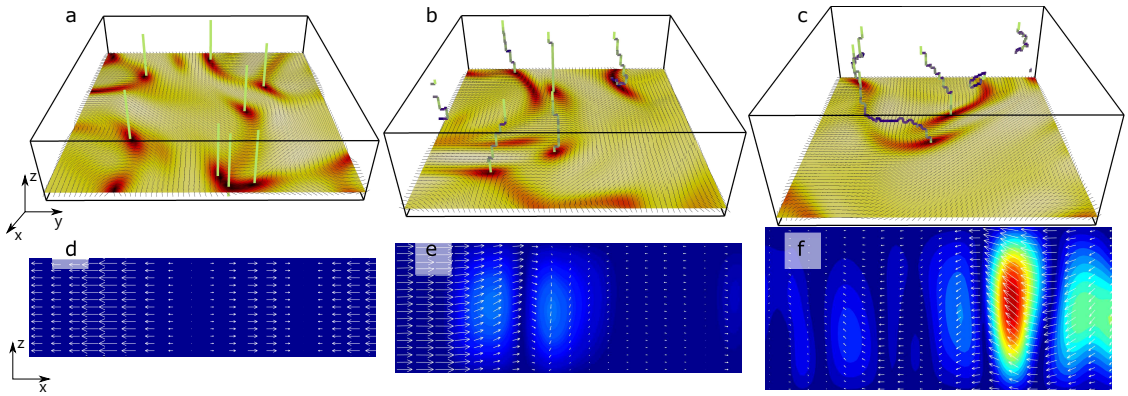

Figure 3.1: Transition to 3D active turbulence. Snapshots of (a,d) quasi-2D, (b,e) transitional and (c,f) 3D active turbulence in confined active nematics. Upon increasing the channel height, the dynamics change from (a) a quasi-2D flow with straight disclination lines for the channel height $H = 15$ ($A = 15$) (b) through a transition regime near $H = 20$ ($A = 20$) to (c) 3D flows with strongly contorted disclination lines for the channel height $H = 25$ ($A = 25$). In the top row (a-c), the planar colourmap illustrates the magnitude of the nematic order q and director field $\boldsymbol{n}$ (solid black lines) in the vicinity of the lower bounding free-slip wall. Disclination lines are shown as thick lines coloured by the characteristic disclination angle α, from wedge-type disclination segments with $\alpha = 0$ (green) to twist-type segments with $\alpha = \pi/2$ (purple). The bottom row (d-f) shows a slice of the velocity fields for the same heights. The length of the arrow indicates the local speed $\vec{u}$, while the colourmap shows the cross-channel component u_z.

$K = [0.01, 0.05]$. When we relax the one constant approximation, we make the simplifying choice $K_{\text{Splay}} = K_{\text{Bend}} = K$ and only vary K_{Twist} (**Eq. 2.10**).

To confine the system in the third dimension, parallel impermeable surfaces are implemented. These surfaces impose strong planar anchoring on the nematic field and free-slip boundary conditions on the velocity except where otherwise stated. Details on the implementation of the boundary conditions are provided in Appendix A.2. Simulations were performed in a cuboid of volume $100 \times 100 \times H$ with periodic boundary conditions in the xy-plane, where the xy-plane is large compared the intrinsic length scale. The planar channel geometry, characterised by the plate separation H, competes with the characteristic length scale of active turbulence $l_\zeta \sim \sqrt{K/\zeta}$ [45, 46], so that the physics can be described by the *dimensionless activity number* $A = H\sqrt{\zeta/K}$.

3.3 Quasi 2D active turbulence

When the channel height H is sufficiently small compared to $\sqrt{K/\zeta}$, the active turbulence is quasi-2D. In this limit, both flow and director fields are height-independent, and topological defects form straight disclination lines normal to the surfaces that directly span the gap with translational invariance across the channel (**Fig. 3.1**a). When observed from above, the disclination lines appear as 2D point defects with half-integer charges $m = \pm 1/2$ (**Fig. 2.3**). Disclinations are continuously created and annihilated, such that in every plane parallel to the channel walls the defect dynamics is effectively that of 2D active turbulence [38, 122].

The flow fields reflect this quasi-2D behaviour for sufficiently small channel heights, showing 2D active turbulence in xy-planes parallel to the wall but translationally invariant across the channel (**Fig. 3.1**d). The turbulent flow dynamics are quantified through the velocity and vorticity correlation lengths, as well as the number density of disclinations (**Fig. 3.2**). The vorticity ω is the curl of the flow in the xy-plane. The velocity ℓ_v and vorticity ℓ_ω length scales are calculated from the the velocity-velocity correlation function $C_{vv}(r) = \langle \vec{u}(r,t) \cdot \vec{u}(0,t) \rangle / \langle \vec{u}(0,t)^2 \rangle$ and vorticity-vorticity correlation function $C_{\omega\omega}(r) = \langle \vec{\omega}(r,t) \cdot \vec{\omega}(0,t) \rangle / \langle \vec{\omega}(0,t)^2 \rangle$, respectively. These length scales are defined as the lengths where the correlation functions are halved. Our measurements in the observed quasi-2D turbulence reveal that the correlation lengths and number density of defects ρ_N are all consistent with 2D behaviour up to certain channel heights.

Although the active turbulence can be described as effectively two dimensional in this limit, indications of the 3D nature of the film remain apparent in the pair-production process. In quasi-2D active turbulence pair-production of effective 2D $\pm 1/2$ defects occurs when a 3D disclination loop forms in the centre of the channel. The small ring inflates until it makes contact with the bounding planar surfaces, at which point it then splits into two straight disclination lines that bridge the gap and appear as the pair of $\pm 1/2$ defects in the xy-plane (**Fig. 3.1**a). Apparent pair-production is a rapid process ($\sim$ 10 simulation time steps) and pair-annihilation events of oppositely charged apparent defects occur analogously,

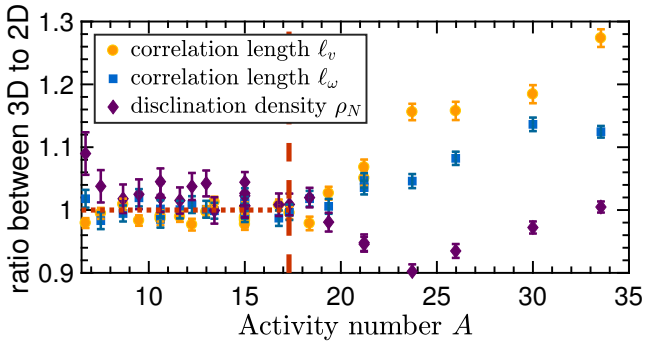

Figure 3.2: Comparison of turbulence properties in 2D and full 3D simulations. Shown are the velocity correlation length ℓ_v, the vorticity correlation length ℓ_ω, and the disclination number density ρ_N in 3D. All values are normalised by their 2D counterpart. The red, dotted line marks the crossover from quasi-2D to 3D active turbulence.

or as horseshoe shaped arches when the annihilating disclination lines make contact at one surface but not the other.

3.4 3D active turbulence

All three characterisations of the flow start to deviate from their 2D values at a critical activity number (**Fig. 3.2**). As the channel height is increased, the system crosses over from quasi-2D to fully 3D active turbulence. At the onset of the 3D behaviour, the disclination lines begin to contort (**Fig. 3.1**b) and the translational invariance of the velocity profile across the channel is lost (**Fig. 3.1**e). Contortion typically occurs near the centre of the channel, while the disclination lines are essentially 2D defects normal to the boundary near the walls (**Fig. 3.1**b,c). The projected positions of the disclination points at the top and bottom walls are separated by a non-zero in-plane distance σ (**Fig. 3.3**a-*inset*). Plotting the ensemble-average of this distance $\langle\sigma\rangle$ against the dimensionless activity number A shows a sharp crossover at a critical activity number (**Fig. 3.3**a), after which the average separation rises continuously from zero as the disclination lines contort. Because this active system is intrinsically out-of-equilibrium, we must be mindful not to think of this transformation of the flow dynamics in terms of a phase transition under equilibrium conditions but rather a dynamic crossover.

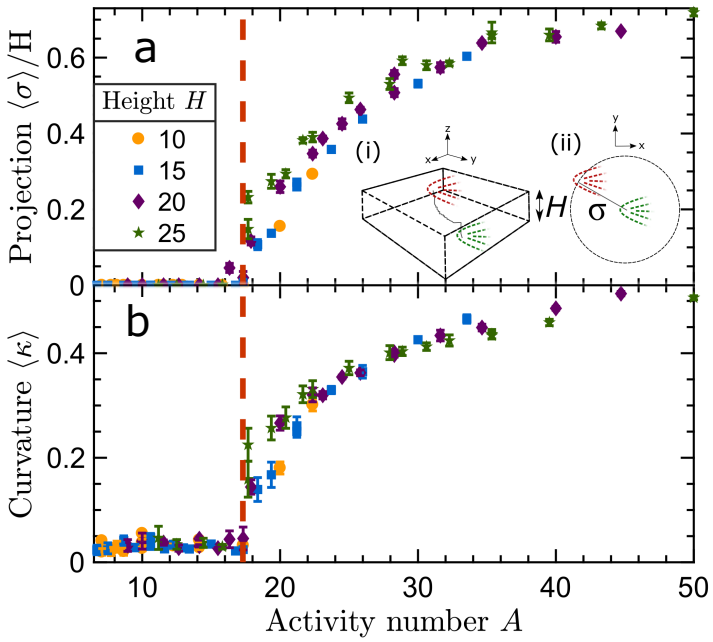

Figure 3.3: Quantifying disclination line behaviour. (a) The average projected distance $\langle\sigma\rangle$ between the ends of the disclinations for free-slip walls as a function of activity number A. *Insets:* Schematic representation of the projected distance between the disclination ends at opposite walls. (b) Mean curvature $\langle\kappa\rangle$ as a function of A.

For simulations with no-slip boundary conditions (**Fig. 3.4**), the transition in the separation of the projected positions of the disclination lines σ is seen to be sharper, but the critical activity is unchanged. This suggests that the nature of the instability that drives the transition from 2D to 3D turbulence is independent of the surface friction and that the breaking of translational symmetry across the channel gap by the no-slip condition causes the transition to rise more abruptly. Likewise the nature of the crossover appears to be unaltered when the simulations do not impose any specific anchoring for the director at the boundaries but rather have free anchoring (**Fig. 3.4**). It was previously shown that the extensile activity generates an effective planar active anchoring [123].

In addition to the average projected distance between the disclination ends $\langle\sigma\rangle$, measurements of the ensemble-average of the mean curvature of the disclination lines $\langle\kappa\rangle$ also show a sharp transition at the critical activity number (**Fig. 3.3**b). This suggests that at the critical activity number, energy injected into the system around disclinations can overcome the elastic energy of the disclination line and

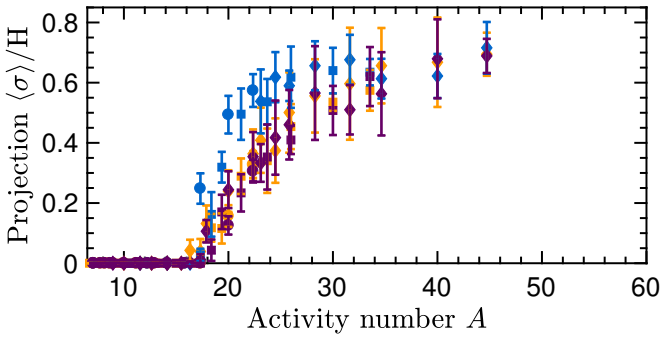

Figure 3.4: The average projected distance $\langle\sigma\rangle$ between the ends of the disclinations as a function of activity number A for various boundary conditions. Walls with free-slip with strong anchoring (yellow symbols) and free-slip with free anchoring (purple) are indistinguishable, but no-slip with strong planar anchoring (blue) rises more rapidly. Three channel heights are varied ($H = 10$: circles; 15: squares; 20: diamonds).

therefore a finite curvature develops along the disclination. At this point, the cross-channel translational symmetry of the flow ceases and 3D active turbulence emerges. Interestingly, both the normalised projected distance and curvature measurements for various channel heights collapse when plotted against the activity number (**Fig. 3.3**), indicating that a constant critical dimensionless activity number $A_{\rm cr} = [H\sqrt{\zeta/K}]_{\rm cr}$ characterises the 2D to 3D crossover.

3.5 Twist instability

In what specific manner does this disclination distortion occur? In 2D films, the deformation of the director field around point defects is set by the splay and bend elastic constants (here assumed to be equal). However in 3D, twist distortions become possible. Therefore to investigate the role of twist in the micro-structure of the disclination lines, we locally classify the disclination-type along each singularity's length. The characteristic disclination angle α is calculated (see Appendix B.2) [124]. This differentiates between pure wedge-type disclinations ($\alpha = 0$), which involve only splay and bend distortions with planar projections of $\pm 1/2$ topological defects, and pure twist-type disclinations ($\alpha = \pi/2$) where the director rotates parallel to the disclination line [125, 126]. The variation of α along the disclinations is shown in **Fig. 3.1**.

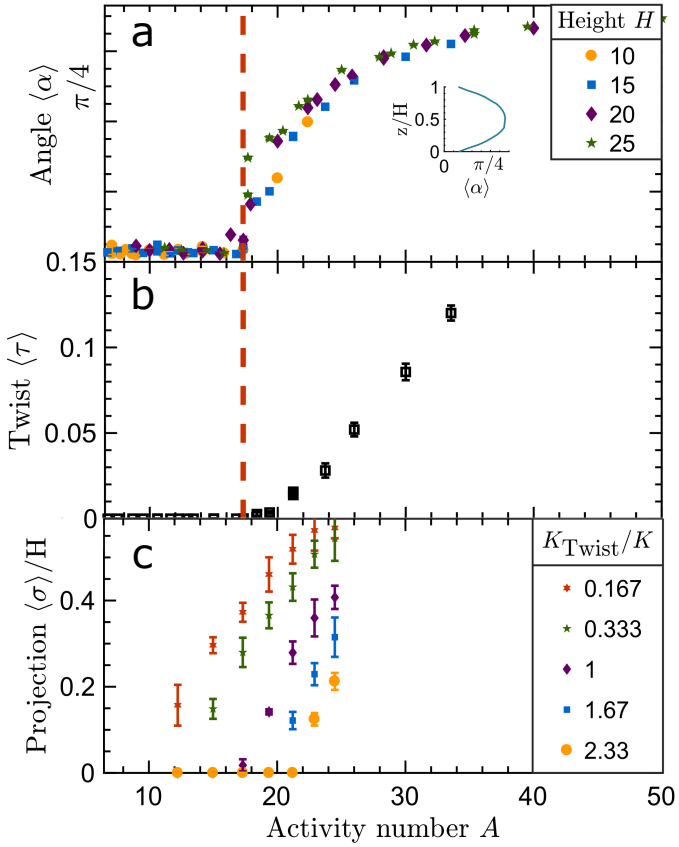

Figure 3.5: The contortion of disclinations are highly correlated to twist deformations. (a) Characteristic defect angle α as a function of activity number A. *Insets:* Angle profile along the defects across the channel for $A = 20$. (b) Global mean twist deformation. (c) Increasing the twist elastic constant suppresses the contortion of defect lines. The activity number A is defined using the bend/splay Frank coefficient K.

Below the critical activity number, the angle averaged over the contour length of all disclination lines $\langle\alpha\rangle$ is close to zero (**Fig. 3.5**a), verifying that in the quasi-2D limit the disclination lines are wedge-type with bend/splay distortions confined to xy-planes. Beyond the critical activity number, however, the curves increasingly transform into twist-type disclinations. The average profile of the disclination angle α at each height through the channel shows a signature of nearly pure wedge-type at the walls and commonly twist-type in the mid-region (**Fig. 3.5**(a)-*inset*). As the activity number is increased, the segment of twist-type disclination near the centreline broadens.

To provide additional evidence of the role of twist, we calculate the system-wide

mean twist deformation [127]

$$\langle \tau \rangle = \frac{1}{q^2} \left(\epsilon_{ikl} Q_{ij} \frac{\partial Q_{lj}}{\partial x_k} \right)^2 ,$$

with ϵ_{ikl} the Levi-Civita symbol. The mean twist becomes non-zero at the transition (**Fig. 3.5**b), where we find that twist is predominantly localised around disclination lines. However, deep in the fully 3D active turbulent regime, the twist deformation increases with activity number throughout the whole domain.

To further check the role of twist in the contortion of disclinations and the subsequent crossover to 3D active turbulence, we suppress the transition by increasing the resistance of the active nematic to twist deformations. To this end, we relax the one-constant approximation for the orientational elasticity and progressively increase the twist coefficient K_{Twist}, while keeping the bend/splay constants equal to K. By increasing the twist elastic constant, the contortion of the disclinations is hampered; consequently, the crossover to 3D is retarded (**Fig. 3.5**c).

3.6 Energy competition

These results suggest that the onset of 3D active nematic turbulence arises from the competition of energies. It is expected that a disclination line maintains its straight configuration when the elastic energy dominates, but contorts when the active energy injection overcomes the elastic energy barrier.

We assume the director configuration around a $+1/2$ disclination line to be $\boldsymbol{n} = [\cos(\varphi/2), \sin(\varphi/2), 0]$ (**Eq. 2.16**), where the factor $+1/2$ is the topological charge of the disclination. Adding a small twist perturbation q_t per unit length along the initially straight line increases both the active energy that is dissipated in the system E_{Act} and the elastic deformation energy E_{Twist}, which resists additional twist deformations. At the onset of the crossover from 2D to 3D behaviour, the director field at height z can be represented as

$$\boldsymbol{n} = \left[\cos\left(\frac{\varphi + q_t z}{2} \right), \sin\left(\frac{\varphi + q_t z}{2} \right), 0 \right] . \tag{3.1}$$

This twist creates a restoring elastic energy

$$E_{\text{Twist}} = \int \frac{K_{\text{Twist}}}{2} \left[\boldsymbol{n} \cdot \vec{\nabla} \times \boldsymbol{n} \right]^2 dV = \frac{\pi K_{\text{Twist}} R^2 q_t^2 H}{8}, \tag{3.2}$$

where we have integrated the twist elastic deformation cost of **Eq. 2.9** over the cylindrical volume V that is deformed by the presence of the disclination. This extends radially from the defect core to a range R, which is set by the average distance between disclinations [42].

Due to the twist perturbation, different segments of the disclination move in different directions as a result of their self-propulsion (**Fig. 3.6**). The relative displacement of a segment at height z with respect to the bottom of the disclination is thus set by the amount of twist at height z and, for small twist $q_t \ll 1$, can be expressed as

$$\Delta\vec{r} = \begin{bmatrix} v_0\tau\left(1-\cos\left(q_t z\right)\right) \\ v_0\tau\sin\left(q_t z\right) \\ 0 \end{bmatrix} \approx \begin{bmatrix} v_0\tau q_t^2 z^2/2 \\ v_0\tau q_t z \\ 0 \end{bmatrix}. \tag{3.3}$$

The magnitude of the displacement $v\tau$, is proportional to the disclination's self-propulsion speed $v_0 \sim \zeta R/\eta$ (see Section 2.3.5) [32] and the elastic relaxation time of the director field $\tau \sim H^2/(\Gamma K)$ [46]. Therefore, $v_0\tau \sim RA^2/\Gamma\eta$, where $\Gamma\eta$ is the ratio of the rotational viscosity of the nematic to the dynamic viscosity. The rotational viscocity scales with the inverse of the rotational diffusivity $1/\Gamma$. In these simulations we use $\Gamma\eta \approx 9/2$. The distortion (**Eq. 3.3**) causes the polar angle of the disclination in the xy-plane to be $\psi = \tan^{-1}\left(\left(y-\Delta r_y\right)/\left(x-\Delta r_x\right)\right)$.

By integrating the active force density $-\zeta\vec{\nabla}\cdot\boldsymbol{Q}$ (**Eq. 2.35**) over a cylinder of radius R and height H around a disclination with orientation as described in **Eq. 3.1**, the active forces per unit length are found to be

$$\vec{f}_{\text{Act}} \approx \pi\zeta R\left[\left(-1+q_t^2 z^2/2\right)\,\hat{\vec{x}} + q_t z\,\hat{\vec{y}}\right]/2, \tag{3.4}$$

where $\hat{\vec{x}}$ is taken to lie in the direction of motion of the bottom point of the disclination line at $z=0$ and $\hat{\vec{y}}$ is orthogonally in-plane (**Fig. 3.6**). We assume that the interaction range is much greater than the defect core and so neglect any contribution from the defect core. When the twist perturbation is zero, we recover the

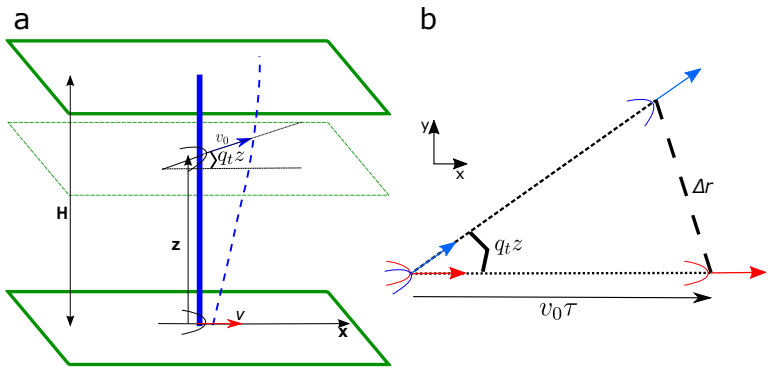

Figure 3.6: Schematic of a twisted disclination line. (a) The solid line is the initial straight line and the dashed line represents the contorted disclination after time τ. (b) Top view of the bottom disclination segment at height $z = 0$ (red) and the top disclination segment at height z (blue). The different segments of the disclination line move with a self-propulsion speed v_0 over a time interval τ (along the dashed line) at an angle $q_t z$ to the x-axis.

known active forces around a 2D point defect that result in self-motility of the $+1/2$ defects (**Eq. 2.44**) [32]. Thus, the first term in the $\hat{\vec{x}}$-component of $\vec{f}_{\mathrm{Act}}$ corresponds to the normal 2D deformation of the director field around a $+1/2$ disclination and the additional terms are due to the twist-induced deformations. Defining the active energy as the active force times the displacement and integrating over the length of disclination, we find the active energy dissipated within the fluid to be

$$E_{\mathrm{Act}} = \int_V \vec{f}_{Act} \cdot \Delta\vec{r} dV \sim \frac{\pi}{6} \zeta R v_0 \tau q_t^2 H^3. \tag{3.5}$$

When the active energy overcomes the restoring elastic deformation energy, twist perturbations grow and the system will not return to a quasi-2D state. Considering these energies leads to a modified activity number

$$A' = H \left(\frac{\zeta}{\sqrt{K K_{\mathrm{Twist}}}} \right)^{1/2} \tag{3.6}$$

that reduces to $A = H\sqrt{\zeta/K}$ in the one-constant approximation $K_{\mathrm{Twist}} = K$. At the crossover, the two competing energies must be comparable and we find

$$A'_{\mathrm{cr}} \sim (\Gamma\eta)^{1/4}. \tag{3.7}$$

Indeed, by measuring the projection distance σ as a function of this modified activity number for varying twist and bend/splay elastic constants, we find that

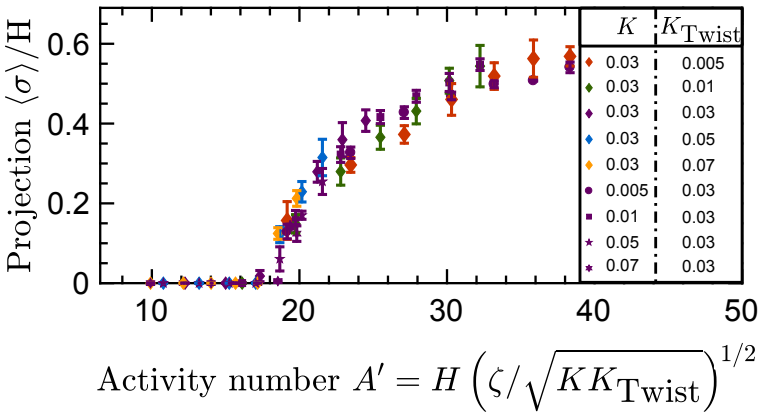

Figure 3.7: The average projected distance $\langle\sigma\rangle$ between the ends of the disclinations as a function of modified activity number A' for varying twist K_{Twist} and bend/splay K elastic constants.

the data collapse onto a single curve **Fig. 3.7**). This shows, in agreement with the theory, that the dimensionless activity number is the control parameter for the transition. Furthermore, it illustrates how the crossover to 3D active turbulence is induced by the competition between distorting active energy injection and the restoring twist elastic energy of the disclination.

3.7 Conclusion

Our results uncover a new physical mechanism in active nematics, showing that the crossover from quasi-2D to confined 3D active nematic turbulence is governed by the contortion of disclination lines above an activity threshold. We show that below this threshold, the system behaves like traditional 2D active turbulence. This confirms that active nematic films with a finite, but thin thickness can be treated like 2D active nematics. The confining length scale stabilises the 2D active turbulence. We show that above an activity number threshold, the activity overcomes elastic twist deformation energy costs, and active forces drive twist deformations around the disclination lines. The role of the activity-driven twist deformations is specific to 3D systems.

We all make choices in life, but in the end our choices make us.

Bioshock

4

Active nematics with anisotropic friction: the decisive role of the flow-aligning parameter

4.1 Introduction

Recent studies have shown that inducing hydrodynamic screening through frictional damping between active materials and their surroundings can stabilise the chaotic flow patterns of active fluids [26, 128]. Of particular interest, recent experiments by Guillamat *et al.* [12] have shown that interfacing microtubule-kinesin motor protein mixtures (see Chapter 1) with a smectic liquid crystal [25], which provide anisotropic damping, can streamline microtubules into a 'laning' state of jets flowing in alternating directions parallel to the anisotropic smectic layers.

In this chapter, we numerically investigate the impact of anisotropic hydrodynamic screening by subjecting a two-dimensional active nematic to anisotropic frictional damping. By systematically varying the strength of the anisotropic friction, we obtain the laning state. We characterise this laning state and map the phenomenological activity ζ to the Adenosine triphosphate (ATP) concentration that induces the active shear flows in the microtubule-kinesin motor protein system [10]. We explain the mechanism for the emergence of lanes in terms of the combined effects

of frictional anisotropy and the active particles' alignment with the extensional velocity gradients, set by the flow-aligning parameter λ. Moreover, by changing the flow-aligning parameter to values deep within the flow-tumbling regime (**Eq. 2.23**), we observe significant changes in the alignment of comet-like (+1/2) topological defects and find an unexpected state of oppositely-charged bound defect pairs that navigate through the system, leaving behind long-lived distortions within the active nematic.

4.2 Simulation method

We solve the nematohydrodynamic equations (**Eq. 2.21**, **Eq. 2.27** and **Eq. 2.28**) for the tensor $\boldsymbol{Q}$, density ρ and velocity $\vec{u}$. The numerical parameters that we use are viscosity $\eta = 2/3$, rotational diffusivity $\Gamma = 0.7$ and pressure $P = 0.25$. We use the single elastic constant approximation with $K = 0.03$ and take the bulk free energy parameters as $\mathcal{A}_0 = 1$ and $\epsilon = 0.35$ in **Eq. 2.7**, resulting in an equilibrium magnitude of the nematic order of $q_0 = 0.24$ (**Eq. 2.6**). These parameters are chosen in the range that reproduces different flow patterns of microtubule-kinesin motor mixtures in confinement [56]. Additionally, we introduce a diagonal friction tensor $\boldsymbol{f}$ in the momentum equation (**Eq. 2.28**) to describes the friction between the active nematic layer and the underlying anisotropic sublayer. The diagonal friction tensor has two components: f_x and f_y. The friction along the y-component of the velocity f_y is set to zero, and the friction along the x-component of the velocity f_x is varied. This results in an easy flow direction along the y-axis. In addition, we vary the activity ζ in this chapter (with a default of $\zeta = 0.03$), to model the experiments by Guillamat *et al.* [12] where they varied the ATP concentration to modify the strength of the collective shear flows. Domain sizes are chosen as 250×250 lattice sites unless stated otherwise in the figure caption, and all simulations are performed with periodic boundary conditions. These domain sizes are many times the intrinsic length scale l_ζ and thus the system reproduces bulk properties.

We also vary the flow-aligning parameter λ, as in experiments the λ depends on the size, aspect ratio, magnitude of the nematic order q, and also interactions

between the nematogens. Indeed, one of the few attempts to extract the flow-aligning parameter, in the wing epithelium of *Drosophila*, has shown that it can have a range of values and even become negative [104]. Therefore it would not be surprising if different experimental systems show distinct behaviours associated with flow-tumbling or flow-aligning behaviour. However, to our knowledge, the role of this parameter has been only marginally explored in most theoretical works and experiments with active nematics. Hence, we vary the flow-aligning parameter, but we typically choose it as $\lambda = 0.7$ or $\lambda = 0.3$, which is deep in the flow-aligning and flow-tumbling regime, respectively (**Eq. 2.23**). Throughout the rest of this chapter, we investigate the effect of λ on the collective flow behaviours when anisotropic damping is present. The general effect of λ on defect dynamics will also be considered in Chapter 5.

4.3 Emergence of laning in the flow-aligning regime

We begin by exploring the dynamics of flow-aligning active nematics ($\lambda = 0.7$), noting that numerical studies of the hydrodynamic screening of active nematics have so far mostly been limited to the flow-tumbling regime [47, 68, 69, 129]. With increasing friction f_x, the active nematic state changes from active turbulence (**Fig. 4.1**a,d), to a laning state of opposing jet flows that are periodically disturbed by the nucleation of pairs of topological defects (**Fig. 4.1**b,e) and then, for higher frictions, to a stable laning state without any defects (**Fig. 4.1**c,f).

To further characterise this behaviour we measure the reduced velocity difference $U = \langle(|u_y| - |u_x|)/u_{\text{rms}}\rangle$ with increasing friction f_x (**Fig. 4.2**a). Here $\langle\rangle$ denotes averaging over space and time. For small friction the velocities in the x- and y-directions (u_x and u_y) are approximately equal and thus $U \sim 0$. Then, as f_x is increased, active flows in the y-direction start to dominate, leading to the emergence of the lanes along the easy flow axis. This is marked by a sharp increase in the velocity difference U. Due to the ordered flow structure found in the laning state, the overall rms velocity u_{rms} of the system is higher than in the state of active turbulence (**Fig. 4.2**a; *inset*).

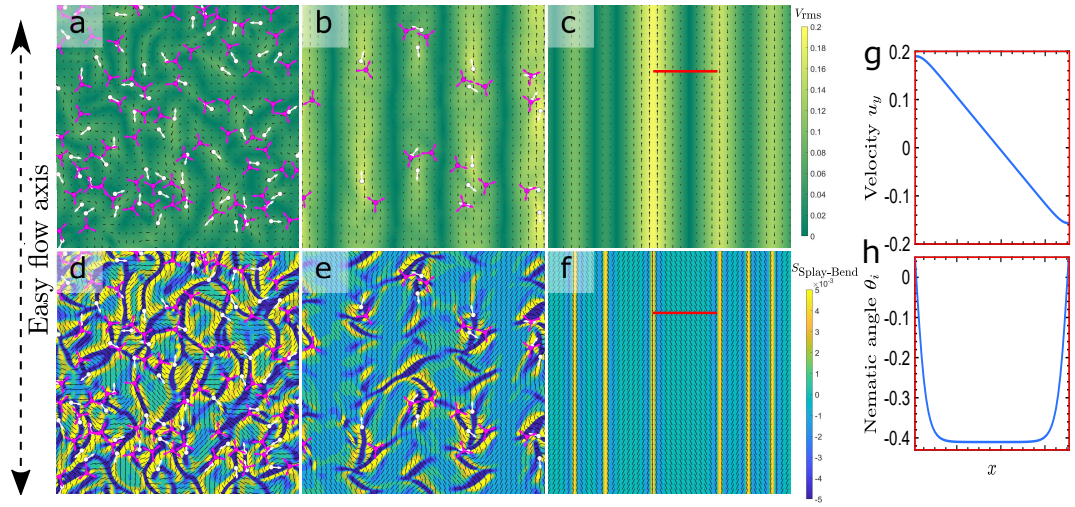

Figure 4.1: Emergence of laning with increasing friction in the flow-aligning regime. Friction is applied along the x-axis making the y-axis the easy flow axis for the flow. (a-c) Velocity field coloured by the magnitude of the rms velocity u_{rms}. (d-f) Director field coloured by the magnitude of the splay-bend order parameter $S_{\text{Splay-Bend}} = \partial_i \partial_j Q_{ij}$. White circles denote $+1/2$ defects with the attached lines indicating their orientation $\vec{p}$ and purple trefoils denote $-1/2$ defects. (a,d) Low friction $f_x = 0.004$, showing active turbulence. (b,e) Intermediate friction $f_x = 0.015$, leading to a laning state with active instabilities. (c,f) High friction $f_x = 0.07$, showing a stable laning state. The activity in (a-f) is kept constant at $\zeta = 0.03$. (g) Variation of the y-component of velocity u_y across a lane (red line in (c)). (h) Variation of the director angle (in radians with respect to the y-axis) across a lane (red line in (f)) reaching the expected Leslie angle of $\theta_L \approx \pm 0.41$ for $\lambda = 0.7$.

At very high friction, the reduced velocity difference U approaches 1, corresponding to zero velocity along the x-axis. However, the rms velocity u_{rms} remains constant in the laning state. The flow in the laning state only travels along the easy-axis, and an increase in anisotropic friction does not correspond to larger screening of the velocities. This is in stark contrast to isotropic friction and the corresponding wet to dry active nematic transition [47], which is further studied in Chapter 6.

We also measured the director-director correlation function

$$C_n(\delta x) = \frac{\left\langle \boldsymbol{n}(x,y) \cdot \boldsymbol{n}(x+\delta x, y) - \frac{2}{\pi} \right\rangle_y}{\left\langle \boldsymbol{n}(x,y) \cdot \boldsymbol{n}(x,y) - \frac{2}{\pi} \right\rangle_y} \tag{4.1}$$

in **Fig. 4.2**b. Because of the nematic symmetry, we subtract $\frac{2}{\pi}$ to make sure that the correlation function goes to zero when there is no-long range correlation and $\langle\rangle_y$ denotes averaging over time and over the y-coordinate. The oscillations

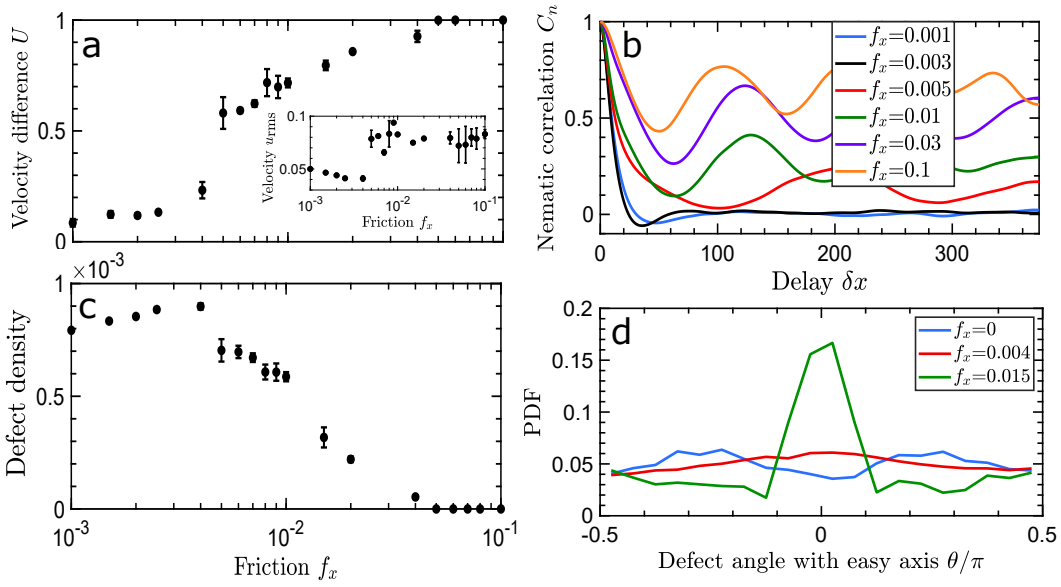

Figure 4.2: Flow-aligning regime. (a) With increasing friction, the reduced velocity difference $U = \langle(|u_y| - |u_x|)/u_{\rm rms}\rangle$ increases from close to 0 (meaning that the velocities in x- and y- directions are approximately equal) to 1 in the state where the flow is directed solely along the y axis. The inset shows the system averaged rms velocity $u_{\rm rms}$. (b) Director-director correlation function for a range of frictions. Domain size for this figure was chosen as 750×250 lattice sites where we tripled the domain size along the anisotropic friction axis. (c) With increasing friction, the average number of defects decreases, dropping to zero in the stable laning state. (d) Histogram of the $+1/2$ defect orientation for $f_x = 0$ (blue), $f_x = 0.004$ (red) and $f_x = 0.015$ (green). With increasing friction, the defects have a strong preference to align and move in the positive or negative y-direction along the easy flow axis. The activity is kept constant at $\zeta = 0.03$ in all graphs.

observed in this correlation function indicate that alternating ordered structures are formed, which correspond to the repeating anti-parallel flow lanes. The distance between the lanes decreases with increasing friction as marked by the reduction of the oscillation wavelength at higher friction values.

The active turbulent state is characterised by topological defects in the director field, and in **Fig. 4.2**c we show that the average number of defects starts to decrease at the onset of laning. A similar decrease in the defect number has been seen for isotropic friction [47]. The defects are responsible for generating flows along the x-axis, and their number dropping to zero coincides with perfect laning: flows only along the y-axis (**Fig. 4.1**f). Moreover the $+1/2$ defects orient more strongly in the y-direction with increasing friction (**Fig. 4.2**d) because of less resistance to

their self-propulsion along the y-axis. Similar alignment is observed for one of the three arms of the $-1/2$ defects. The preferential alignment of motile defects to the direction of lower friction has recently been reported in [69], but since that work focused on the flow-tumbling regime, no laning state was observed.

A defining feature of the laning state is diagonally-aligned nematic domains separated by straight splay-bend walls (**Fig. 4.1**c,f). The existence of these structures is highlighted with the splay-bend order parameter $S_{\text{Splay-Bend}} = \partial_i \partial_j Q_{ij}$ [127]. This configuration can be explained in terms of the director response to activity-induced flows in the presence of anisotropic friction. Stresses associated with director gradients at the splay-bend walls drive anti-parallel flow lanes. Within the lanes, the director responds to the extensional part of the flow and aligns at a particular orientation with respect to the shear following the Leslie angle, which is $\theta_L \approx \pm 0.41$ for $\lambda = 0.7$ with respect to the x-axis [52]. We conjecture that this could allow for the extraction of the flow-aligning parameter from experimental active systems. The elastic interactions favour nematic alignment, and hence a uniform shear (**Fig. 4.1**g,h). Similar director and flow profiles are seen at the onset of flow in confined active nematics [52, 102].

Experimentally, a laning state has been reported in two-dimensional microtubule-kinesin mixtures in contact with a passive smectic liquid crystal [12]. A smectic liquid crystal is a spatially ordered liquid crystal. In a smectic, particles stratify into discretised layers which can freely slide over one another [25]. When the passive liquid crystal is in this smectic phase, a magnetic field can be used to align it such that the normal to the smectic layers lie parallel to the active nematic film. The passive liquid crystal flows much more easily along the smectic layers than perpendicular to them. Consequently, the frictional damping of the active nematic, due to the neighbouring smectic is anisotropic [130] and lanes form along the easy direction, parallel to the smectic layers. It is interesting to observe that, at least in these experiments, the active material is behaving as a flow-aligning nematic as we show in Section 4.4 that lowering the flow-aligning parameter dramatically

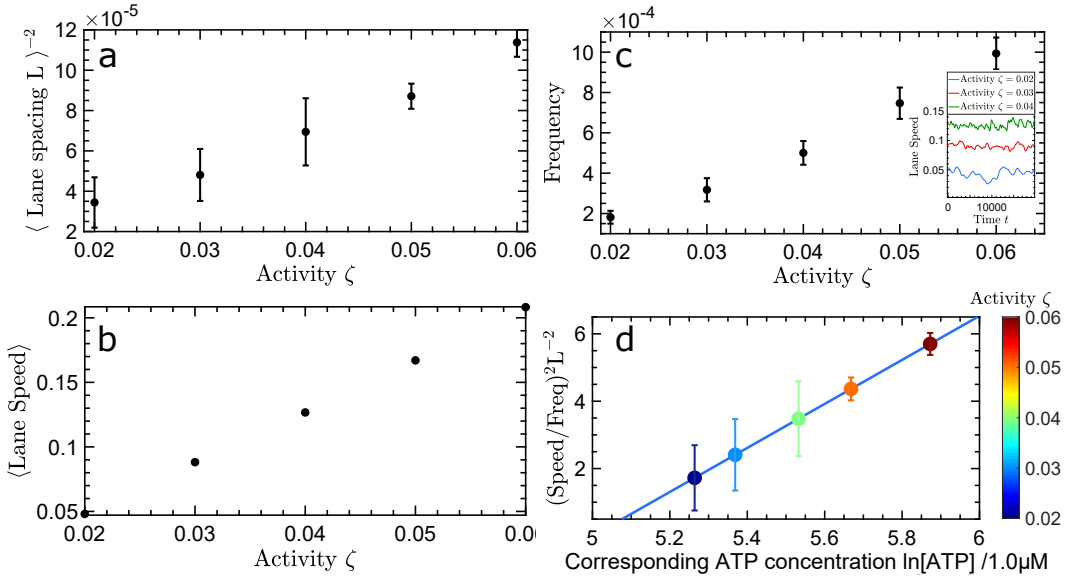

Figure 4.3: Characterising the laning state at intermediate friction $f_x = 0.015$. (a) The distance between the lanes as a function of activity ζ. (b) The average speed of the active nematic in the lanes as a function of activity ζ. (c) The lanes still exhibit periodic instabilities due to defect creation events, resulting in fluctuations in the speed of the lanes. The mean frequency of this signal (inset) is dependent on the activity ζ. Figures (a-c) show linear dependencies with the activity corresponding to the experimentally reported relationships with the log ATP in [12]. (d) Non-dimensionalising the numerical results (the circles) for different activities and comparing them with the experimental data (blue lines) allows us to find the ATP concentration in a two-dimensional microtubule-kinesin mixture which correspond to the values of the active stress parameter ζ used here. Experimental data retrieved from [12].

changes the behaviour of an active nematic system in the presence of anisotropic friction and destroys the laning state.

In **Fig. 4.3**, we concentrate on an intermediate friction value $f_x = 0.015$ (**Fig. 4.1**b,e) that corresponds to a laning state, which is periodically disturbed by defect formation as seen in the experiments [12]. At this friction the spacing between the lanes L scales inversely with the square root of activity $\zeta^{-0.5}$ (**Fig. 4.3**a), which is typically found in active hydrodynamic instabilities resulting in the formation of walls [122]. Increasing the active stress also results in an increase in the overall speed of active material along the lanes. The anisotropic friction suppresses any secondary lateral instability of the walls [123], by hampering deformations and flows perpendicular to the walls. This results in stabilisation of the laminar flow as long-lived lanes. In agreement with the experimental observations [12], unzipping of the

walls is still sometimes observed as, for this friction value, defects are continuously created and annihilated within the lanes. However, due to the suppression of the secondary instability, the walls are not destroyed. The frequency of the defect creation instability scales with the activity ζ and results in fluctuations in the speed of the lanes (**Fig. 4.3**c), which is consistent with the experimental measurements of the fluctuations in the speed and the frequency of these fluctuations [12]. However, in our system, as previously remarked, further increasing the friction will suppress the formation of these defects and result in the system getting stuck in a state where the spacing between lanes is sporadic.

In addition to observing a similar qualitative behaviour as in the experiments, the quantitative measurements of the spacing between the lanes, the velocities within the lanes, and the frequency of the periodic instabilities within the lanes, allow us to map the activity coefficient ζ to the Adenosine triphosphate (ATP) concentration used in the experiments. To this end, we define a dimensionless parameter based on the measurements of the speed, frequency and the length scale associated with the spacing between the lanes: $\Lambda = (\text{Speed}/\text{Freq})^2 / L^2$. It is expected that the activity coefficient is proportional to the chemical potential of ATP hydrolysis $\zeta \propto \ln(\text{ATP})$ [39]. As such comparing the dimensionless number Λ extracted from the experiments as a function of $\ln(\text{ATP})$ with that from the simulations for different values of activity ζ (**Fig. 4.3**d) results in a direct mapping of the activity coefficient to the ATP concentration used in the experiments [12].

4.4 The flow-tumbling regime

The crossover from flow-aligning to flow-tumbling should occur at the effective flow-aligning parameter value $9q/(3q+4) \approx 0.47$ (**Eq. 2.23**) [101]. This definition depends on the value of the nematic order q. For high activity systems, q increases from its equilibrium value [117]. As a result, the transition from flow-aligning to flow-tumbling does not occur exactly at the calculated equilibrium parameter in **Fig. 4.4**a,b, but at a slightly higher flow-aligning value. In the flow-tumbling regime, the director rotates in shear flows and therefore the laning state is expected

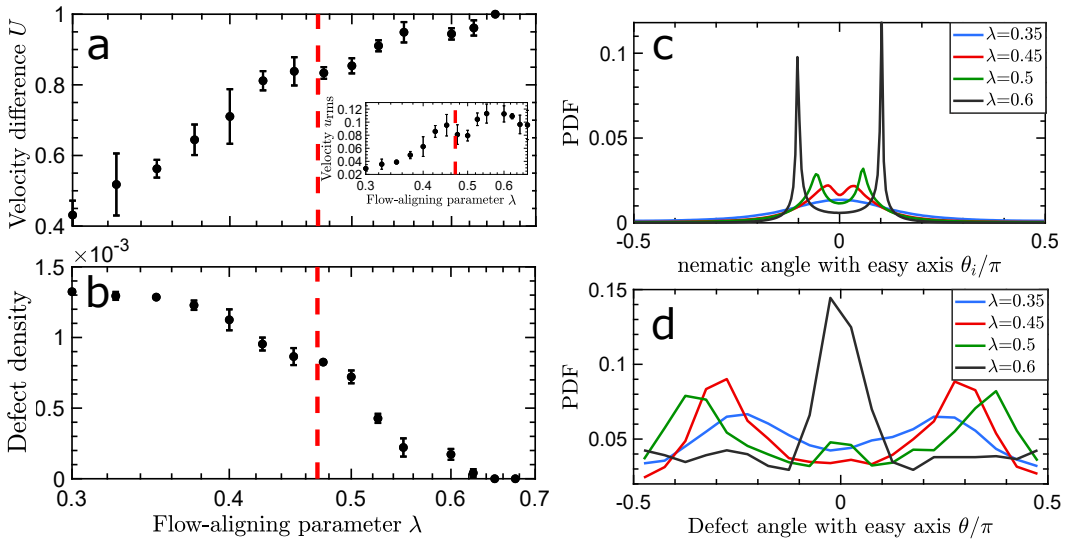

Figure 4.4: Varying the flow-aligning parameter. (a) The reduced velocity difference U as a function of the flow-aligning parameter with rms velocity in the inset. (b) Average number of defects as a function of the flow-aligning parameter. The dashed red line in (a,b) indicates the effective flow-aligning parameter $9q/(3q+4) \approx 0.47$ transition point, corresponding to the crossover from flow-tumbling to flow-aligning behaviour. (c) Orientation of the nematic director relative to the easy flow axis for different flow-aligning parameters. (d) Histograms of the defect orientation for different flow-aligning parameters. For large flow-aligning parameters, defects move mostly along the y-axis, but additional peaks appear around $\theta \sim \pm 0.2\pi$ for smaller flow-aligning parameters.

to be unstable. To investigate this, we fix the friction to $f_x = 0.1$ and the activity to $\zeta = 0.06$, while we reduce the flow-aligning parameter. As evident in **Fig. 4.4**, both the velocity difference U and the rms velocity u_{rms} decrease as the flow-aligning parameter is reduced (**Fig. 4.4**a), while the number of topological defects increases from its zero value in the laning state (**Fig. 4.4**b). The director moves away from the Leslie angle to a more isotropic distribution, but with the expected preference for the easy flow axis (**Fig. 4.4**c).

An interesting change in the behaviour of the system with decreasing flow-aligning parameter is observed in the angular distribution of the motile +1/2 defects (**Fig. 4.4**d). We showed that for large flow-aligning parameters, where the system is in the flow-aligning regime and the laning state is established, the defects are mostly oriented along the easy flow axis. This is marked by a single peak in the defect angle distribution (**Fig. 4.4**d; *black solid line*). However, as the flow-aligning parameter is reduced, two additional peaks appear in the histogram.

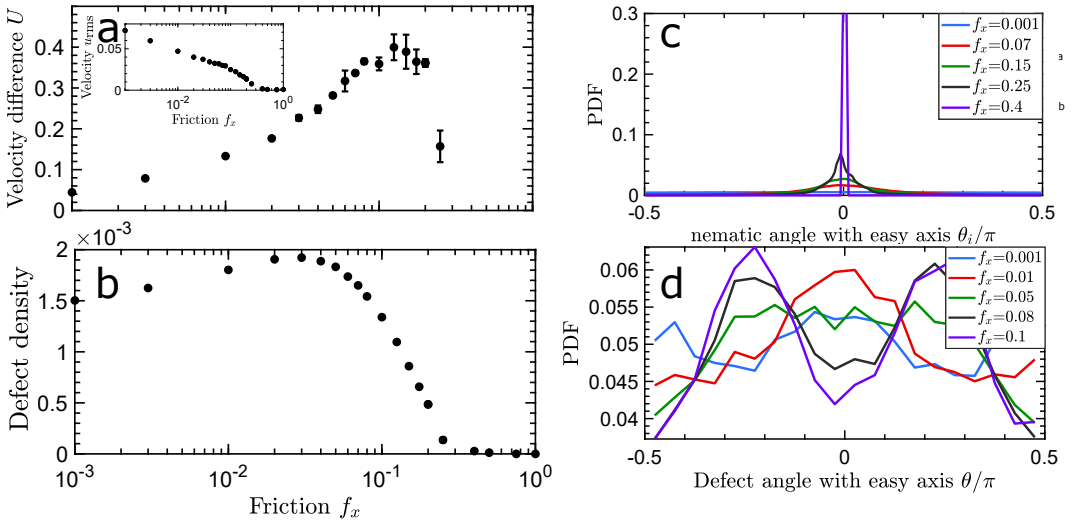

Figure 4.5: Flow-tumbling regime. (a) The reduced velocity difference U as a function of the friction with rms velocity in the inset. Velocity difference U increases with increasing friction until the friction becomes so strong that any flow is suppressed in the system, and the reduced velocity difference becomes ill-defined. (b) Average number of defects as a function of the friction. (c) Orientation of the nematic director relative to the easy flow axis for different frictions. (d) Histograms of the $+1/2$ defect angle for different frictions. At large friction, the defects start moving preferentially at a given angle with respect to the easy flow axis, which is illustrated by peaks forming at different positions.

These correspond to defects moving at some angle with respect to the y-axis. At yet smaller flow-aligning parameters, where the reorientation of the director is predominantly controlled by the rotational part of the flow gradient, any preference for moving along the y-axis disappears, and only two peaks remain (**Fig. 4.4**d; *red, blue solid lines*). This occurs when flows in x-direction are dissipated quickly, strongly suppressing self-motility of $+1/2$ defects along x. At the same time, the flow-tumbling behaviour of the active nematic means that the $+1/2$ defect aligned along y wants to rotate. These two counterbalancing effects lead to a state where defects travel at a preferred angle with respect to the y-axis.

In order to further check the behaviour of the active material in the flow-tumbling regime, we next fix the flow-aligning parameter to $\lambda = 0.3$, the activity to $\zeta = 0.06$, and vary the friction. The rms velocity steadily decreases with the increase in friction (**Fig. 4.5**a) and, after an initial increase, the number of topological defects falls to zero (**Fig. 4.5**b). The reduced velocity difference U increases initially, but then starts to drop down and eventually becomes ill-defined as the rms velocity

goes to zero. The director field gradually develops a preference for the easy flow direction until, for sufficiently strong friction, tumbling is suppressed and nematic alignment is imposed by the flow (**Fig. 4.5**c). In **Fig. 4.5**d, we show the orientation of the defects as a function of friction. Again for higher frictions the two-peak structure is clearly visible. For lower frictions the self-propulsion defect velocity dominates and they tend to move along the easy flow axis.

4.5 A state of oppositely-charged bound defect pairs

If the activity is lowered further within the tumbling regime a new feature appears in the defect dynamics (**Fig. 4.6**a-c). There is a breaking of the mirror symmetry and only one preferred angle is observed (**Fig. 4.6**e; *green, black and purple lines*). In order to better understand how this mirror symmetry-breaking mechanism works, we next focus on the high friction regime and very small activities such that only a few defects are created within the director field and their dynamics can be closely monitored (**Fig. 4.6**d). Upon nucleation of defect pairs - along the direction with lower friction (y-direction) - the defects initially move away from each other, trying to unbind. However, the activity is too weak to overcome the elastic attraction and the defect pair remains bound. At the same time, since the system is in the flow-tumbling regime, the defects slightly rotate relative to each other, so that the line of director distortions in between the defects is no longer along the y-direction. The bound defect pair starts moving as a single object at an angle with respect to the y-direction, with the $+1/2$ defect dragging the $-1/2$ defect behind. The director distortions between the defects appear as 'scars' on the background nematic ordering (**Fig. 4.6**a-c).

With time an additional defect pair can be nucleated at a scar, with the new $+1/2$ defect annihilating the original $-1/2$ defect, and the new $-1/2$ defect binding to the original $+1/2$ defect. Increasing activity leads to a larger number of defect nucleation events and shorter distances between the defects in a bound pair (**Fig. 4.6**a-c,f). The scarred defects are descendants of an original defect pair, and

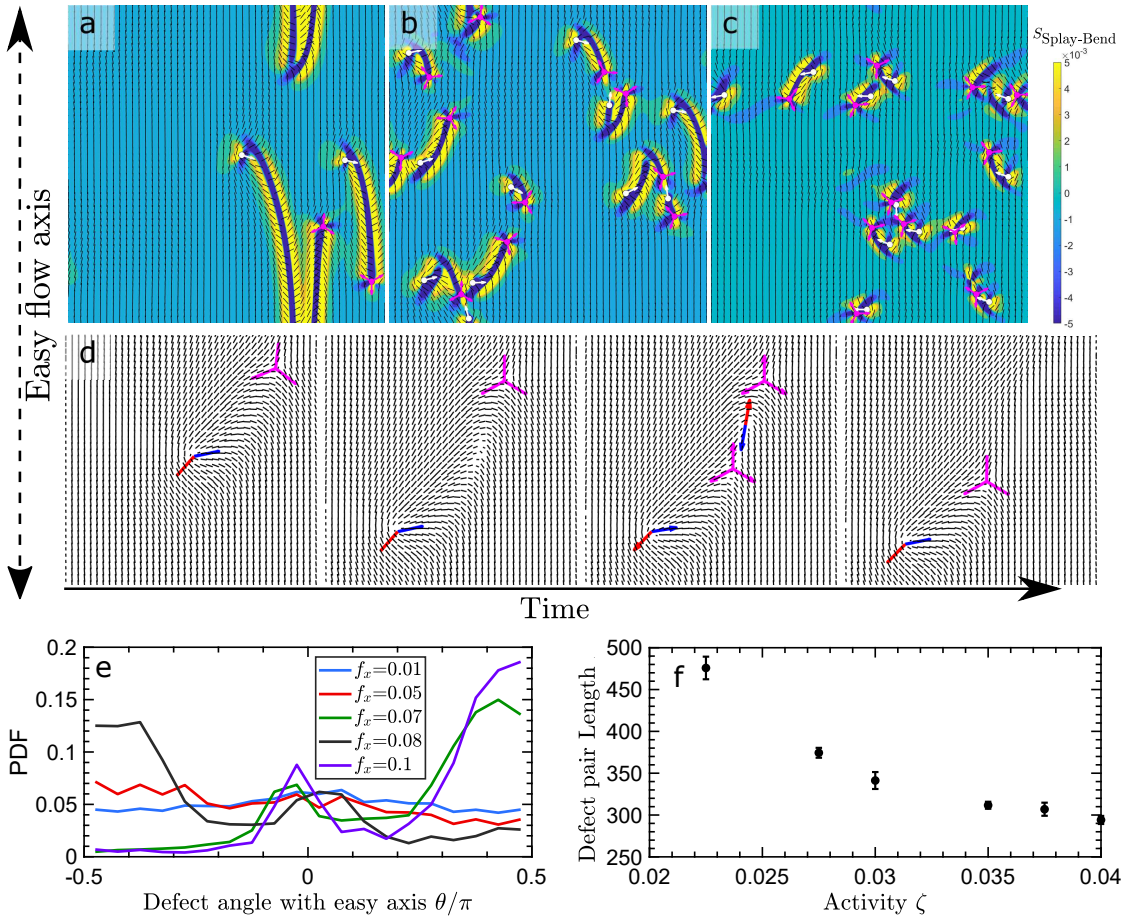

Figure 4.6: Bound defect pairs at low activities. (a-c) Snapshots of different bound defect states at different activities: (a) $\zeta = 0.0175$, (b) $\zeta = 0.0275$ and (c) $\zeta = 0.0375$. Friction is $f_x = 0.3$. White lines denote the orientation of $+1/2$ defects $\vec{p}$ and purple trefoils denote the $-1/2$ defects. (d) Simulation results showing the propagation of a defect pair with time. Red (blue) arrows show the $+1/2$ defect velocity direction (orientation $\vec{p}$). Purple trefoils denote the $-1/2$ defects. Simulation values are $\zeta = 0.04$ and $f_x = 0.5$. Snapshots are taken at times 0, 1700, 1800 and 2000. (e) Histogram of the defect angles for different frictions. For higher frictions the system spontaneously breaks symmetry with scars between the defects in the nematic ordering. The defects prefer either a clockwise or an anticlockwise angle with respect to the easy flow axis. (f) The length of scars. This is calculated by calculating the area where the bend-splay order parameter $S_{Splay-Bend} < -0.01$ and then dividing by the number of defect pairs.

due to the frictional damping, they retain the original orientation after creation. This results in the scars tending to point in the same direction over long time scales. The scar dynamics is reminiscent of the polar ordering of $+1/2$ topological defects that was observed in a study of over-damped active nematics with broken Galilean invariance [131]. Similarly, they are also reminiscent of the memory effect in wet nematics which can cause the formation of arch-like structures and long-range polar

ordering of defects deep in the flow-tumbling regime [118].

4.6 Discussion

The results presented in this chapter demonstrate the important interplay between the flow-aligning behaviour of active particles and anisotropy in hydrodynamic screening. By varying the flow-aligning parameter from flow-aligning to flow-tumbling, we are able to consolidate different observations of active nematic behaviour in anisotropic environments including the laning state in the flow-aligning regime and preferential alignment of +1/2 defects in the flow-tumbling regime. Moreover, when the nematic is flow-tumbling, and at low activities, we identify long-lived and motile bound defect pairs that spawn new pairs and that appear as scar-like distortions within the otherwise aligned nematic.

In order to more clearly summarise and distinguish the different behaviours observed, we generate wind rose plots of the +1/2 defect alignment with respect to the direction with lower friction and coloured by the angular mismatch between the alignment of the +1/2 defect and the direction in which it moves (**Fig. 4.7**). In the absence of any friction anisotropy, the angular distribution would be uniform and the +1/2 defects self-propel along their direction of alignment (mismatch angle will be identical to zero) regardless of the flow-aligning parameter.

Let us begin with the flow-aligning case and increasing friction: at low friction (**Fig. 4.7**a) the angular distribution of +1/2 defects is uniform as expected, but due to the active turbulent flows there is the possibility of mismatch between a defect's orientation and its velocity. This starts to change as the friction anisotropy is increased, such that at the onset of lane formation (**Fig. 4.7**b), defects show a higher tendency to be aligned along the easy flow axis, and they predominantly move along this direction. Deep into the laning state (**Fig. 4.7**c) the majority of +1/2 defects align along the easy flow axis, and any mismatch between their orientation and their velocity is greatly diminished. There is also a small number of defects pointing perpendicular to the easy flow axis. These are defects just after nucleation events, where the wall formation results in the orientation of the defects being

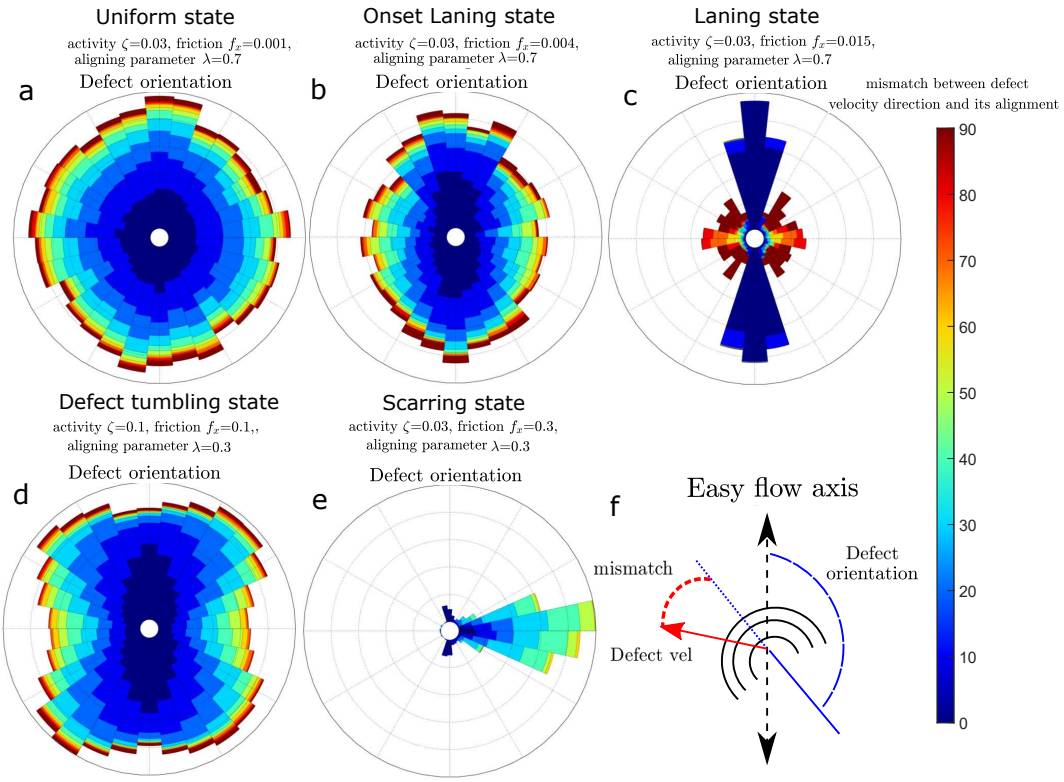

Figure 4.7: Wind roses of the different states. The +1/2 defect orientation $\vec{p}$ and its mismatch with the velocity orientation at the defect core (colourmap) for (a) small friction anisotropy, (b) just at the onset of the laning state, (c) for the stable laning state, (d) within the tumbling regime, and (e) for the scarring state. (f) Schematic showing the quantities of interest for the measurements in (a-e).

perpendicular to the easy flow axis. However, due to the large velocity gradients in between the lanes, these defects rapidly turn to align with the easy flow axis.

A different behaviour of the active defects is observed in the flow-tumbling regime (*bottom row in* **Fig. 4.7**). At low friction anisotropy and high activity the +1/2 defects predominantly align and move along the easy flow axis and two other preferred directions (**Fig. 4.7**d). This is consistent with the behaviour reported in [69] and is due to the balance of the friction anisotropy trying to reorient defects along the easy flow axis with the flow-tumbling behaviour. Increasing the friction anisotropy and reducing activity dramatically changes this picture (**Fig. 4.7**e). The +1/2 defects align predominantly away from the easy flow axis, but move at an angle that has a large mismatch with their alignment, creating the scarring state introduced in Section (4.5).

It is noteworthy that we do not observe a laning behaviour for contractile active nematics with positive flow-aligning parameter as the splay deformations that form at the centre of the lanes are unstable for contractile stresses. On the other hand, the possible reverse case of the stabilisation of bend at the centre of the lanes does not work since this would result in the situation that the nematic director and the velocity orientation are perpendicularly orientated, which is not stable due to the flow-aligning effect. Therefore, in the contractile case, we retain the active chaotic flows with increasing anisotropic friction. The defects become more aligned, similar to the results found in [69], until the flows are completely killed due to very high frictional damping.

4.7 Conclusion

We have numerically investigated the impact of anisotropic hydrodynamic screening on the behaviour of active nematics by imposing anisotropic friction between an active nematic and its surroundings. We find that competing effects between the torques induced by frictional anisotropy and the flow-induced torques result in dynamics that are strongly sensitive to the flow-aligning parameter that characterises the aspect ratio of elongated particles. At high values of the flow-aligning parameter, where the orientation of particles is predominantly affected by the extensional flows, we recover and explain the laning state previously reported in microtubule-motor protein mixtures in contact with a smectic liquid crystal [12]. From this, we have shown that it would be possible to extract the flow-aligning parameter and get an estimate of the corresponding active stress from experimental data. As the alignment parameter is reduced to values corresponding to the flow-tumbling regime, in which rotational flows predominantly determine particle orientations, we observe a dramatic change in the flow and defect patterns. The laning state disappears and the self-propelled $+1/2$ defects align along specific orientations relative to the direction of the friction anisotropy. Furthermore, at low flow-aligning parameter values and small activities, we find a peculiar arrangement of topological defect pairs, where bound $\pm 1/2$ topological defects navigate through the otherwise aligned

active nematic, breaking the mirror-symmetry of the system and creating scar-like distortions in the director field. In addition to confirming the mechanism of previous experimental observations, our work could motivate new sets of experiments exploring the effects of the flow-aligning parameter on the patterns of motion in active nematic materials as our results show that the flow aligning parameter results in distinct behaviours associated with flow-tumbling or flow-aligning behaviour.

But who prays for Satan? Who in eighteen centuries, has had the common humanity to pray for the one sinner that needed it most?

Mark Twain

5

Binding self-propelled topological defects in active turbulence

5.1 Introduction

So far, we have focused on the dynamics of *half-integer* strength discontinuities. While +1/2 topological defects are prolific in active nematics [24], the understanding of *full-integer* defects remains obscure. In fact, in two-dimensional nematic layers and in the absence of any specified anchoring at the boundaries, the simple energy calculation in **Eq. 2.19** shows that two half-integer defects cost less elastic energy than one full-integer defect. Therefore, any full-integer defect should be inherently unstable [31]. Yet, in this chapter we show that in active nematics, self-propelled +1/2 defects can come together to form virtual full-integer defects in the form of asters and vortices (**Fig. 5.1**). Importantly, this behaviour emerges in the active turbulent bulk regime [37] and in the absence of any confinement or any imposed anchoring boundary conditions. This finding has no parallel in equilibrium systems. This is important since the formation of full-integer topological defects in 2D has until now only been associated with systems with polar symmetry [77–80], confined systems subject to strong anchoring conditions [7, 57, 81, 82] or externally applied stresses [83].

We continue our investigation of the role of the flow-aligning parameter λ from Chapter 4, by exploring the activity ζ and flow-aligning parameter λ phase-space in this chapter. In certain regimes, we find the emergence of stable full-integer defect structures due to two $+1/2$ defects moving towards each other. We show that in addition to activity, active particles' flow-aligning behaviour is the determining factor in this binding of two $+1/2$ defects. We quantify this behaviour and recognise this phenomenon as the director reorienting itself around topological defects due to their self-generated active flows.

5.2 Simulation method

To investigate the formation of full-integer defects, we solve the continuum equations of active nematohydrodynamics (**Eq. 2.21**, **Eq. 2.27** and **Eq. 2.28**). We vary the sign of the activity ζ from extensile ($\zeta > 0$) to contractile ($\zeta < 0$) [21]. While the pivotal role of activity in setting the motion and ordering of self-propelled topological defects has been well established in both models [32, 120, 132, 133] and experiments [28, 58, 70, 84], we illustrated in Chapter 4 that the flow-aligning parameter also has an impact on topological defects' motion. In this chapter, we vary the normalised flow-aligning parameter $|\nu| = \frac{|\lambda|9q}{3q+4}$ (with q denoting the magnitude of nematic order) around the transition point from flow-tumbling to flow-aligning, which occurs at $|\nu| = 1$ (**Eq. 2.23**). For $|\nu| > 1$, which corresponds to the flow-aligning regime, positive values indicate alignment parallel to shear flows, while negative values describe particles that align perpendicular to shear flows. For smaller values, $|\nu| < 1$, the system is in the flow-tumbling regime, and the particles continuously tumble in shear flows.

We set the model parameters to $\Gamma = 0.34$, $\eta = 2/3$, $\mathcal{A} = 0, \mathcal{B} = -0.3, \mathcal{C} = 0.3$ and $K = 0.02$, while varying activity and the flow-aligning parameter. Unless specified, activity is $|\zeta| = 0.25$ and flow-aligning parameter is $|\lambda| = 0.7$ (corresponding to $|\nu| = 1.2$) in our system. Periodic boundary conditions are applied on all sides of the domain, and simulations are initialised with zero velocities and a random director field.

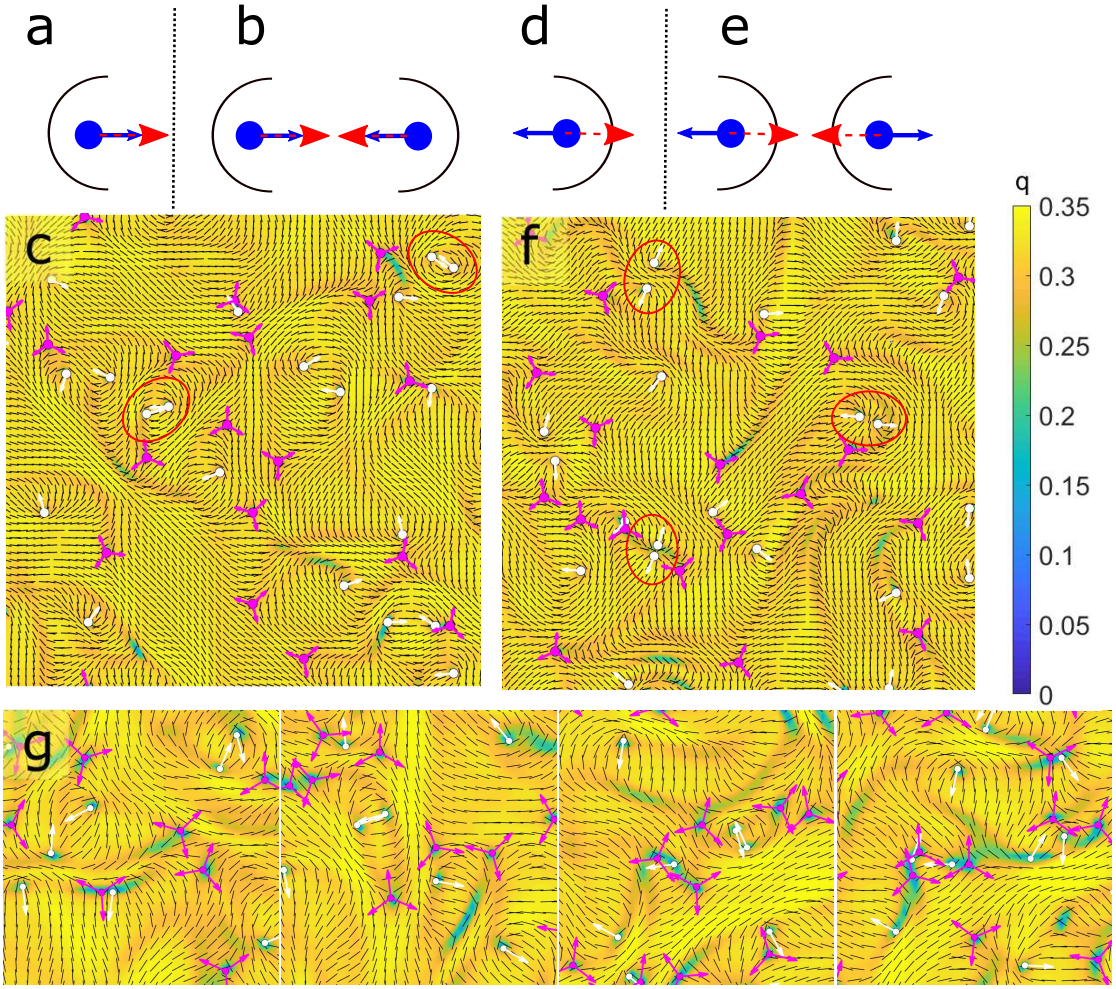

Figure 5.1: Emergence of bound defect pairs. (a,d) Schematic movement of a $+1/2$ topological defect with polar, head-to-tail, axis (where blue arrows denote orientation $\vec{p}$) and a self-propulsion direction (red arrows) for (a) a contractile or (d) an extensile system, respectively. (b,e) Two $+1/2$ defects move toward each other and form a bound $+1$ defect with (b) a vortex-like structure for contractile or (e) an aster-like structure for extensile systems. (c,f) Snapshots of (c) a contractile system with positive flow-aligning parameter $\nu = 1.2$ or (f) an extensile system with negative flow-aligning parameter $\nu = -1.2$. The colourmap illustrates the nematic ordering q and $+1/2$, $-1/2$ defects are highlighted by comets and trefoils, respectively. (g) Snapshots of bound defect dynamics over time.

5.3 Formation of full-integer vortex-like topological defects

First, we consider the case of a positive flow-aligning parameter in the flow-aligning regime with $\lambda = 0.7$ ($\nu = 1.2$). Since most of the numerical studies so far have only focused on extensile activities [13, 24, 53, 56, 120, 132, 134–136], we begin by exploring the effect of contractile activity to shed light on possible new patterns.

At low contractile activities, splay instabilities are followed by unbinding of $\pm 1/2$ defect pairs, and active turbulence is established, a process that is consistent with both previous theoretical predictions [21, 120] and numerical simulations [38, 122]. However, by increasing the contractile activity in this flow-aligning regime, we observe that after $\pm 1/2$ unbinding events, pairs of $+1/2$ defects join together along their comet-shaped tails $\vec{p}$ (**Fig. 5.1**a). The defects form stable structures in the form of vortex-like topological defects (**Fig. 5.1**b,c). Further increase in activity restores unbinding and active turbulence, destroying bound $+1/2$ defect pairs. Intriguingly, we do not observe similar activity-dependent $+1/2$ defect binding for a flow-tumbling regime, indicating that the underlying mechanism of bound $+1/2$ defect formation must be controlled by the flow-aligning behaviour of the director field.

To understand the mechanism of bound $+1/2$ defect pair formation, we consider the response of the director field associated with two interacting $+1/2$ topological defects to their corresponding activity-induced flow fields (**Fig. 5.2**a). To this end, we consider a simplified setup, where only two $+1/2$ defects are near each other in a vortex-like pattern as shown in **Fig. 5.1**a and **Fig. 5.2**; *blue dotted lines*. Using the linearity of Stokes equation, the flow field associated with this configuration is obtained by superposition of the flow fields of each individual $+1/2$ defect that was calculated in **Eq. 2.45** [32]:

$$\vec{v} = \begin{bmatrix} -|\zeta|\left(3(r_2 - r_1) + r_1\cos(2\psi_1) - r_2\cos(2\psi_2)\right) \\ -|\zeta|\left(r_1\sin(2\psi_1) - r_2\sin(2\psi_2)\right) \end{bmatrix}, \tag{5.1}$$

where, $r_{1,2}$ and $\psi_{1,2}$ are the polar coordinates around defect 1 or 2 at the coordinates $(x, 0)$ and $(-x, 0)$ with defect orientation $\psi_1 = \pi$ and $\psi_2 = 0$ (see Appendix C.2 for more details). In the vicinity of the defect core, the total active flow is non-zero (**Fig. 5.1**a; *red streamlines*), and indeed this tends to destroy the vortex-like configurations as $+1/2$ defects rotate and move away from each other in the flow-tumbling regime ($|\nu| < 1$). However, just above the transition to the flow-aligning regime ($|\nu| = 1$), the director field tends to align with a Leslie angle θ_L (**Eq. 2.24**) [104] to the principal axis of flow deformation (**Eq. 2.25**) defined based on the rate of the strain tensor $\boldsymbol{E}$ [52]. As such, calculating the reconfiguration of the

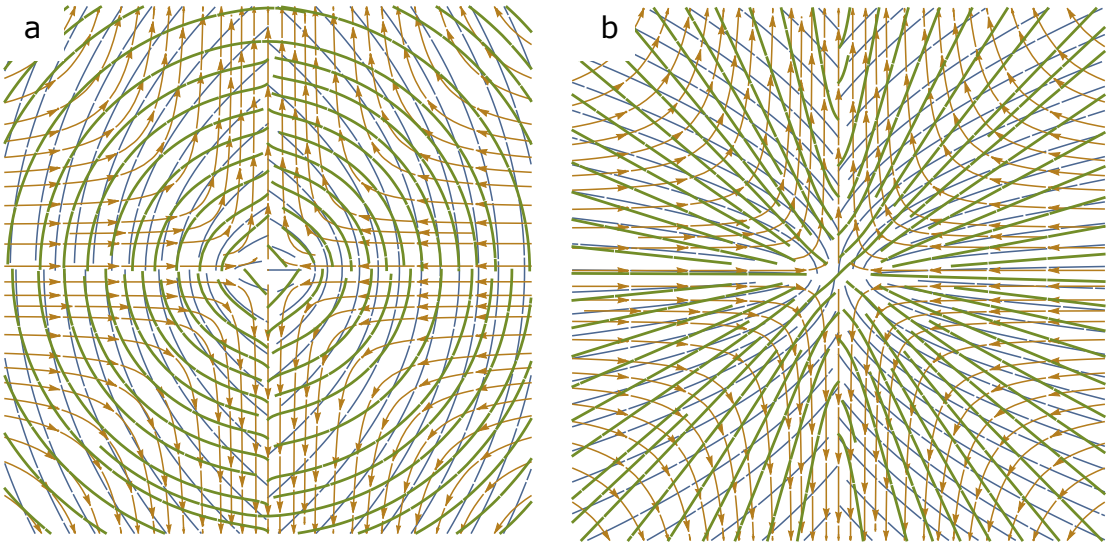

Figure 5.2: Analytical prediction of director reconfiguration in response to active flows of $+1/2$ defect pairs. (a) The contractile vortex-like configuration for $\nu \to 1$. (b) The extensile aster-like configuration for $\nu \to -1$. Blue dotted lines indicate the director field and their associated flow fields are illustrated with the orange streamlines. The green dotted lines indicate the expected reconfiguration of the director field in response to the active flows.

director field in response to the activity-induced flow of the vortex-like structure (see Appendix C.3 for a detailed calculation) shows that as $\nu \to 1$, *i.e.* Leslie angle $\to \pi/4$ to the principal axis of flow deformation, flow gradients result in a preferred reorientation of the director field back into the vortex-like configuration (**Fig. 5.2**a; *green dotted lines).* Thus $+1/2$ defects move closer together due to an effective attractive force from the activity, which eventually is balanced by the elastic force (see Appendix C.4). This indicates a positive feedback between the active flows and the reorientation response of the director field, which can stabilise the vortex structures and explains the formation of stable bound defect pairs.

5.4 Formation of full-integer aster-like topological defects

Interestingly, this mechanism of synergy between active flows and flow-aligning behaviour predicts that in an extensile system, where $+1/2$ defects self-propel along their comet-shaped head (**Fig. 5.1**d), stable bound pairs of $+1/2$ defects can form

when the director tends to align with a Leslie angle to the perpendicular to the principal axis of flow deformations, *i.e.* for a negative flow-aligning parameter ($\nu < 0$). Our calculation of the defect-induced flows and the consecutive reconfiguration of the director field shows that in this case - unlike for contractile case - stable bound defect pairs form when $+1/2$ defects come together head-on, forming aster-like configuration (**Fig. 5.2**b). To test this prediction in our simulations, we consider $\lambda = -0.7$ ($\nu = -1.2$) and increase the extensile activity (**Fig. 5.1**f). At small activities, bend instabilities are followed by $\pm 1/2$ defects unbinding and active turbulence generation. Increasing activities further, we observe the formation of bound $+1/2$ defect pairs in the form of aster-like structures. Further increase in activity breaks down these stable bound defects, and active turbulence is recovered. As in the contractile case, no aster-like configuration is obtained in a flow-tumbling regime. While previous theoretical analyses have predicted the possible existence of such defect configuration due to the active torques acting on $+1/2$ defects [120], our results show the stabilisation as consequence of flow-aligning behaviour of director in response to active flows.

5.5 Quantifying full-integer defects

To more quantitatively characterise the formation of stable bound $+1/2$ defect pairs, we measure the time $+1/2$ defects spend near each other and calculate the density of the bound defect occurrences. If two self-propelled $+1/2$ defects are for a prolonged time ($t > t^*$) next to each other ($r < r^*$) in the configuration as shown in **Fig. 5.1**b,e, they are considered to be bound. Here t^* is a long time ($t^* = 2000$ in simulation units) and $r^* = 10$ is a small distance corresponding to the size of vortex- and aster-like configurations. We introduce this cut-off as even in the active turbulent regime, there is always a finite chance of defects being temporarily near each other due to the chaotic nature of $+1/2$ defect motion.

The results of these measurements are shown in **Fig. 5.3** for varying activities and flow-aligning parameters, and clearly indicate that for defects to bound for long times, the system needs to be active, but that the probability of finding a

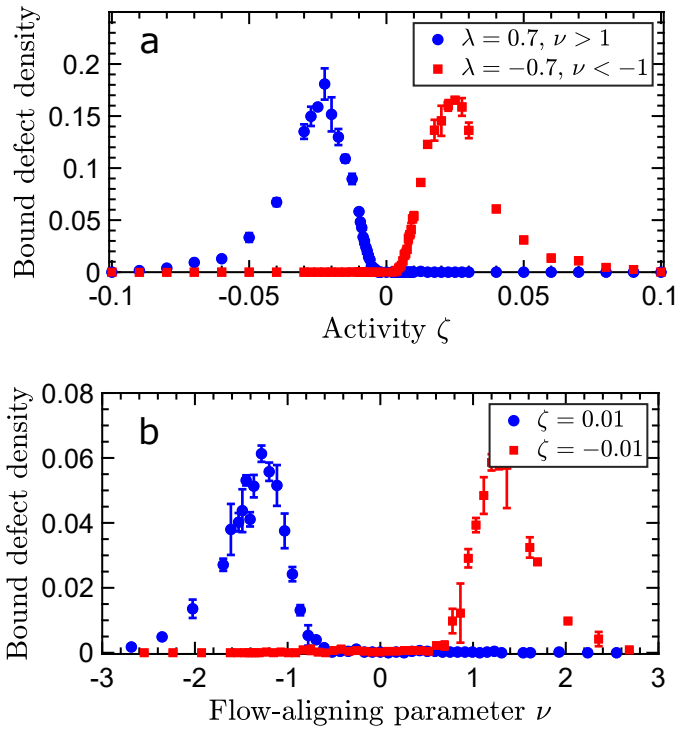

Figure 5.3: Numerical measurements of the bound defect density as a function of (a) activity and (b) flow-aligning parameter.

bound defect pair becomes lower eventually with increasing activity (**Fig. 5.3**a). This suggests that the $+1/2$ defects need their self-propulsion to form stable vortex- and aster-like structures, but that for higher activities, the more chaotic flows make it easier for the bound defects to break apart. This breaking up is caused by approaching $-1/2$ defects as shown in **Fig. 5.1**g.

Secondly, we find that the bound defects appear when the flow-aligning parameter approaches $\nu \to |1|$. Above this value the bound defect density drops again. This is consistent with our analytical prediction that shows that increasing ν above 1, makes the director field align stronger with the principal axis of flow deformation, *i.e.* a smaller Leslie angle, resulting in a deviation from the reconfiguration shown in **Fig. 5.2** (see Appendix C.3 for a detailed calculation). Eventually for large ν, this results in a preferred reconfiguration which renders the bound defect state unstable. This explains why eventually the bound defect density drops by increasing flow-aligning parameter. The results of varying activity and flow-aligning parameters are

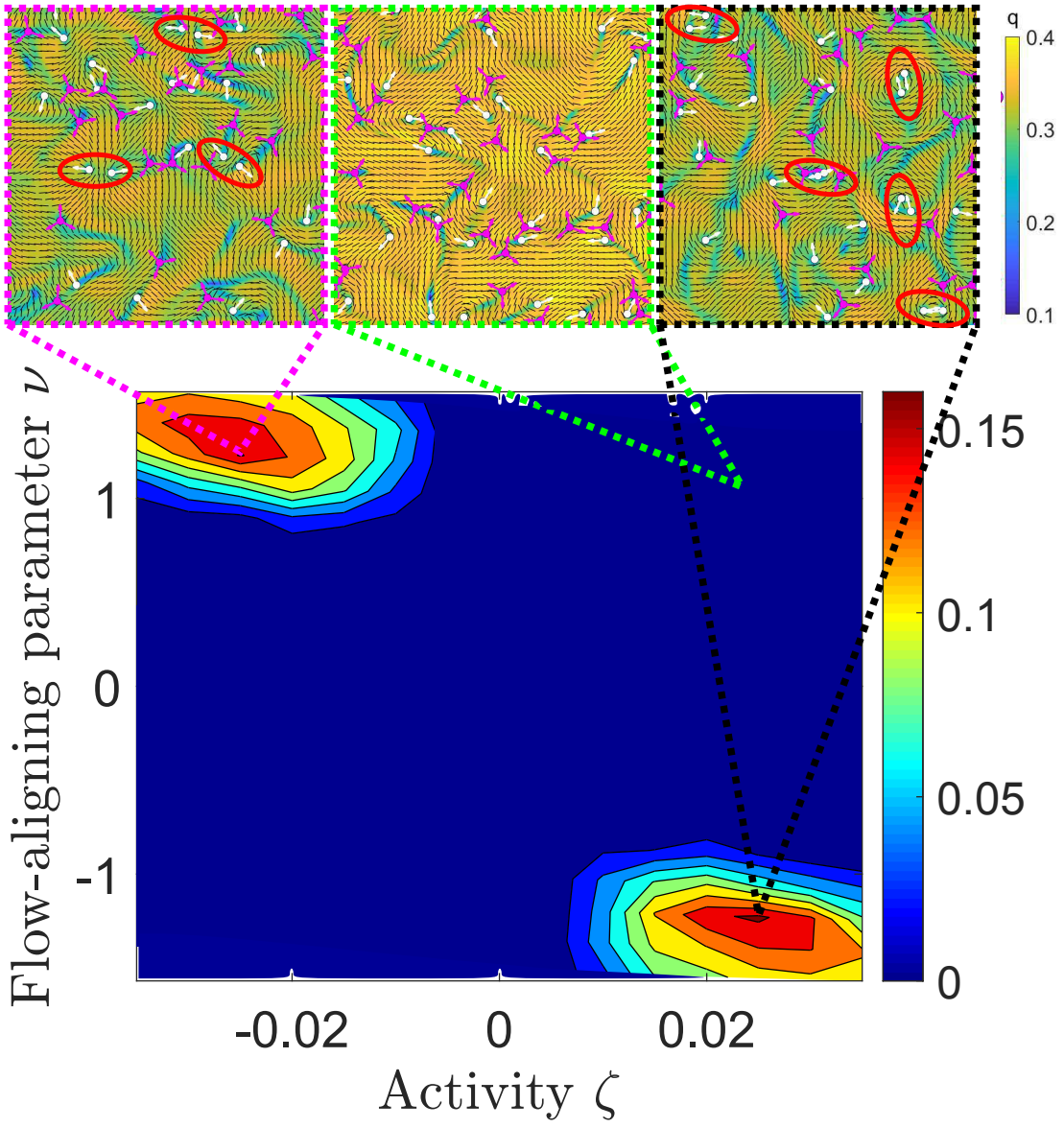

Figure 5.4: Stability diagram of bound defect density. Stability diagram of bound defect density (shown in colourmap) in the activity flow-aligning parameter ($\zeta - \nu$) phase space. The colomap in the inset figures indicates the magnitude of nematic order q.

summarised in the stability diagram (**Fig. 5.4**) showing that similar behaviour of bound defect pair formation is observed for contractile and extensile active nematics in the flow-aligning regime upon changing the sign of the flow-aligning parameter. A further spatio-temporal characterisation of the bound defect lifetime and distance between the defects is provided in **Fig. 5.5**. Measuring the lifetime of two defects near each other shows that this bound defect lifetime has an almost exponential decay (**Fig. 5.5**a,b). When the activity or the flow-aligning parameter is too low, no long-

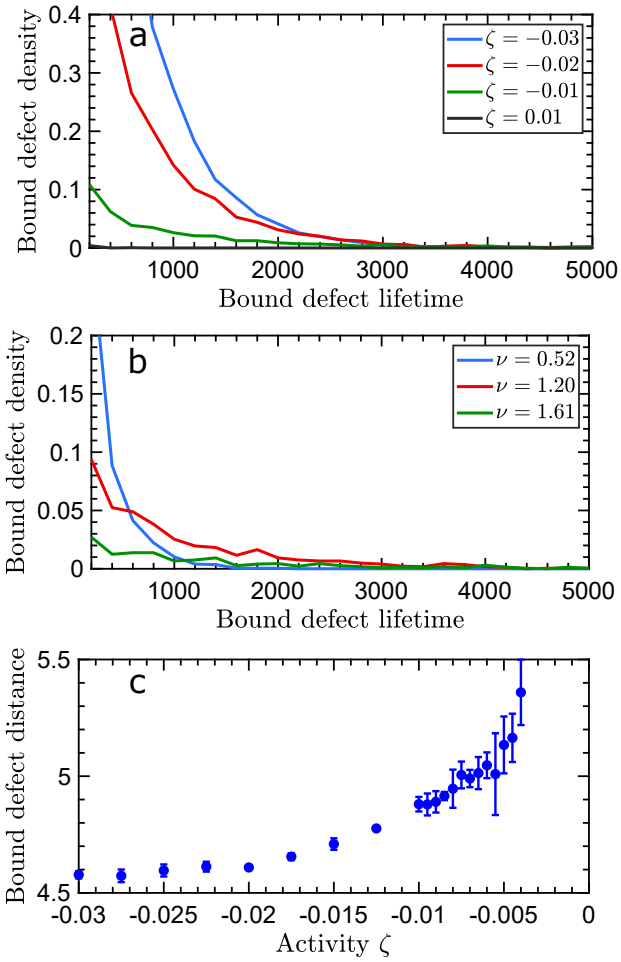

Figure 5.5: Further quantifying bound defect state. Histogram of the bound defect lifetime for (a) different activities when $\nu > 1$ or (b) for different flow-aligning parameters when $\zeta = -0.01$. (c) The average distance between two bound $+1/2$ defects as a function of activity for $\nu > 1$.

lived bound defects are detected. Interestingly, when the flow-aligning parameter becomes too large ν (similar to the activity) the probability of finding a bound defect goes down for any possible lifetime, and the bound defect density starts to decrease.

Moreover, measuring the average distance between bound defects shows that when the activity becomes smaller, the distance between the $+1/2$ defects becomes larger, which suggests that the activity indeed drives the defects close towards each other, which is stabilised with repulsive elastic forces (see Appendix C.4). Increasing the activity results in an eventually plateauing of the distance between $+1/2$ defects due to these repulsive forces (**Fig. 5.5**c).

5.6 Conclusion

The formation of virtual full-integer nematic defects observed here might explain the emerging roles of full-integer defects in biological systems. For example, Maroudas *et al.* [34] show that nematic organisation of actin filaments on the surface of the regenerating animal *Hydra* are important determinants of the shape of the animal. In particular, they show that the full-integer defects demarcate sites of head, foot and tentacles in the animal. Based on the results of our study, we believe that in the regenerating Hydra the full-integer defects are sites where pairs of half-integer defects stabilise into full-integer structures allowing for protrusions to form. In another example, a recent experiment by Meacock *et al.* [29] has revealed that in colonies of fast-moving bacteria, pairs of active $+1/2$ defects are able to come close and orbit each other. The results are reproduced by a discrete model of self-propelled rods interacting via volume exclusion. The experiments show that these sites of stable bound defects are the points where bacteria *escape* into the third dimension. Interestingly, and in-line with our predictions here, it is observed that this phenomenon only happens for fast-moving (larger ζ) and longer (larger flow-aligning parameter ν) bacteria compared to the wild types. These two recent experiments on different biological systems further indicate the potential importance of full-integer defect formation in active systems.

The results presented here demonstrate a new feature of topological defects in monolayers of active nematics. Moreover, identifying the regions of phase-space where $+1/2$ defects can bind to form a $+1$ defect can provide guidelines to design and engineer active nematic systems with more complex topological states.

In addition to the experimental implications, recent theoretical advances have taken steps to construct generic formalisms for multi-defect dynamics in 2D dry active nematics [132, 137] in the limit of compressible and hydrodynamically over-damped systems. Incorporating shear-alignment effects within such a framework and investigating bound defect states would be another interesting step towards constructing generic defect models in active systems.

Reality is merely an illusion, albeit a very persistent one.

Albert Einstein

6 The role of friction in multi-defect ordering

6.1 Introduction

Throughout this thesis, we have considered the experimental system consisting of a dense suspension of microtubules propelled by two-headed kinesin motors (see Chapter 1) [10, 12]. This is a key experimental system to study active nematics as it captures collective dynamics like bulk active turbulence [10, 12], hydrodynamic instabilities and defect proliferation [40]. This experimental system is often prepared such that the microtubules form a film between an aqueous top layer and an oil layer beneath, which in an unconfined system normally results in active turbulence [10]. Interestingly, an investigation of the defect motion in a thin layer of the active material showed that the $+1/2$ topological defects could themselves display long-range nematic ordering while retaining their motile nature [70]. This ordering suggests the possibility for multi-defect interactions that span many defect pairs.

Seveal papers have reported the possibility of defect ordering. Recent simulations of active nematics with hydrodynamics, *wet systems*, have shown that defects exhibit some short-range interactions in active turbulence [13, 84]. Additionally, simulations and analytical approaches to active nematics with strong friction that ignored viscous stress, *dry systems*, showed long-range $+1/2$ defect ordering, but they found polar

rather than nematic orientational order of +1/2 defects [131, 132, 134]. Such polar defect ordering has been attributed to arch-like configurations of the nematic director field [138], which can also exist in wet systems due to memory effects when the system relaxes towards nematic ordering [118]. In another study in the same dry regime where arch-like configurations emerge and where rotational contributions to the flow are ignored, a static lattice of defects with positional and orientational order was observed [129]. A static lattice was also found in the high friction regime in the presence of viscous stress [47].

To clarify how defects order in wet active nematics, we perform large scale continuum simulations to measure both the positional and the orientational order of topological defects with varying friction (**Fig. 6.1**). We confirm that +1/2 defects prefer to position themselves side by side and align anti-parallel [13, 84], while the −1/2 defects prefer to impose a three-fold symmetry on their surroundings. Increasing friction decreases the hydrodynamic screening length, which measures the competition between viscocity and friction, and increases the effectiveness of the defect-defect interactions. The defects start to form dynamically evolving orientationally and positionally ordered structures even in the regime where defects are still motile. The emerging structures can be explained in term of the competition between hexagonal packing preferred by the −1/2 defects and rectangular packing preferred by the +1/2 defects. The range of the ordering increases with increasing friction in agreement with experiments [70].

6.2 Simulation method

To investigate the orientational arrangements of defects, we solve the continuum equations of active nematohydrodynamics (**Eq. 2.21**, **Eq. 2.27** and **Eq. 2.28**). In this chapter, we use the parameter range $\Gamma = 0.34$, $K = 0.01$, $\eta = 2/3$, $\rho = 1$, $\lambda = 0.7$ and $\zeta = 0.02$. We set the Landau-de Gennes parameters to $\mathcal{A} = 0.01, \mathcal{B} = 0$ and $\mathcal{C} = 1.3$, so that without active shear flows the isotropic state emerges and we get no memory effects in the nematic orientation as the tensor order parameter $\boldsymbol{Q}$ relaxes towards the isotropic state [118]. We also include a friction tensor $\boldsymbol{f}$ in the

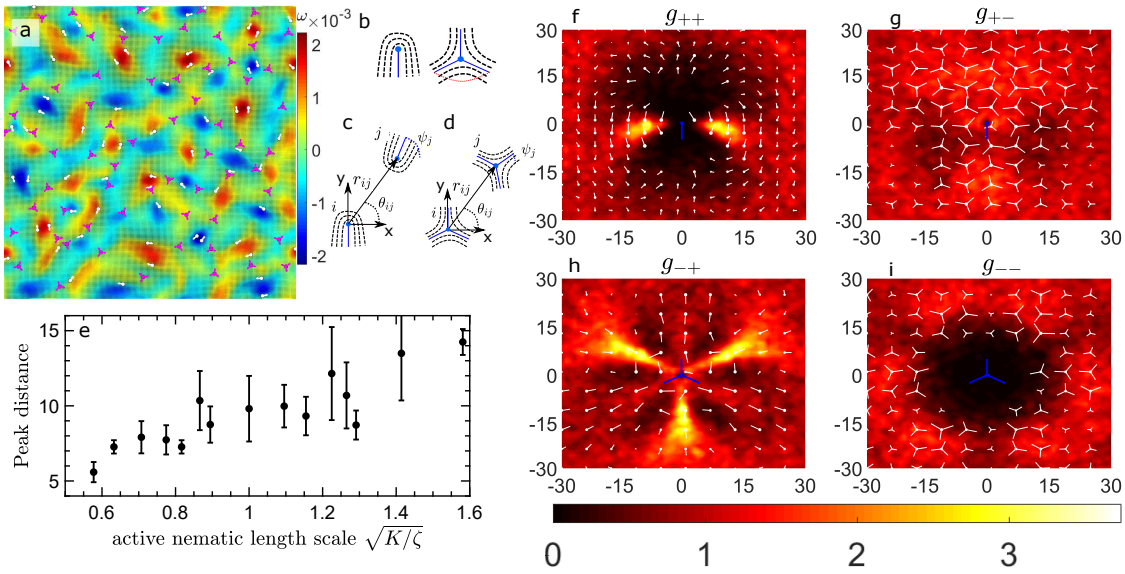

Figure 6.1: Defect ordering in wet active turbulence. (a) Snapshot of active turbulence for very low friction, $F = \sqrt{(K/\zeta)(f/\eta)} = 0.023$. The white (magenta) symbols are $+1/2$ ($-1/2$) defects. Background colour denotes the vorticity. (b) Schematic representation of $+1/2$ and $-1/2$ defects. $+1/2$ defects have a single polar axis $\vec{p}$ (blue line) and $-1/2$ defects have three axes $\vec{p}$. (c,d) For a reference (c) $+1/2$ or (d) $-1/2$ defect i we define an associated polar coordinate system. (e) Spacing between $+1/2$ defects (defined as the position of the maximum in g_{++} (in lattice units) as a function of the active length scale $\sqrt{K/\zeta}$. Activity ζ and elasticity K were varied. (f-i) Pair distribution function $g_{ab}(r, \varphi)$ where a and b represent $+$ and/or $-$ half-integer defects showing the positional distribution of b-type defects around an a-type defect. The white arrows represent the orientational distribution vector $\vec{S}$ with arrow size normalised by the magnitude of $\vec{S}$ and axes are in lattice units.

Navier-Stokes equation (**Eq. 2.28**), thus modelling energy loss from the 2D active film to its surroundings. The two diagonal coefficients of the friction tensor are identical f (isotropic damping), which we vary in the range $f = 0.0007$ to $f = 0.014$.

6.3 Defect distributions

To measure positional and orientational correlations between defects, we treat the $+1/2$ and $-1/2$ defects as two different types of quasi-particle with different symmetries (**Fig. 6.1**b) [139]. Defects are found by measuring the local winding number or the charge (see Appendix B.1) [124, 127] while the defect orientation $\vec{p}$ is measured with **Eq. 2.18**. We consider a reference defect i and choose a coordinate system with the reference defect as the origin and the Cartesian axes oriented

relative to the defect orientation $\vec{p}$ as shown in **Fig. 6.1**c,d. To define the relative position of the second defect, we use polar coordinates (r, φ) defining φ as the angle from the x-axis in this reference frame. We measure the relative position of the other defects j present at a given time step (**Fig. 6.1**c,d), and then sum over all the measured defect pairs, taking data every 1000 time steps to get the pair-wise positional distribution function:

$$g_{\pm\pm}(r, \varphi) = \frac{V}{N_{\pm\pm}} \sum_t \sum_{\pm\pm\text{pairs}} \delta(r - r_{ij}, \varphi - \varphi_{ij}), \tag{6.1}$$

where the subscripts of g indicate the type of the defect pair ij, e.g. $-+$ refers to the positioning of $+1/2$ defects around a $-1/2$ defect. The normalisation $V/N_{\pm\pm}$ is the area divided by the total number of defect pairs $N_{\pm\pm}$. We introduce this normalisation to set $g = 1$ at $r \to \infty$ to normalise to bulk densities at large distances. To acquire sufficient statistics each distribution function is based on measurements of at least 10^6 defect pairs which requires runs ~ 3 orders of magnitude longer than the average defect lifetime (see Appendix C.5 for an estimate of the errors in the measurements).

In addition to the relative defect positions, we are also interested in the average defect orientation relative to the reference defect. To obtain this information, we calculate the orientation distribution vector,

$$\vec{S}_{\pm\pm}(r, \varphi) = \mathcal{N}_{\pm\pm} \sum_t \sum_{\pm\pm\text{pairs}} \delta(r - r_{ij}, \varphi - \varphi_{ij}) \begin{bmatrix} \cos \mathcal{M}_j \psi_j \\ \sin \mathcal{M}_j \psi_j \end{bmatrix}, \tag{6.2}$$

where ψ_j is the polar angle of the orientation of defect j in the coordinate frame defined by the reference defect i (**Fig. 6.1**c) (**Eq. 2.18**). Here $\mathcal{M}_j = 2(1 - m_j)$, where m_j is the charge of the jth defect, accounts for the three-fold rotational symmetry of the $-1/2$ defects. Taking the normalisation constant as $\mathcal{N}_{\pm\pm} = V/(N_{\pm\pm} g_{\pm\pm}(r, \varphi))$ means that the magnitude of $\vec{S}$ is 0 in the absence of orientational correlations and 1 if the defect orientations are perfectly correlated. To avoid statistically insignificant data, we set $g = 0$ and $\vec{S} = 0$ if the defect count for any lattice site is lower then 5.

6.4 Emergent defect ordering at low friction

We first consider very low friction and high activity, recovering well-developed wet active turbulence (**Fig. 6.1**a). **Fig. 6.1**f shows how positive defects behave in the vicinity of another positive defect: even in this highly turbulent regime there is a clear preference for neighbouring $+1/2$ defects to line up along the x-axis in an anti-parallel configuration with a preferred distance between neighbours. This preferred defect spacing scales with the active nematic length scale, $l_\zeta \sim \sqrt{K/\zeta}$ (**Fig. 6.1**e). Therefore we choose to measure the friction in terms of a dimensionless friction number $F = \sqrt{(K/\zeta)(f/\eta)}$ which is the ratio of the active length scale to the hydrodynamic screening length.

Fig. 6.1i shows that $-1/2$ defects prefer not to lie too close to each other, and that there is no preferred length scale in contrast to the $+1/2$ defects. Interestingly, the $-1/2$ defects do impose an orientational structure on surrounding $-1/2$ defects even in this fully active turbulent regime. We already find six peaks where the neighbouring defects have a strong preference for anti-parallel alignment. This is due to the elastic torque [140]. However, the symmetry of the peak positions is caused by the flow fields, which form six vortices around negative defects (**Fig. 2.6**b). Finally, **Fig. 6.1**g,h show that positive and negative defects are preferentially found close together and aligned in the relative orientation associated with creation and annihilation events.

6.5 Defect lattices at high friction

As the friction is increased to $F \sim 0.08$, the defect interactions result in large-scale ordering of the defects. As an example, **Fig. 6.2**a presents a snapshot of the defect structure and corresponding vorticity field for $F = 0.083$, where the mean speed of the flow has been reduced by an order of magnitude with respect to the no friction regime. This figure shows that $+1/2$ defects have a strong tendency to form anti-parallel pairs, which induce and orbit on vortices, as already apparent in the no friction limit. But much larger-scale defect arrangements also become

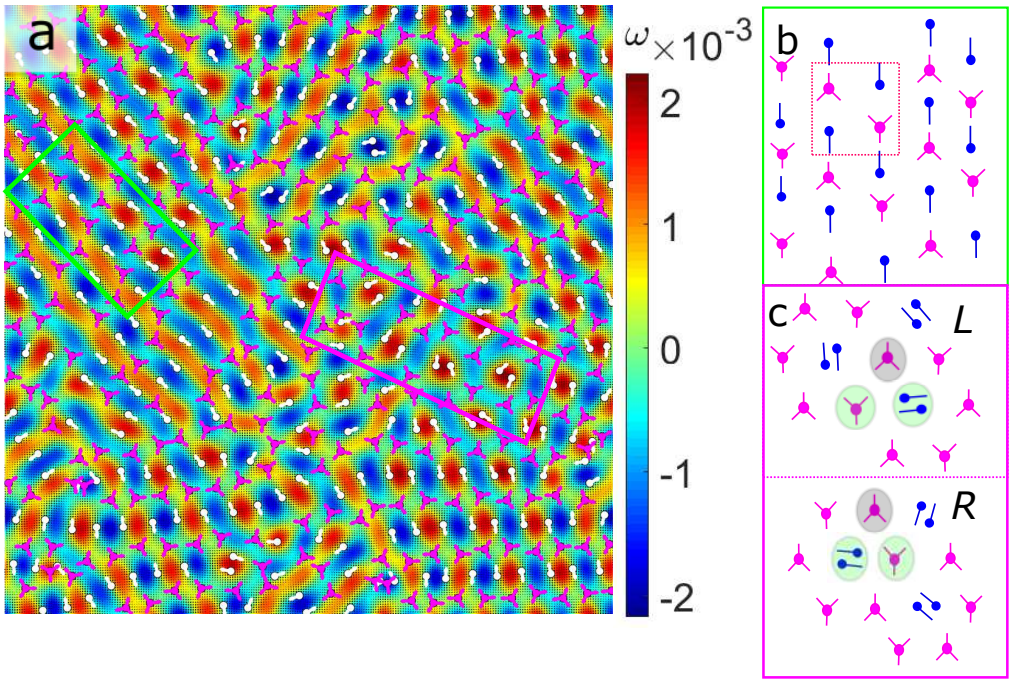

Figure 6.2: Defect structures at intermediate friction. (a) Snapshot of the defect structures at intermediate friction $F = 0.083$. $+1/2$ ($-1/2$) defects are shown in white (magenta). There is transient local defect ordering into a rectangular (green outline) or a hexagonal (magenta outline) pattern. The background colour represents the vorticity field. (b) Schematic of the rectangular ordering. (c) Schematic of the hexagonal ordering, which is chiral: $-1/2$ defects (in grey) have either a left or right neighbouring $-1/2$ defect (in green). The other position is filled by rotating $+1/2$ defects resulting in local zero defect charge (also in green).

apparent at high friction, as not only the interactions between the $+1/2$ defects but also those between the $-1/2$ defects result in significant ordering. To investigate this, we first consider the structure formed by the $+1/2$ defects (**Fig. 6.2**b), and then the ordering preferred by the $-1/2$ defects (**Fig. 6.2**c).

Fig. 6.3a,b show distribution functions of $\pm 1/2$ defects around a $+1/2$ defect at strong friction ($F = 0.103$). The first obvious feature of these correlations is that the anti-parallel ordering of the $+1/2$ defects along x is more pronounced and longer ranged than in the frictionless limit. This is confirmed by **Fig. 6.3**c where we plot the pair-wise positional distribution function $g_{++}(r, 0)$ showing how the strength and range of the correlations increase with increasing friction.

Fig. 6.3d shows that $+1/2$ defects are also ordered along the y-axis. This ordering can be interpreted by comparing the distribution functions in **Fig. 6.3**a,b

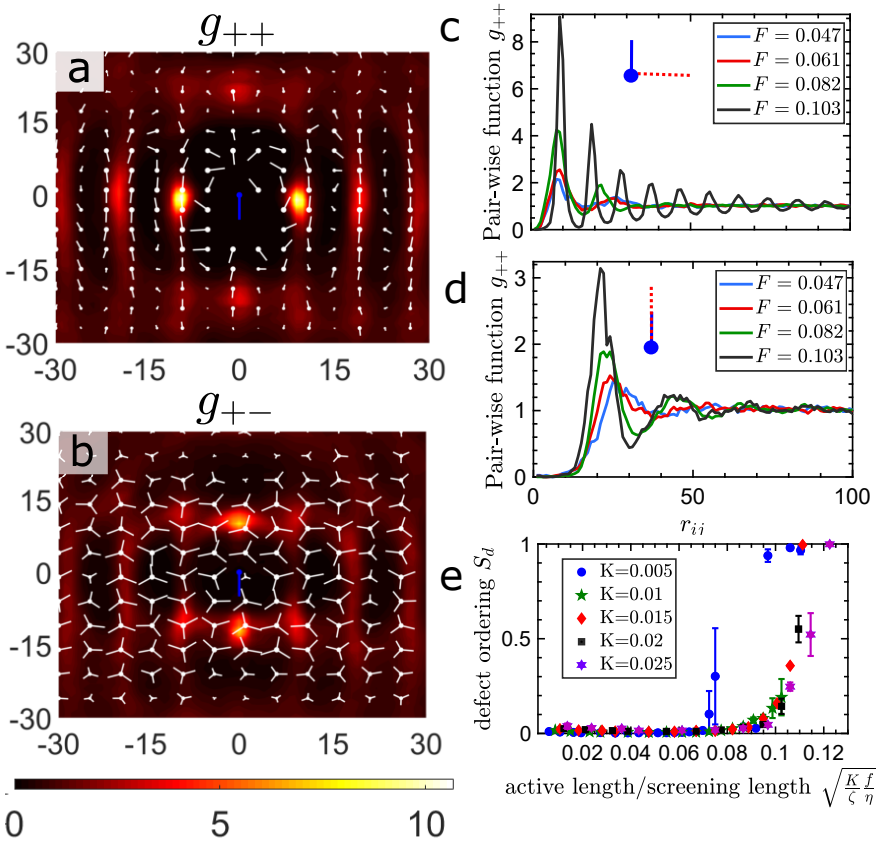

Figure 6.3: Ordering around a $+1/2$ defect at high friction. (a,b) Pair distribution function $g_{++}(r,\varphi)$ and $g_{+-}(r,\varphi)$ (colourmap) and the corresponding orientation distribution vector $\vec{S}_{\pm\pm}$ (white arrows) for high friction $F = 0.103$. Axes are in lattice units. (c,d) $g_{++}(r,0)$ and $g_{++}(r,\pi/2)$ showing the build-up of order along the x- and y-axes (in the direction of the red dotted line) with increasing friction. (e) Nematic defect ordering S_d, as a function of dimensionless friction $F = \sqrt{\frac{K}{\zeta}\frac{f}{\eta}}$, for varying elastic constant K.

which show that $+1/2$ and $-1/2$ defects alternate along the y-axis, and that they align parallel. The ordering increases with friction, but is less pronounced than that along x. This configuration is favoured because it leads to non-conflicted flows. We note that this result relies on the presence of intervening $-1/2$ defects, and is different from the active torque between two $+1/2$ defects studied in [120]. Together, the preferred ordering of $+1/2$ defects along x and y, *i.e.* perpendicular and parallel to the polar axis of the defects $\vec{p}$, is satisfied by the rectangular packing of defects shown in **Fig. 6.2**b.

In **Fig. 6.3**e we plot the nematic order parameter $S_d = -1 + 2\sum_t \sum_{++pairs}(\vec{p}_i \cdot \vec{p}_j)^2/N_{++}$ as the friction and elastic constants are varied. The data collapse confirms

F as a suitable control parameter for the simulations. We find that S_d takes a non-zero value, even when the defects are still motile, and increases with increasing friction. It is reminiscent of the experimental system of microtubules driven by motor proteins where the nematic order of defects increased with decreasing film thickness [70]. However, the patterning also exhibits higher-order symmetry than just nematic as the ordering of defects is polar or anti-polar depending on their relative positions. Upon increasing the friction further ($F = 0.106$ in **Fig. 6.3**e), the defects stop moving and a vortex lattice with orientational defect order is established [47] on scales comparable to the system size, which is ~ 15 times the active length scale. To check whether this is a true transition, we ran simulations on larger systems which showed that the ordering decreases with increasing system size (reported in Appendix C.6). Thus, at these values of F, we observe coexisting domains with long- but not infinite-range order. At yet higher frictions the dynamics becomes too slow to allow feasible simulations of the defect lattices and, for $F \gtrsim 0.14$, the activity is too weak to create defects.

Fig. 6.4 presents results for the ordering around negative defects showing a distinct difference between intermediate ($F = 0.082$, **Fig. 6.4**a,d) and high friction ($F = 0.103$, **Fig. 6.4**b,e). In the intermediate friction regime there are six first neighbour and six second neighbour peaks in the positional distribution function around the central defect, corresponding to a hexagonal packing of $-1/2$ defects. Both right-handed and left-handed lattices are possible (**Fig. 6.2**c). With increasing friction, however, the nearest neighbour peaks become less pronounced showing that it is increasingly difficult to form a hexagonal lattice.

Instead the secondary peaks become more pronounced. The reason for this is apparent from **Fig. 6.4**c,f, which show that the $+1/2$ defects increasingly line up along the polar arms of the $-1/2$ defects, and lie between two $-1/2$ defects [84, 120]. It corresponds to the polar ordering of alternate $+1/2$ and $-1/2$ defects seen in the rectangular lattice (**Fig. 6.2**b).

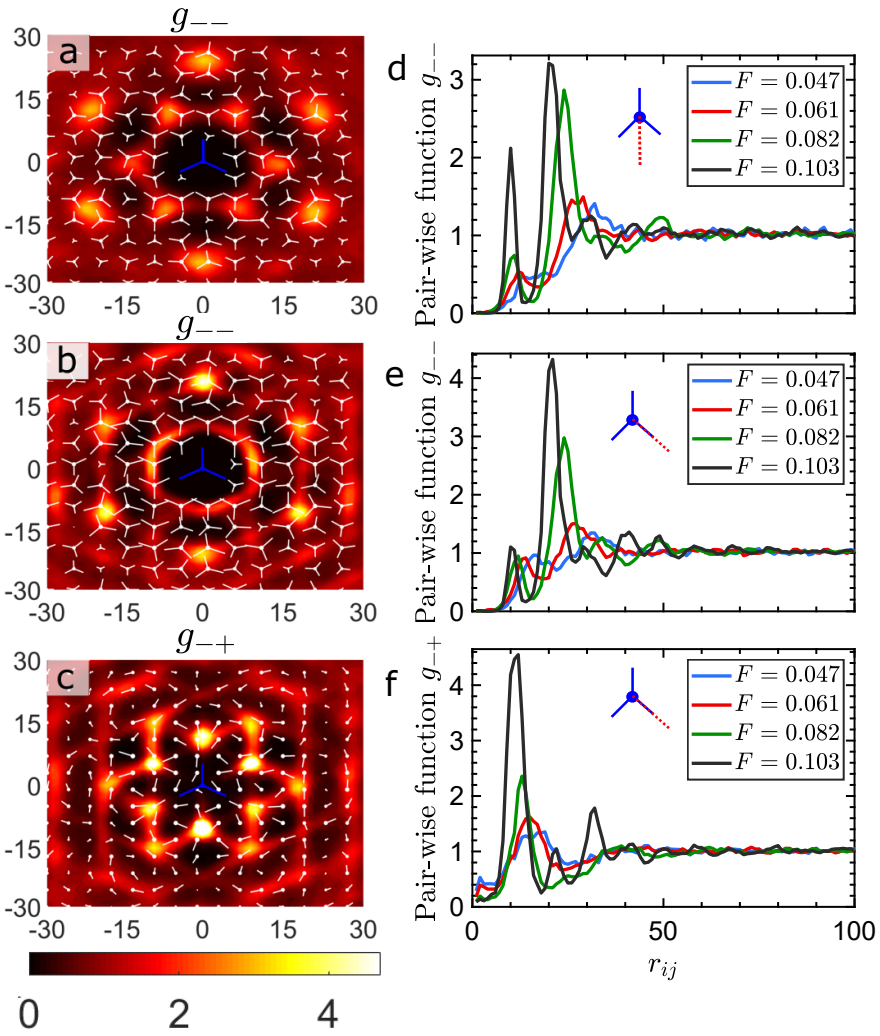

Figure 6.4: Ordering around a $-1/2$ defect at high friction. (a) Pair distribution function $g_{--}(r, \varphi)$ (colourmap) and the corresponding orientation distribution vector $\vec{S}_{\pm\pm}$ (white arrows) for intermediate friction $F = 0.083$. Axes are in lattice units. (b,c) Pair distribution functions $g_{--}(r, \varphi)$ and $g_{-+}(r, \varphi)$ for high friction $F = 0.103$. (d-f) $g_{--}(r, -\pi/2)$, $g_{--}(r, -\pi/6)$ and $g_{-+}(r, -\pi/6)$ (along the red dotted line) with increasing friction.

6.6 Conclusion

We have numerically investigated defect ordering in an active nematic with hydrodynamic interactions and increasing friction. We show that friction can introduce nematic ordering of defects on length scales many times larger then the active length scale, as observed in experimental systems [70]. A local measurement would, however, give polar order of $+1/2$ defects in the direction of their polar axis (mediated by intervening $-1/2$ defects), and anti-polar order of the $+1/2$

defects perpendicular to this axis.

Weak signatures of this ordering are observed even in fully developed active turbulence with no friction. Upon increasing the friction, we observe structures with longer-ranged ordering. The $-1/2$ defects tend to reorganize themselves into hexagons, where each hexagon encompasses two $+1/2$ defects which rotate on a vortex. However, this is not an ideal configuration for pairs of oppositely charged defects and, as a consequence, the hexagonal packing of defects coexists with the rectangular structure shown in **Fig. 6.2**b. As the friction is increased, and the hydrodynamic screening length becomes comparable to the active length scale, the rectangular packing becomes dominant, and the system eventually freezes into the rectangular lattice [47, 129]. The work in this chapter illustrates that defects in active nematics may exhibit complex multi-defect dynamics, which was recently described using a generic formalism in dry systems. In some parameter regimes, that theory captured the behaviour reported in this chapter [137].

What is consciousness? Our brain simulates reality. So, our everyday experiences are a form of dreaming, which is to say, they are mental models, simulations, not the things they appear to be.

Stephen Laberge

7

Submersed micropatterned structures control active nematic flow, topology and concentration

7.1 Introduction

We have demonstrated control of collective flows and topological discontinuities in active nematics by introducing confining walls (Chapter 3), and anisotropic and uniform isotropic substrates (Chapters 4 and 6). In addition to commanding the flow and defect dynamics, the possible control of active materials' concentration is also a topic of ongoing investigations. This has been studied from the perspective of coexistence of dilute and dense phases of self-propelled rods [141–146]. In addition, controlled accumulation and depletion of active material has been engineered in biophysical systems such as funnel ratchets, which have been employed to concentrate cells [147–149] or drive bacterial-ratchet motors [150–152]. Similarly, substrate gradients have been shown to modify cellular motility leading to density variations [153–156].

In this chapter, we report a method for controlling the topological defect population, collective flow and concentration of active nematics by introducing position-dependent friction in a two-dimensional active nematic film. Our simulations are

accompanied by experiments consisting of microtubule-kinesin motor films between aqueous and oil layers [10], as outlined in Chapter 1. In the experiments, the oil layer's depth beneath the superjacent active film is varied to adjust dissipation at different positions by implementing submersed underlying substrate geometries. This tunes the effective friction at different positions in the film. The change in friction results in effective virtual boundaries within the active film, which can control active nematics' collective dynamics. In this chapter, we will introduce three submersed structures: micropatterned trenches (**Fig. 7.1**a-c), stairways (**Fig. 7.1**d-f), and pillars (**Fig. 7.1**g-i). We demonstrate that we can control the flow and orientation of active nematics with the trench structure. In addition, we can modify the defect density in active turbulence with the friction stairway. Lastly, the small virtual enclosure allows us to induce depletion of active material above the pillar.

The experiments presented here pertaining to the submersed trenches and pillars were performed by Dimitrius Khaladj and Professor Linda Hirst of UC Merced. The submersed stairway experiments were performed by Professor Mohamed Amine Gharbi and Professor Seth Fraden, who are affiliated with the University of Massachusetts Boston and Brandeis University, respectively.

7.2 Simulation method

We solve the nematohydrodynamic equations (**Eq. 2.21**, **Eq. 2.27** and **Eq. 2.28**) that evolve the density ρ, the velocity $\vec{u}$ and the tensor order parameter $\boldsymbol{Q}$. Following the conclusion of Chapter 4, the flow-aligning parameter λ is taken to be in the flow-aligning range and set to $\lambda = 0.5$. We take $\epsilon = 2.55$ and $\mathcal{A}_0 = 0.05$ in **Eq. 2.7**. The choice of free energy parameters allows nematic ordering only due to activity-induced flows, in agreement with previous experiments [10]. Other parameters are also set to values that capture microtubule-kinesin mixture dynamics ($\Gamma = 0.5$, $K = 0.02$ and $\eta = 2/3$) [56]. We supplement the continuum equations with **Eq. 2.30** to allow for varying concentrations of active material, which we describe with a phase-field $\phi(\vec{r})$ varying from 0 (low concentrations) to 1 (high concentrations). As we vary ϕ, we retain the ϕ dependence of the active stress (**Eq. 2.35**) with

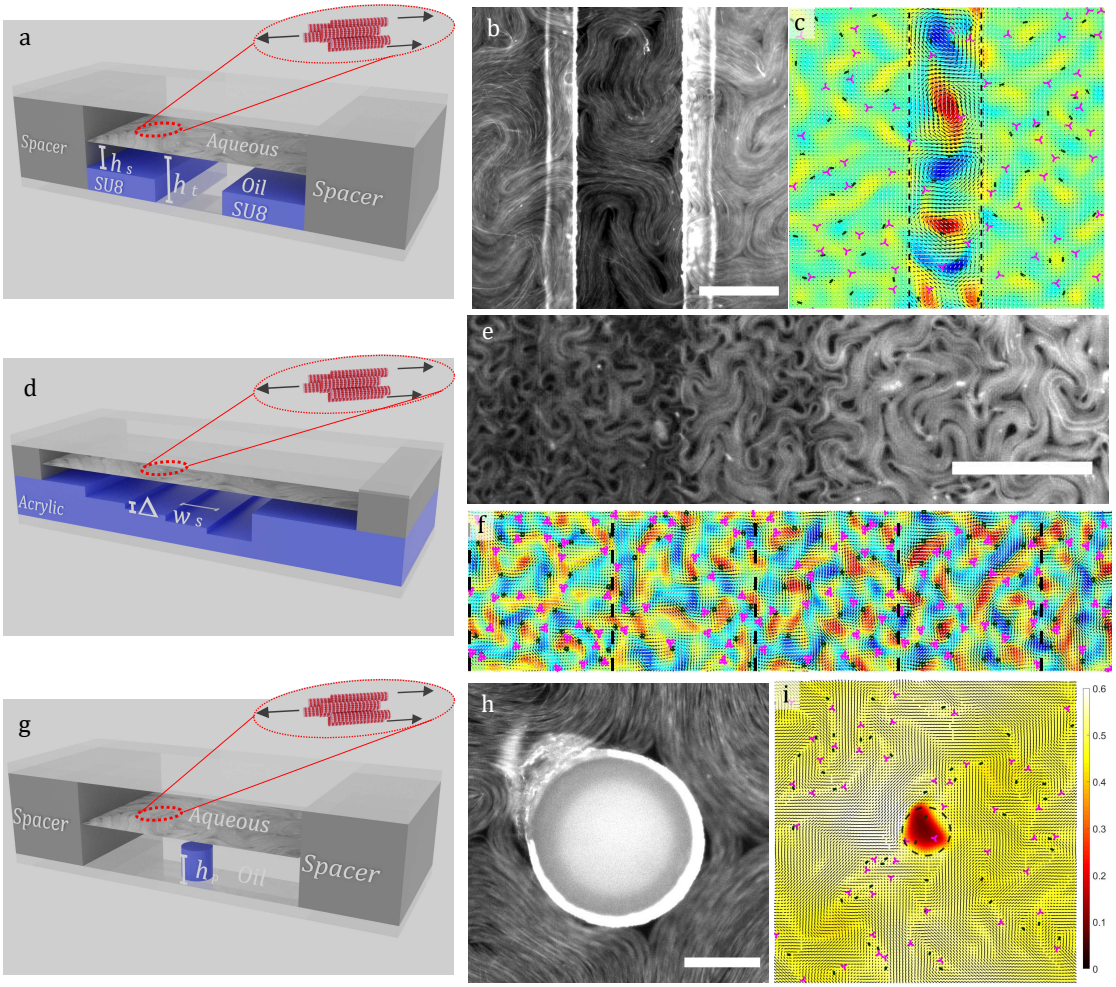

Figure 7.1: Submersed micropatterns control active nematic dynamics. (a-c) **Trench set-up.** An active film resides at the oil-water interface above different substrate depths. The active flows drag the underlying oil layer, but viscous dissipation is depth-dependent, affecting active nematic film dynamics. (b) Fluorescent image of the submersed trench and the superjacent bundled-microtubule active nematic. Scale bar is 250µm. (c) Simulation results for the vorticity field ω (curl of flow) within the superjacent active nematic layer. Distinct flow behaviours are found within the low friction region (between the dashed lines) and high friction (beyond the dashed lines). $+1/2$ $(-1/2)$ defects, denoted by dark green (magenta) symbols, behave markedly different in different regions. (d-f) **Stairway set-up.** (e) Fluorescent image of micromilled stairway and the superjacent bundled-microtubule active nematic. Scale bar is 250µm. (f) Simulation results for discrete steps in the effective friction (dashed lines). The difference in oil depth alters the length scale of the active turbulence above each step. Step location indicated by dashed lines. (g-i) **Pillar set-up.** (h) Fluorescent image of the bundled-microtubule film above the SU-8 micropillar. Scale bar is 100µm. (i) Simulations results show the active nematic concentration ϕ (denoted with the colourmap) is depleted within the high friction region encircled by the pillar perimeter (dashed line).

activity $\zeta = 0.09$, and we initialise our simulations with $\phi = 0.5$ everywhere. Hence, the magnitude of the active stress ($\phi\zeta$) is similar to previous chapters. The additional parameters in **Eq. 2.30** are $\Gamma_\phi = 0.1$, $\mathcal{A}_\phi = 0.03$ and $K_\phi = 0.1$. The $\Gamma_\phi = 0.1$ is taken low compared to Γ as concentration changes are advection dominated. Active shear flows suppress mixing so that ϕ does not phase separate into high and low ϕ regions for sufficiently high active shear flows. Lastly, we define a characteristic boundary scale as $R = 20$ lattice Boltzmann (LB) nodes and normalise all length scales with R in this chapter.

7.3 Submersed trench

Experiments are performed in the trench geometry (**Fig. 7.1**a) to investigate how structures fully submersed in a layer of oil influence defect and flow dynamics in the superjacent active film. The micropatterned trench has a depth of $\Delta_t = 18 \pm 1\mu$m and width $w_t = 327 \pm 2\mu$m (**Fig. 7.1**a). **Fig. 7.1**b,c show that flows in the active nematic layer exhibit coexistence of two distinct regions: orderly collective flows directly above the trench and active turbulence in the shallows surrounding the deep trench. These regions are separated by well-defined virtual boundary lines located directly above the trench edges. Beyond the trench borders, the active nematic retains the chaotic nature of active turbulence. However, directly above the trench, the width establishes a local confining length scale within the superjacent active nematic sheet. The virtual walls at the trench edges trap defects in the trench region and produce active flow behaviours similar to those observed in confining channels [53, 56, 58, 136]. This illustrates how virtual boundaries such as these, can be used to define areas of orderly flows and areas of active turbulence, all without penetrating the active nematic film.

Fig. 7.2a displays the $+1/2$ and $-1/2$ topological defect distributions across the trench, demonstrating that $-1/2$ defects tend to be located in the vicinity of the virtual boundaries. Experimental observations of $-1/2$ defect motion close to the trench edge reveal that these defects tend to reside there with reduced velocity over long intervals, contributing to high-frequency peaks in defect distribution.

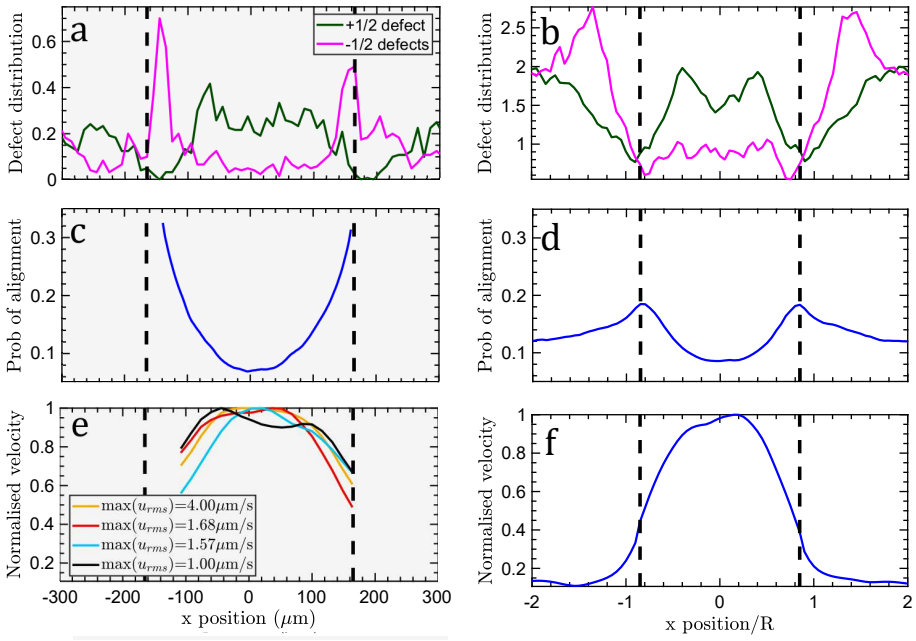

Figure 7.2: Positive defects depleted at the trench interface. The interfaces are indicated by the dashed lines. Panels with grey backgrounds denote experimental results, while white backgrounds denote numerical results. (a,b) Distribution of $\pm 1/2$ defects as a function of transverse position x measured from experiments and simulations, respectively. (c,d) The probability profile that the nematic director is oriented less than 10° from the direction parallel to the trench wall as a function of x. The director field has a high probability of alignment with the virtual boundaries. (e,f) The normalised root mean square fluid velocity profile across the trench.

On the other hand, $+1/2$ defects tend to be depleted from the vicinity of the trench boundaries. Plus-half defects confined within the trench region move along oscillatory trajectories that do not approach the boundaries in general. In the exterior region far from the virtual trench, the defect density profile approaches a homogeneous distribution.

We explain the virtual boundary mechanism as arising from abrupt steps in fluid depth h between the film and the underlying substrate. The trench depth increases from h_s in the surrounding shallows down to a trench depth $h_t = h_s + \Delta_t$ (**Fig. 7.1**a). As activity drives flows within the nematic film, the underlying thin oil-layer viscously dissipates momentum due to the subjacent no-slip substrate, which can be described as a local effective friction acting on each point within the superjacent active film [157]. Following from the lubrication limit, the effective friction coefficient scales as $f \sim \eta'/h\,(\vec{r})$, where η' is an effective viscosity of the

surrounding fluid. The abrupt height change across the trench boundaries results in sharp virtual boundaries in the active nematic film [157].

In our simulations, we replicate the observed experimental phenomena with 2D active nematohydrodynamic simulations, in which the submersed micropatterning is incorporated via an effective isotropic friction field $\boldsymbol{f}(\vec{r}) \cdot \vec{u}(\vec{r})$ in the momentum equation (**Eq. 2.28**). Similar to Chapter 6, the two diagonal components of the friction tensor are identical, but they are now position-dependent, $f(\vec{r})$. Since previous studies have successfully modelled the collective dynamics of microtubule-kinesin-based active nematic films with weak friction [158], we treat the friction as negligible in the active film above the deep regions. We include lubrication momentum dissipation in the regions above shallows via a non-zero effective friction coefficient f, which we set to $f = 0.07$. The trenches are simulated in $(7.5 \times 30)R$ periodic systems with a deep trench (no friction) region of width $1.7R$.

The numerical results show that steps in effective friction can introduce virtual boundaries in the active nematic layer. This is similar to recent work where defects interact with virtual boundaries due to position-dependent activity ζ [159]. The $+1/2$ defects are repelled from the friction interface, and the $-1/2$ defects tend to be positioned at the boundaries with reduced velocities compared to distant positively charged defects (**Fig. 7.2**b). The agreement between our simulations and experiments shows that the micropatterned structures create virtual planar boundaries in the film. The existence of peaks in the $-1/2$ defect density at the virtual boundaries (**Fig. 7.2**a) is consistent with previous work [58] in which it was shown that an interface could act as a catalyst for the creation and subsequent unbinding of defect pairs. While newly created $+1/2$ defects move away due to their self-propelled motility, the $-1/2$ defects remain near the interface.

Fig. 7.2c shows the time-averaged director orientation across the trench and plots the probability that the nematic director is oriented between $80 - 100°$ relative to the normal of the virtual boundaries. This reveals that the virtual boundaries introduce an effective planar anchoring of the director field, similar to real boundaries [58]. The active nematic model captures this behaviour for the virtual boundaries

and reveals that the probability declines to a uniform distribution far from the trench (**Fig. 7.2**d). The experiments exhibit stronger planar anchoring at the virtual boundaries than the simulations, which is likely related to the assumption of an active, continuous fluid in the simulations compared to finite-sized microtubule bundles. The stronger anchoring in the experiments constrains the $-1/2$ defects to the region inside the trench, while in simulations they are pushed into the immediate unconfined outer region, which exhibits active turbulence properties (**Fig. 7.2**a,b). In both the experiments and simulations, $+1/2$ defects are trapped between the virtual boundaries and rotate around each other.

The submersed trench not only impacts defect distribution and director orientation but also generates virtual boundaries for the velocity field, as measured by the root mean square velocity across the trench. **Fig. 7.2**e shows lower velocities in the proximity of the trench boundaries and a maximum at the trench centre. Since activity varies slightly between experimental realisations, the flow profiles are normalised by the maximum and can be compared directly to our model prediction (**Fig. 7.2**f), in which we observe a similar drop in velocity. As would be expected, we do not observe no-slip conditions at the virtual boundaries. Rather, we find a decrease to the slower velocity of the surrounding active turbulence. The decreasing flow profile in the vicinity of a boundary explains the preferential alignment of the microtubule bundles at the virtual boundary (**Fig. 7.2**c-d). Consider the contradictory situation of an orthogonal bundle midway over a boundary. The segment that is superjacent to the trench is subject to large orderly axial flow profiles, whereas the outer segment is subjected to slow inconsistent advection, resulting in a net torque that co-aligns the director with the trench edge. Though flow speeds are greater above the trench, the characteristic active nematic length scale is large, which in conjunction with confinement by the virtual boundaries, generates rapid-but-orderly flows. On the other hand, the larger friction produces a smaller characteristic length scale [68] even though speeds in the shallows are slower. Thus, the submersed micropatterned trench separates the flow states into a rapid-but-orderly flow above the trench and a slow-but-disorderly active turbulence outside.

Because the submersed micropatterned trench produces virtual boundaries that introduce a confining length scale, the competition between confinement and the intrinsic active nematic length scale can be probed. **Fig. 7.3**a experimentally support the computational result that a periodic vorticity structure is established between the virtual boundaries when the active and confining length scales coincide [50, 56, 160, 161], which is confirmed by the simulations shown in **Fig. 7.3**b. Examining the velocity-velocity spatial autocorrelation $C_v(\delta y) = \langle \vec{u}(\vec{r}, t) \cdot \vec{u}(\vec{r} + \delta y\ \hat{\boldsymbol{y}}, t) \rangle \,/\, \langle u^2 \rangle$ with a distance δy along the trench allows quantification of the different flow profiles exhibited above the trench (**Fig. 7.3**e, f; *blue curve*). The correlation function exhibits repetition between correlated and anti-correlated regions due to the repetition of clock-wise and anti-clockwise vortices. Active turbulence exists outside of the virtual channel, as characterised by an immediate initial drop in the correlation (**Fig. 7.3**f; *dashed curve*). Thus, the virtual boundaries are able to maintain distinct flow behaviours simultaneously in a single active system.

By narrowing or widening the trench, we can cause the confined flow to transition to other flow states. We confirm this with simulations (**Fig. 7.3**c-f). The narrowest trench width is $w_t = 1.2R$ (**Fig. 7.3**c), and the two wider trenches have widths of $w_t = 1.7R$ (**Fig. 7.3**b) and $6R$ (**Fig. 7.3**d), respectively. In the narrow trench (**Fig. 7.3**c), the flows are long-ranged, bidirectional and oscillatory with a preference to align with the boundaries (**Fig. 7.3**f). This oscillatory-streaming state occurs when the confining length scale w_t is small compared to the intrinsic active nematic length scale within the low-friction trench [56]. The increased trench width allows active turbulence in both the area superjacent to the trench and the shallow exterior regions (**Fig. 7.3**d) but with differing active nematic length scales (**Fig. 7.3**f).

The trench geometry demonstrates that submersed microstructure patterning can impose confining virtual boundaries and is a feasible technique for establishing different flow profiles at different locations in the active nematic layer without penetrating it, allowing for fine-tuned positional control. Unlike other control mechanisms, this allows for different flow states' coexistence within a single active film. The submersed-micropatterned-structure approach's strength is that active

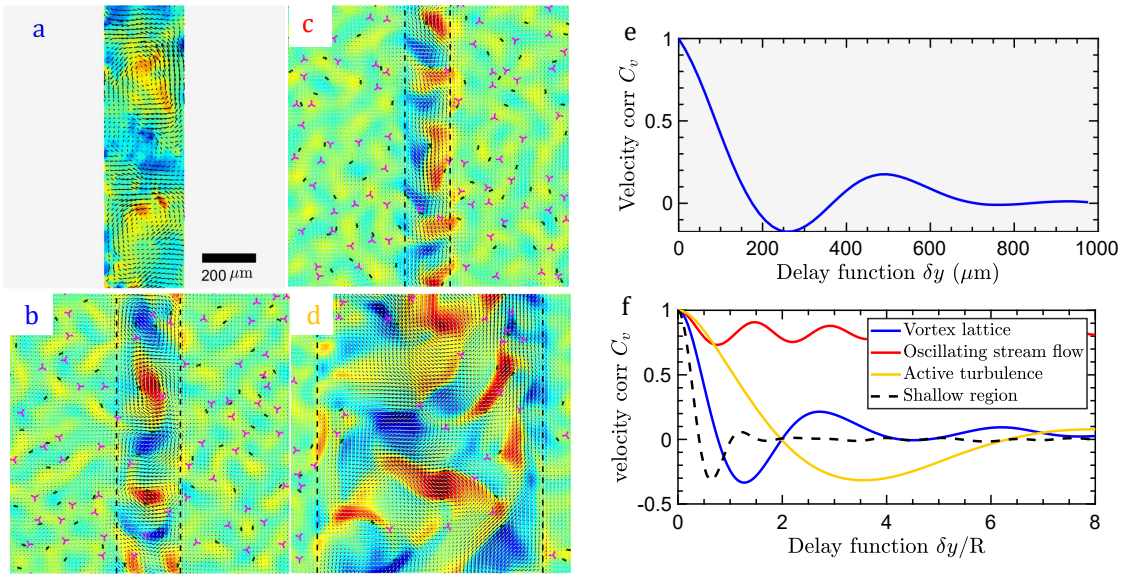

Figure 7.3: Friction boundaries result in separate flow regions. (a) Instantaneous vorticity superjacent the experimental deep trench region from PIV for a trench of width $w_t = 325\mu$m. (b) Simulation snapshot of a repeating lattice of counter-rotating vortices above a trench of width $w_t = 1.7R$. Plus-half defects (dark green) are trapped between the virtual boundaries, generating the repeating vortex structure along the centerline that is distinct from the active turbulence that exists outside the virtual boundaries, which are denoted by dashed lines. (c) Decreasing the trench width to $w_t = 1.2R$ results in long-range, oscillatory, bidirectional streaming flow inside the trench. (d) Increasing the trench width to $w_t = 6R$ results in active turbulence both inside and outside the trench region, but with differing intrinsic length scales due to the different frictions. (e) The velocity-velocity auto-correlation function for the experiment illustrated in (a), measured along the trench δy at the centerline $x = 0$ from PIV. Due to the confinement, long-range flow structures are formed in the low-friction regime epitomised by the strong correlation-anticorrelation signal. (f) Velocity-velocity auto-correlation function from the simulations shown in (b) blue, (c) red, (d) yellow and the shallow region outside the virtual channel (dashed). The blue curve displays pronounced correlation and anticorrelation indicating the counter-rotating vortex pattern in (b), which corresponds to the behaviour observed in the presented experiments in (a,e). The red curve is long-lived and fully correlated in the narrow channels (c), while the yellow curve decorrelates to zero after an anticorrelation, signalling active turbulent behaviour within the virtual boundaries as well as outside.

material does not first have to saturate a cavity before confinement dynamics can be explored [57]. Filling complex geometries with filament-based active material may be the prohibitive step in active microfluidics [59]. The proposed micropatterned method circumvents these difficulties, opening possibilities for experiments involving more complex geometries.

7.4 Submersed stairway

While the trench geometry can separate two distinct flow states into coexisting regions, the next set of experiments employs substrate micropatterns to simultaneously observe active turbulence with a gradient in characteristic length scales, all with the same ATP concentration through a stairway of submersed steps (**Fig. 7.1**d). In this case, a series of ten steps are fabricated from cytop-treated acrylic substrates through CNC milling. Individual steps have a run (horizontal width) of $w_s = 500\mu$m and steps are separated by an abrupt drop in the height of $\Delta_s = 10\mu$m. The depth of fluid between the substrate and the nematic film is $h(n) = h_0 + \Delta_s n$, where n is the step number and the initial fluid depth is determined to be $h_0 = 12 \pm 3\mu$m through confocal microscopy. **Fig. 7.1**e displays the five steps $5 \leq n \leq 9$ for which the microtubule network forms a well-defined, continuous nematic field. As the depth h increases with step number n, the effective dissipation within the oil-layer decreases, which we simulate via discrete steps in effective friction (**Fig. 7.1**f). We simulate a $(7.5 \times 50)R$ long system composed of the same number of steps as in the experimental system (10 steps) of step width $w_s = 5R$. Each step represents a different lubrication momentum dissipation region with different non-zero effective friction coefficients set to $f(n) = \frac{0.1}{1+n}$, where $n \in \{0 \dots 9\}$ denotes the different steps corresponding to a different oil depths in the experiments. We focus on the simulation data from steps $n = \{1, 2, 3, 4, 5\}$.

Above the stairway, the intrinsic active length scale increases with decreasing friction [68], which we characterise along the stairway by measuring the defect distributions (**Fig. 7.4**). In particular, the distributions are flat within each step, except at each edge, where the number densities of positive defects plunge and minus defects peak. This is consistent with the variation in defect densities at the borders of the trench (**Fig. 7.2**a,b). Numerical results show the decrease in density for both $\pm 1/2$ defects, though the peaks and dips in defect density near each edge are less pronounced than in experiments. Though the change in defect density is modest, a previous study demonstrated the difficulty in controlling defect density: Increasing oil viscosity many orders of magnitude (from 5×10^{-3} to 3×10^2Pa $\cdot$ s)

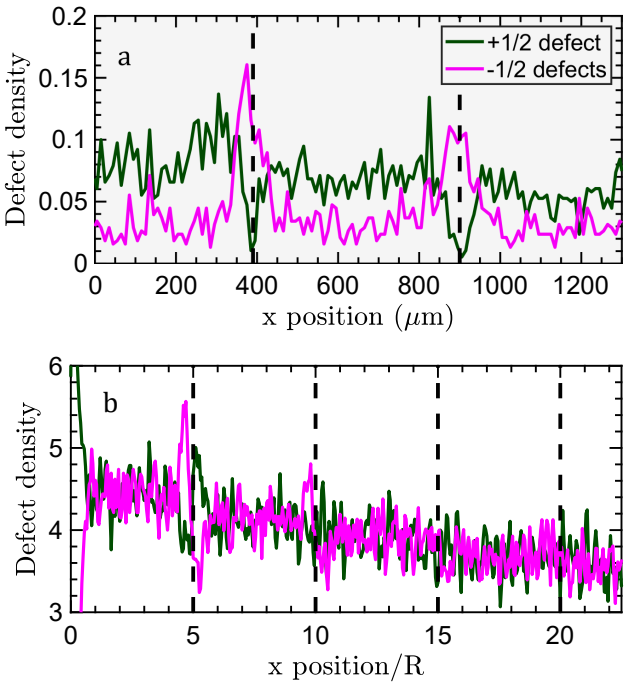

Figure 7.4: Submersed micropatterned stairway allows simultaneous coexistence of regions of separated active turbulence with differing defect densities. The $+1/2$ and $-1/2$ defect distributions as a function of position down the stairway x. (a) Measurements from experiments for steps of width $w_s = 500\mu$m (grey background) with $7 \leq n \leq 9$. (b) Measurements from simulations for steps of width $w_s = 5R$ with $1 \leq n \leq 5$ (white background).

only increased defect density by a factor of order unity [162]. This highlights the tunability convenience of our method.

Interestingly, we only observe a well-defined, continuous nematic field for oil-depths that are much greater than h_0 (lower friction regions) in both the experiments and the numerical simulations (**Fig. 7.1**d). At the highest points in the stairway (largest friction regions), the active film exhibits disorderly textures which are akin to those previously observed in experiments utilising high viscosity oils [162]. The film develops gaps, defining singularities in the nematic field becomes tenuous, and the film is not necessarily an unambiguously ordered nematic phase. This suggests that submersed micropatterned structures can do more than impact flow and orientational state. It can also influence phase and ordered active material concentration, as we will demonstrate with a final geometry.

7.5 Submersed pillar

Finally, the third set of experiments demonstrates how substrate micropatterning can be used to control active matter concentration via structures raised above the solid substrate yet still fully submersed in the underlying oil-layer. Specifically, a fully submersed pillar structure is considered (**Fig. 7.1**g). As in the trench and stairway geometries, the active nematic layer is subject to a step-change in the effective film friction. However, differentiating it from previous structures, the pillar's virtual boundary forms a closed loop. This difference contrasts the pillar geometry from the previous longitudinal ones. The most prominent effect is a pronounced dilution of active material directly above the pillar (**Fig. 7.1**h). The pillar structure demonstrates that submersed micropatterns can control active material concentration in addition to dictating and segregating flows.

The experimental SU-8 pillars have radius $r_p = 116 \pm 2\mu\text{m}$ and height $h_p = 6.8 \pm 0.3\mu\text{m}$. Similar to the trench geometry, the active nematic layer here is subject to a step-change in the effective film friction representing the viscous dissipation within the underlying oil layer, resulting in a circular virtual boundary. The experiments illustrate that this circular boundary depletes active material from the enclosed region. The behaviour is recapitulated in the simulations (**Fig. 7.1**i), in which the phase-field active material concentration ϕ demixes in the high friction region. We model the pillar with a radius $r_p = R$ of high friction and simulate a $(10 \times 10)R$ periodic system. We start to observe a depletion of active material concentration ϕ for $f = 0.07$, corresponding to the trench geometry's friction choice. However, the results presented are for a larger friction value $f = 0.5$, as that choice better matches the pronounced depletion observed experimentally (**Fig. 7.5**).

To understand the mechanism leading to the pillar-bound, dilute phase of active matter, we consider a simplified model of the active nematic hydrodynamics. The effective friction is locally large above the pillar, causing the flow speed to fall to $V \approx 0$ in the enclosed area but remain non-zero beyond the pillar border (**Fig. 7.5**a). Since nematic ordering arises due to activity-induced motion, the sharp decrease in flow causes a corresponding drop in scalar order q across the

circular virtual border (**Fig. 7.5**b). However, the abrupt gradient in scalar nematic order $q(\vec{r})$ feeds directly back into the advection since the active force density is $\vec{f}_{\mathrm{Act}}(\vec{r}) \propto \vec{\nabla} \cdot \boldsymbol{Q}(\vec{r})$ (**Eq. 2.35**). When the variation of the nematic order is dominated by the radial change in scalar order parameter and bend-induced stresses are neglected, we get an active force density $\vec{f}_{\mathrm{Act}}(\vec{r}) \approx \partial_r \zeta(\vec{r}) q(\vec{r}) \hat{\boldsymbol{r}}$. Thus, the active forcing is expected to be radially outward and sharply peaked about the interface as observed in simulations (**Fig. 7.5**c).

However, the active forces do not simply produce increased pressure across the perimeter but instead can selectively deplete the concentration of active material ϕ. Since the active film is considered incompressible, fluid mass density ρ is constant. Hence, the divergence of the film velocity is zero (**Eq. 2.27**). Thus, depletion demands that outward advection is more frequent in regions where ϕ is larger on average. This is indeed the case because the active stress depends on the local amount of active material present, $\zeta\phi(\vec{r})$ (**Eq. 2.35**), which causes the radially outward foces to be stronger in magnitude where ϕ is large. For this reason, if the surrounding active turbulence stochastically advects ϕ-rich active material across the perimeter, the local active forces increase to repulse the material from the dissipative region selectively (**Fig. 7.5**d). If a ϕ-poor fluid parcel enters the high friction region, the local active forces decrease allowing the fluid to cross the perimeter more easily. Thus, the depletion of active matter above the pillar results from the high effective friction lowering the velocity, which causes nematic melting ($q \to 0$). This causes active repulsion which selectively maintains the depletion above the pillar through the dependence of active stress on the local concentration of active material (**Fig. 7.5**e).

Although the stairway geometry's highest steps also fail to exhibited continuous nematic fields, they are not devoid of active material (**Fig. 7.1**d). whereas, depletion within the enclosed region superjacent to the pillar is far more pronounced. To explore the cause of this, we simulate a range of variations on the pillar geometry. Firstly, we consider if the virtual barriers' curvature is the significant difference by simulating a rectangular pillar (see Appendix C.7 and **Fig. C.6**). We observe a

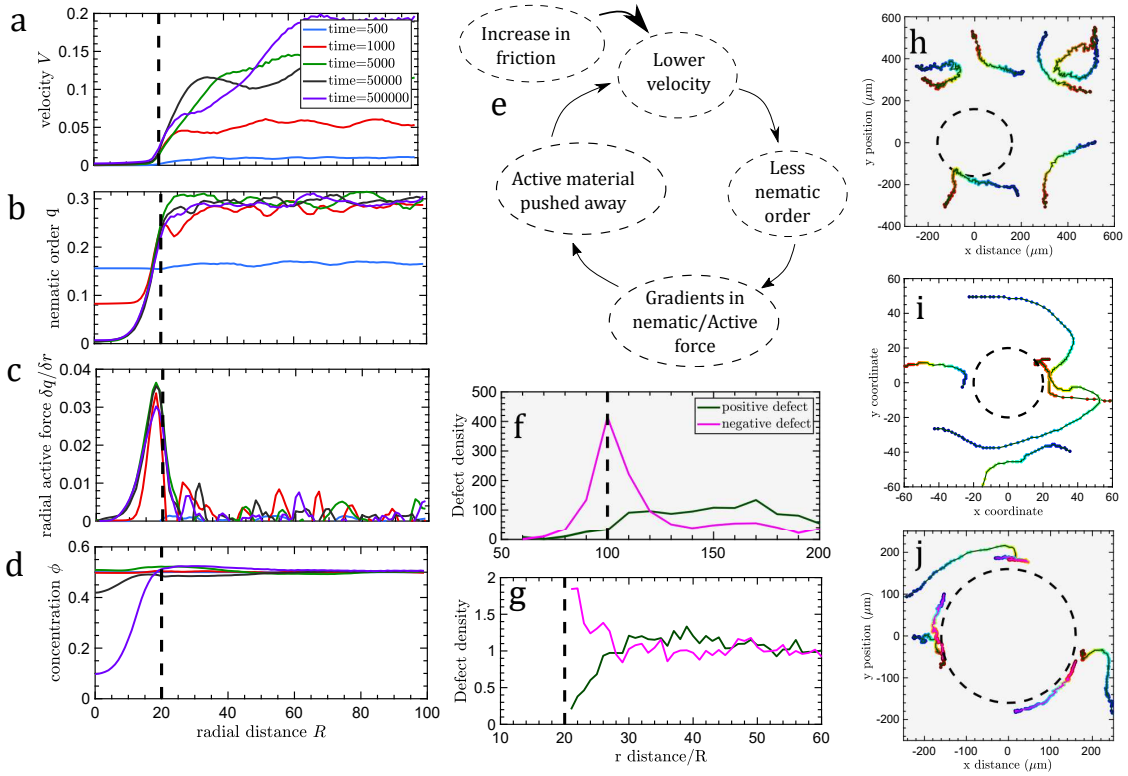

Figure 7.5: Pillars cause local high friction regions which result in active matter depletion. Panels with grey backgrounds denote experimental results, while white backgrounds denote numerical results. (a) Due to the higher friction, the flow in the active nematic film remains low. (b) The scalar order parameter q has a high value far from the pillar but a low value above it because the shear flows are less intense in the high friction region. (c) The difference in nematic order at the friction interface results in a radial active force. (d) This radial active force pushes the active material concentration outwards resulting in depletion effects. (e) Schematic explanation of (a-d). (f-g) $+1/2$ and $-1/2$ defect distributions as a function of radial distance from a submersed pillar from (f) experiments and (g) simulations. (h-j) Example xy trajectories of $+1/2$ defects dynamics in the vicinity of the pillar. Dark green (magenta) lines denote $+1/2$ ($-1/2$) defects. Time along the trajectory is displayed as circular markers coloured blue at the initial time and changing to red at the final instant. (h,i) $+1/2$ defects deflecting from the pillar; (h) experiments and (i) simulations. (j) Experimental xy trajectories of $+1/2$ defects being absorbed at the pillar boundary through defect annihilation with $-1/2$ residing in the vicinity of the perimeter.

comparable depletion of ϕ from the enclosed area and conclude that the curvature of the pillar's perimeter compared to the trench's boundaries is not the critical difference. Secondly, we consider a circular pit and find that active material accumulates in the enclosed area, consistent with the explanation of the depletion mechanism (see Appendix C.7 and **Fig. C.7**). We conclude that accumulation

or depletion of active material using submersed micropatterned structures relies on two attributes: (i) The oil-layer should be thin such that effective friction is high, suppressing the active flows which are necessary for the system to exhibit nematic order [10]. (ii) An enclosed area must be circumscribed by a virtual boundary to prohibit longitudinal active streams through the incompressibility constraint. The virtual boundaries circumference must be small compared to the intrinsic active length scale.

In addition to controlling active nematic concentration, submersed pillars can interact with defects within the superjacent nematic. We observe a greater frequency of $-1/2$ defects in the vicinity of virtual boundaries in both experiments and simulations (**Fig. 7.5**f,g). The planar anchoring of the director field explains the distribution of defects at the pillar boundary (**Fig. 7.1**h,i). The resulting bend deformation around the perimeter drives hydrodynamic instabilities to continually generate defect pairs, with newly created, self-motile $+1/2$ defects typically oriented radially away from the centre of the pillar. The self-motile $+1/2$ defects swiftly move away from the vicinity of the interface, leaving immotile $-1/2$ defects behind (**Fig. 7.2**f,g). As the active nematic length scale controls the continual pair-creation process [40, 163], we expect a steady-state increased population of $-1/2$ defects around the pillar, with a value related to the circumference of the pillar divided by the active nematic length scale.

The submersed pillar can also serve as a virtual obstacle for defect trajectories. Positive defects that approach the pillar from the surrounding turbulence stall or are deflected once in proximity to the pillar (**Fig. 7.5**h-j). Deflected $+1/2$ defects first slow as they approach the pillar, then scatter and regain speed as they move away from the submersed structure (**Fig. 7.5**h,i). Positive defects that stall as they approach the boundary temporarily hold their position before annihilating with pillar-associated $-1/2$ defects (**Fig. 7.5**j). While defects can temporarily enter the depleted area, such infrequent events are transient as the repulsive active forces (**Fig. 7.5**c) push such incursions radially outward.

7.6 Conclusion

Using a combined experimental and simulation approach, we have demonstrated in this chapter that micropatterns fully submersed in an underlying oil layer can influence the flow, topology, and even concentration of active material in a superjacent active nematic film without direct contact. By imposing changes in substrate depth, viscous dissipation in the oil layer enacts a position-dependent effective friction on the active material. Abrupt substrate height steps can constitute sharp virtual boundaries in the active matter layer, controlling flow, defect and active material behaviour. As a proof-of-concept, submersed micropatterned structures were employed. We created virtual channels with active turbulent surroundings and coexisting with different flow states determined by the confinement through trench geometries. Secondly, we showed a stairway of separated regions of active turbulence with differing characteristic length scales but the same ATP concentration or activity ζ. Lastly, we used a virtual enclosure in which activity-induced advection selectively depleted active material to produce a localised, dilute phase that could act as an obstacle that interacts with and scatters defects.

The proposed method to control active nematics opens approaches for fabricating active topological microfluidic devices. Complications associated with infiltration of active nematics into confined spaces could be avoided, and active dynamics in various geometries at the same activity could be compared directly. Furthermore, locally concentrating or depleting active material could regulate active stress at constant levels of ATP or rheological properties such as film viscosity or nematic elastic coefficients.

Please don't go. The drones need you. They look up to you.

Sid Meier's Alpha Centauri

8 Discussion

In this thesis, we investigated different methods for suppressing the emergence of active turbulence and the control of active nematics through their surroundings. Section 8.1 summarises the main findings. Section 8.2 provides an outlook for continuing the research presented in this thesis.

8.1 Summary

In Chapter 3, we investigated the transition from two-dimensional to three-dimensional meso-scale turbulence in active nematics. We employed continuum simulations to model an active nematic between two parallel planes. We found that the ratio between the intrinsic active length scale and the interplate distance determines the active nematic behaviour. The system exhibited traditional 2D active nematic turbulent flows below a given value of this ratio, confirming that active nematic films with a finite, but thin thickness can be treated like 2D active nematics. Above this ratio, the activity overcame elastic twist deformation energy costs, and we found that the active forces drove twist deformations around disclination lines, indicating a crossover to 3D turbulence.

In Chapter 4, we introduced anisotropic friction and showed that this is a possible method to control chaotic active flows. Our model revealed dynamics

similar to the experimental laning state reported by Guillamat *et al.* [12] in which microtubule-kinesin motor mixtures were put in contact with a smectic liquid crystal. In the laning state, the active nematic flowed up and down in alternating stripes, resulting in dynamical but orderly collective flows. We used this laning state to map the phenomenological model activities ζ to corresponding Adenosine triphosphate (ATP) concentrations which induced shear flows in the microtubule-kinesin mixtures. We also illustrated that the laning state only emerged in the flow-aligning regime (high flow-aligning parameter). We found that the active nematic behaved quantitatively differently in the flow-tumbling regime (low flow-aligning parameter) as pairs of oppositely charged defect pairs navigated through the system leaving behind long-lived distortions.

We followed this up by investigating an active nematic's response to different flow-aligning parameters in Chapter 5. We identified regions in the activity-flow-aligning parameter phase-space, where self-propelled $+1/2$ defects came together to form bound full-integer topological defects. We showed that the emergence of full-integer defects was caused by the director reorientating due to the self-generated active flows around the topological defects.

In Chapter 6, we introduced isotropic friction to further numerically investigate defect ordering. We showed that friction could induce ordering of defects on length scales many times larger than the intrinsic active length scale. Even in the absence of isotropic friction, we found a weak ordering of defects in the active turbulent state. Upon increasing the friction, the hydrodynamic screening length became comparable to the active length scale. $-1/2$ defects tended to reorganise themselves into a hexagonal lattice, where each hexagon encompassed two $+1/2$ defects that rotated on a vortex. However, this was not an ideal configuration for sets of oppositely charged pair defects. Consequently, the hexagonal packing of defects coexisted with a rectangular structure reminiscent of the nematic ordering of defects found experimentally by Dogic *et al.* [70]. The long-range rectangular ordering eventually dominated for the largest values of friction that could be simulated.

Lastly, we demonstrated in Chapter 7 three possibilities of using position-dependent isotropic friction to control active nematic patterns. The simulation results were accompanied by experiments, where oil submersed underlying substrate geometries induced effective friction in the superjacent active nematic film. The experiments were carried out by UC Merced, University of Massachusetts Boston and Brandeis University. It appeared that substrate height steps constituted sharp friction interfaces, which resulted in virtual hydrodynamic boundaries in the active nematic film. We demonstrated control of the active nematic dynamics by creating virtual channels using trench geometries, where active turbulence in the high friction regions coexisted with different flow states above the trench. The virtual boundaries' confinement length determined the flow state in the low friction regions. We also modelled a friction stairway that resulted in separated regions of active turbulence with varying characteristic length scales but where activity ζ remained uniform. Thirdly, we demonstrated how we could archive activity-induced advection using a virtual enclosure (a pillar), which produced a region of dilute active material. This dilute region acted as an obstacle for the motile $+1/2$ defects as $+1/2$ defects were either scattered away from the pillar or absorbed by nearby $-1/2$ defects.

8.2 Outlook

This thesis presented possible means for controlling the otherwise chaotic flows of active nematics. While several physical control mechanisms were explored, there are still many interesting open research questions. In particular, I propose three questions that would be especially interesting to explore in depth. These will be elaborated in the following paragraphs. They are: 1) Further explore the effect of the flow-aligning parameter. 2) Investigate the effect of adaptive surroundings, which are more realistic for many biological systems. 3) Expand the work on indirect control through submersed patterning.

Firstly, the work presented in Chapter 3 shows that three-dimensional active nematics will behave differently from two-dimensional active nematics as active forces will drive twist deformations around disclinations. It would be interesting to

study how the flow-aligning parameter affects disclination line dynamics. Similarly to the 2D case, it might be possible to create full-integer disclination lines or stable point structures in three-dimensions for certain flow-aligning parameters. These full-integer point defects could be long-lived once formed and impact the dynamics of active nematics.

Additionally, recent theoretical achievements have taken interesting steps in constructing multi-defect dynamic formalisms in 2D active nematics in the limit of compressible and over-damped systems [132, 137]. Incorporating shear-alignment effects within such a framework and investigating bound defect states would help construct generic defect models in wet active nematic systems.

Secondly, throughout this thesis, we have mentioned that we would like to understand how natural biological systems influence collective dynamics. Our work explained different methods to control the collective flow behaviours of active nematics through their surroundings. However, many natural biological systems have adaptive surroundings. Previous research has shown that motile cells can modify their environment. For example, individual cells can pull on and deform the extracellular matrix in order to migrate [164], and swimmers can transport passive mobile microparticles, such as nutrient particulates [165], exopolymers [166] and colloids [167]. A logical extension to the field of active nematics would be to investigate the possibility of a bidirectional relation between the collective dynamics of active particles and their material surroundings.

As we showed in Chapter 3, the collective dynamics of many swimmers can be regulated by introducing a confining length scale, *e.g.* a channel, when the collective active length scale is comparable to the confinement. Introducing deformable walls would be interesting as this reflects biological reality more closely, *e.g.* membrane fluctuations, than previous studies on confined swimmers. It might be possible that the walls' fluctuating length scale will interact with the swimmer's collective dynamics, yielding novel flow behaviours.

Research could also be initiated on the collective restructuring of porous media. There is just one (modifiable) hydrodynamic screening length in deformable channels,

but most biological systems through which bacteria move, *e.g.* biofilms or mucus, have a range of length scales. Multi-scale environments might affect collective dynamics in surprising ways as there are many pathways over different lengths. It would be interesting to investigate how environmental porosity affects collective swimmer dynamics. In turn, we could then study how collective flows modify the porosity of the environment.

Lastly, the work presented in Chapter 7 is still ongoing. The results presented suggest that more complex submersed patterns could allow for a more fine-tuned control of the active nematic behaviour. Preliminary experimental results show that gradual changes (compared to step functions) in friction can also influence defect dynamics. The experiments archive control of the defects' orientation by patterning a submersed undulating wave. This finding suggests that complex patterns could guide defect motion. Simulations could help rapidly identify functional structures as experiments are time and cost-intensive because new submersed patterns need to be manufactured for each different set-up.

Another extension of submersed patterning in oil would be for the pillars to extend through the active nematic film. The oil-water interface will form a meniscus when it touches the pillar. Early experiments suggest that the active nematic material climbs the pillar and forms a second tiered layer on top. This suggests that the curvature of active nematic films can influence the migration of active material. Following lubrication theory, we could include forces in the two-dimensional plane, which would mimic the effect of curvature. As such, we could model curved active nematic films without having to fully solve the three-dimensional system. This is a considerable simplification.

Moreover, preliminary results suggest that the active nematic layer that forms on top of the pillar behaves like an isolated region of active nematic material confined inside a circle. This isolation results in ordered dynamics on top of the pillar, coexisting with the active turbulence. This behaviour suggests another method to achieve coexistence between different collective flow states, which might also be described by a modified two-dimensional active nematic model.

This chapter gave an overview of the main results presented in the thesis on *Control of Active Nematics*. In addition, multiple future research directions were proposed: 1) Exploring the effect of the flow-aligning parameter in different systems. 2) Investigating how adaptable environments control and are influenced by active nematics. 3) Exploring the full potential of using submersed patterned surfaces to control active nematic films.

Appendices

I'll sleep when I'm dead.

Warren Zevon

A The hybrid lattice Boltzmann method

A.1 The hybrid lattice Boltzmann method

In this thesis, we evolve the density ρ and velocity $\vec{u}$ using the Navier-Stokes equations (**Eq. 2.27** and **Eq. 2.28**). These are solved using a lattice Boltzmann (LB) algorithm while the Cahn-Hillard equation for concentration ϕ (**Eq. 2.30**) and the evolution of the tensor order parameter $\boldsymbol{Q}$ (**Eq. 2.21**) are solved using a finite difference method as put forward by Marenduzzo *et al.* [102, 168].

The lattice Boltzmann algorithm is defined in terms of a set of partial Boltzmann distribution functions at each discretised lattice site $\vec{x}$ [112]. A Boltzmann distribution function $g_i(\vec{x}, t)$ represents the density of particles with a certain velocity at a certain point in time. In the algorithm, the Boltzmann distribution functions are discretised, so they only possess values at discretised lattice sites (with spacing $\Delta x = 1$) and at discrete times with time step $\Delta t = 1$.

The hybrid Boltzmann scheme has one set of distributions, $g_i(\vec{x}, t)$, where i labels a lattice direction at site $\vec{x}$ at timestep t. We use a D3Q15 grid (**Fig. A.1**), where each lattice direction i is associated with a velocity vector $\vec{e}_i$. In the D3Q15 grid, there are 3 spatial dimensions and 15 discretised velocity vectors, $\vec{e}_i = (0, 0, 0)$, $(\pm 1, 0, 0,)$, $(0, \pm 1, 0, 0)$, $(0, 0, \pm 1)$ and $(\pm 1, \pm 1, \pm 1)$.

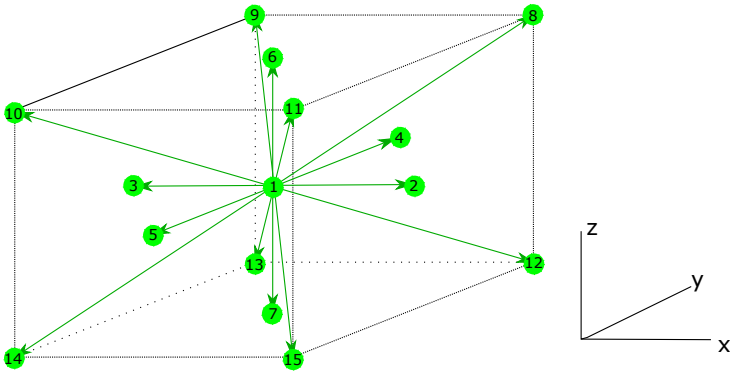

Figure A.1: The lattice geometry and lattice vectors $\vec{e}_i$ (green arrows) for the D3Q15 grid used in our lattice Boltzmann model.

The fluid density ρ and fluid momentum $\vec{u}$ are defined as moments of the distribution functions

$$\rho = \sum_i g_i, \tag{A.1}$$

$$\rho\vec{u} = \sum_i g_i \vec{e}_i. \tag{A.2}$$

The distribution functions evolve according to

$$g_i(\vec{x} + \vec{e}_i\Delta t, t + \Delta t) - g_i(\vec{x}, t) = \Delta t \left[C_g(\vec{x}, t)\right], \tag{A.3}$$

where C_g is a collision operator.

The discretised Boltzmann scheme (**Eq. A.3**) has two steps: the streaming step (left side of **Eq. A.3**) and the collision step (right side of **Eq. A.3**). In the streaming step, the distribution functions stream towards neighbouring grid positions. In the collision step, the distributions relax towards the equilibrium distributions g_i^{eq}, using a single relaxation time $\mathcal{T}$, as

$$C_g(\vec{x}, t) = -\frac{1}{\mathcal{T}}(g_i - g_i^{\mathrm{eq}}) + \vec{B}, \tag{A.4}$$

where $\vec{B}$ contains additional body forces, *e.g.* friction and off-diagonal stress terms. The equations of motion that we indirectly solve with **Eq. A.3**, follow from the choice of the equilibrium distribution moments g_i^{eq}. We constrain g_i^{eq} as

$$\begin{aligned} \sum_i g_i^{\mathrm{eq}} &= \rho, \\ \sum_i g_i^{\mathrm{eq}} \vec{e}_i &= \rho\vec{u}, \\ \sum_i g_i^{\mathrm{eq}} \vec{e}_i\vec{e}_i &= -\boldsymbol{\mathcal{S}} + \rho\vec{u}\vec{u}, \end{aligned} \tag{A.5}$$

with $\boldsymbol{\mathcal{S}}$ the symmetric part of the stress tensor $\boldsymbol{\Pi}$ in the momentum equation **Eq. 2.28**. With this constrain, we can map **Eq. A.3** to the Navier-Stokes equations (**Eq. 2.27** and **Eq. 2.28**) using a Chapman-Enskog Analysis [102, 112]. The zeroth and first moments of g_i^{eq} ensure that mass and momentum are conserved. The second moment of g_i^{eq} describes momentum dissipation and contains the viscous stress as well as the symmetric part of the additional active strss (**Eq. 2.35**), elastic strss (**Eq. 2.29**) and the stress due to concentration differences (**Eq. 2.31**). The conditions in **Eq. A.5** can be satisfied by writing the distribution functions as polynomial expansions in the velocity (see for instance [102]).

The antisymmetric parts of the stress tensor and the friction $\boldsymbol{f} \cdot \vec{u}$ (**Eq. 2.28**) are added as body forces $\vec{B}$. This only gives a first-order accuracy, but this is enough for most of this thesis as these terms are small compared to the symmetric components of the stress tensor. However, we use a more accurate forcing scheme in Chapter 7, where we model sharp friction interfaces. In that chapter, we use the forcing method proposed by Guo *et al.* [169].

The strength of using LB is that **Eq. A.3** is a first-order solving scheme, but it has second-order accuracy (without the body forces) as a predictor-corrector type scheme can be mapped onto it [102, 112]. This allows us to do a rather accurate computation yet with an acceptable computation time.

The equations of concentration ϕ (**Eq. 2.30**) and tensor order parameter $\boldsymbol{Q}$ (**Eq. 2.21**) are solved simultaneously using a Runge-Kutta (RK4) method [170]. This hybrid lattice Boltzmann scheme [102] can be compared to the full lattice Boltzmann approach, where all variables are discretised into Boltzmann distributions. The hybrid method reduces computational costs significantly, as we only need to solve one set of fifteen Boltzmann distribution functions compared to seven sets of fifteen distribution functions needed with the full lattice Boltzmann method. [171]. Additionally, we avoid the error terms arising from connecting the lattice Boltzmann model to the tensor order parameter [102].

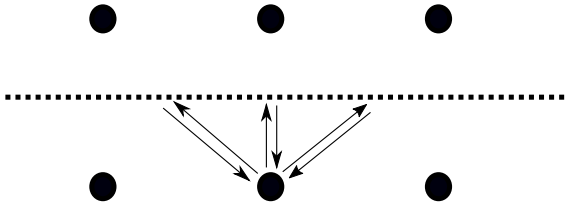

Figure A.2: Schematic representation of the bounce-back algorithm. The dotted line represents a wall which is located between lattice Boltzmann sites (black circles). At the lattice Boltzmann streaming step, the Boltzmann distribution functions that encounter the wall while streaming bounce back to their original lattice site.

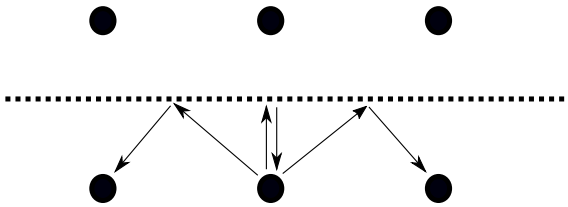

Figure A.3: Schematic representation of the full-slip boundary. The dotted line represents a wall which is located between lattice Boltzmann sites (black circles). The normal components of the Boltzmann distribution functions are reversed during the streaming step when encountering a wall (black arrows).

A.2 Wall boundary conditions

A.2.1 Flow field boundary conditions

In Chapter 3, we restrict ourselves to two types of boundary conditions on walls for the flow field: no-slip boundary conditions and free-slip boundary conditions. Walls are implemented as effectively residing between two lattice Boltzmann lattice sites.

No-slip boundary conditions are implemented by demanding Dirichlet boundary conditions at the walls,

$$\vec{u} = \vec{0}. \tag{A.6}$$

We implement this condition with a bounce-back algorithm (**Fig. A.2**). When a Boltzmann distribution function encounters a wall during the lattice Boltzmann streaming step, it bounces back to its original lattice site.

Full-slip boundary conditions are implemented by demanding Dirichlet boundary conditions on the velocity components perpendicular to the walls,

$$u_{\perp} = 0, \tag{A.7}$$

and Neuman boundary conditions on the velocity components parallel to the walls,

$$\frac{\mathrm{d}u_{\parallel}}{\mathrm{d}x_{\parallel}} = 0. \tag{A.8}$$

A schematic representation of the implementation is given in **Fig. A.3**. The normal components of the Boltzmann distribution functions are reversed during the streaming step when encountering a wall.

A.2.2 Director field boundary conditions

When planar anchoring is applied to a two-dimensional wall, the director is allowed to rotate freely planar to the wall, but reorientations perpendicular to the wall are penalised. To implement this, we add additional free energy terms at sites in contact with walls. We add a Rapini-Papoular-like free energy term which penalises the director field $\boldsymbol{n}$ pointing perpendicular to the surface,

$$\mathcal{F} = c_1 \vec{k}\boldsymbol{Q}\vec{k} + c_1(\vec{k}\boldsymbol{Q}\vec{k})^2 + c_3 \vec{k}\boldsymbol{Q}^2\vec{k}, \tag{A.9}$$

where $\vec{k}$ is the normal to the wall. Here c_i are constants which signify the strength of the anchoring. The effective anchoring strength can be compared to a Rapini-Papoular energy [172]:

$$\frac{2}{3}q(3c_1 + (c_3 - 2c_2)q). \tag{A.10}$$

In Chapter 3, we take high values ($c_1 = 0.01, c_2 = 0.001, c_3 = 0.005$) when we use strong planar anchoring conditions. In addition, we always use Neumann boundary conditions for the tensor order parameter to set gradients to zero [172].

Duty is heavy as a mountain, death is light as a feather.

Imperial Rescript to Soldiers and Sailors.

B Defect detection

B.1 Topological defects

Topological defects in a two-dimension plane are detected by calculating the winding number [124, 127]. The algorithm to detect the defects goes over all sets of four lattice points, forming a two by two square. A $+1/2$ $(-1/2)$ defect is detected if the director changes its orientation by π $(-\pi)$ stepping around the four corners of the square in a clockwise direction.

B.2 Disclination lines

Disclination lines are detected with the topological defect detection method described in [124]. We examine if a disclination line has passed through a two by two square of neighbouring grid points. We accomplish this by examining the projection of the director to the three-dimensional orientation space (**Fig. B.1**) at every lattice point. Every lattice point has two corresponding projections as the director is unidirectional ($\boldsymbol{n}$ and $-\boldsymbol{n}$). We perform a closed walk over the four neighbours' director projection, and at every step, we take the next closest director configuration (**Fig. B.1**). When we are back at the initial starting point, we either have returned to the original director orientation (**Fig. B.1**b) or to the other side of the orientation sphere (**Fig. B.1**a). If the latter, then a half-integer disclination line has passed

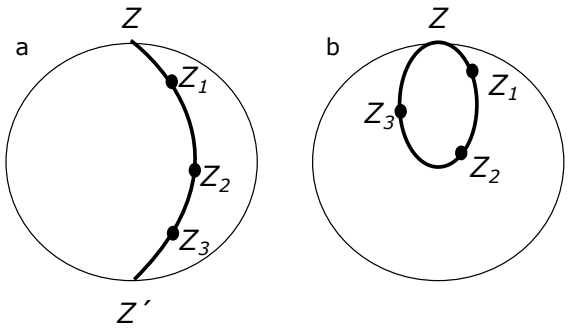

Figure B.1: Detection of disclination lines. The representation of the director $\boldsymbol{n}$ in the three-dimensional spherical space. The director has two projections ($\vec{n}$ and $-\vec{n}$). We take one of these projections Z at a lattice site. We make a closed walk over neighbouring two by two lattice points (to Z_1, Z_2, Z_3 and then either back to Z or Z'), where we always take the new director projection with the smallest angle difference. After the closed walk, the director projection is either (a) opposite to that of the starting vector Z' or (b) on the same vector Z. If we ended up at Z' a half-integer disclination passed through the four lattice sites.

through this two by two grid and we have a disclination core between the four points. If the former, no disclination line is present, or a full disclination line has passed through. We saw no indication in our simulations that full integer charged disclinations had formed (which can be detected with other methods [124]).

A disclination line has to cross two grid planes for every two by two by two lattice cube (getting in and out of the cube). By tracking disclination cores that share a lattice cube, we can connect the disclination cores to recreate the full disclination line. We measure the disclination line direction at a disclination core by taking the derivatives of the surrounding two disclination cores [124].

The characteristic disclination angle α is the angle between the rotation vector and the disclination line direction [124]. We can calculate this rotation vector by summing the vector cross products formed from each consecutive pair of the four directors around the disclination core.

And now his watch is ended

George R.R. Martin *A Feast for Crows*

C

Additional comments and measurements

C.1 Inclusion of Landau-de Gennes free energy

Throughout this thesis, we keep a non-zero bulk free energy $\mathcal{F}_b$, which allows us to set relaxation dynamics in the absence of shear flows even though we work in non-equilibrium systems. One of the reasons for this is that when we calculate the scalar nematic order parameter q from **Eq. 2.6** with only the additional active free energy terms in **Eq. 2.38**, we find that the q is independent of activity ζ. This behaviour is not seen in experimental systems where, for example, Adenosine triphosphate (ATP) is needed to generate nematic symmetry in microtubule-kinesin mixtures through shear flows [10]. Additionally, the relaxation dynamics becomes ill-defined in the limit $\zeta \to 0$ without a Landau-de Gennes bulk free energy $\mathcal{F}_b$. Lastly, active hydrodynamic interactions can result in realignment terms in the tensor equation **Eq. 2.21**. To first order in $\boldsymbol{Q}$, the active realignment term is $\lambda_\zeta \boldsymbol{Q}$ [173], which can be seen as a modification to the active nematic equilibrium properties (as it does not depend on the presence of shear flows) and this term is absorbed into the homogeneous bulk equation $\mathcal{F}_b$ [102]. Hence, we retain a non-zero bulk free energy $\mathcal{F}_b$ throughout the thesis.

C.2 Flow field around bound defects

Using the linearity of Stokes equation, we can find the contractile flow field associated with two defects in a vortex-like structure separated by a distance of $2x$ (Chapter 5). We do this by superimposing the analytical flow fields (**Eq. 2.45**) of each individual $+1/2$ defect [32]. We neglect additional deformations and resulting active forces in the director field due to the presence of other defects. The resulting flow profile around a bound defect pair becomes

$$\vec{v} = \begin{bmatrix} -|\zeta|\left(3(r_2 - r_1) + r_1\cos(2\psi_1) - r_2\cos(2\psi_2)\right) \\ -|\zeta|\left(r_1\sin(2\psi_1) - r_2\sin(2\psi_2)\right) \end{bmatrix}, \tag{C.1}$$

as reported in Chapter 5 (**Eq. 5.1**). Here $r_{1,2}$ and $\psi_{1,2}$ are the polar coordinates around defect 1 or 2 at the coordinates $(x, 0)$ and $(-x, 0)$ with defect orientations $\psi_1 = \pi$ and $\psi_2 = 0$. We lost the integration constant R found in **Eq. 2.45** as the boundary condition of one defect is set by the presence of the other defect. An identical flow field is found for the extensile aster-like configuration when using defect orientations $\psi_1 = 0$ and $\psi_2 = \pi$. Hence, we find the same flow profiles for a contractile and extensile system when the defects are in the vortex-like or aster-like configuration, respectively.

We confirm that this analytical flow profile (**Eq. C.1**) is found around bound defects in our simulations. When we measure the average velocity profile around bound defects, we recover a similar dipole flow profile for the contractile vortex bound defects and the extensile aster bound defects (**Fig. C.1**).

We perform this measurement by averaging the flow profiles around all defect pairs with a separation distance less than 10 LB units, and with orientation differences $\psi_1 - \psi_2$ between $(170 - 190)°$. The frame of reference is rotated so that both defects lie on the x-axis.

C.3 Axis of flow deformation

In the flow-aligning regime, the director aligns to the principal axis of flow deformation with a Leslie angle dependent on the flow-aligning parameter $\nu = \frac{\lambda}{\frac{9q}{3q+4}}$

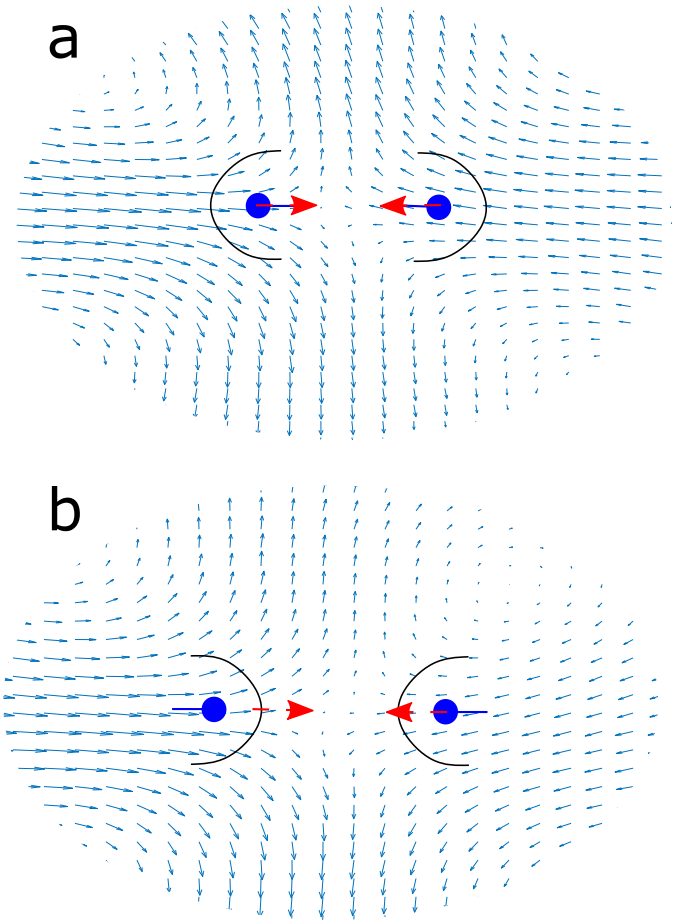

Figure C.1: The measured average flow profile around: (a) contractile vortex bound defects and (b) extensile aster bound defects. Schematic drawing of defects indicate their head-to-tail alignment $\vec{p}$ (blue solid line) and their self-propelled velocity (red arrow).

(**Eq. 2.24**). In the limit of $\nu \to \infty$ ($\nu \to -\infty$), the director lies parallel (perpendicular) to the principal axis of flow deformation [52].

We can find the principal axis of flow deformation from the strain tensor $\boldsymbol{E}$ of the active flows. The angle of this axis is defined as $\theta_P = \frac{1}{2}\tan^{-1}\frac{2E_{xy}}{E_{xx}-E_{yy}}$ in 2D (**Eq. 2.25**). Using the analytical flow profile around a bound defect pair (**Eq. 5.1**), the angle of the principal axis of flow deformation around the bound defect is then

$$\theta_P = \frac{1}{2}\tan^{-1}\left[\begin{array}{c}\Big((a+x)r_1\sin(2\theta_2)+(a-x)r_2\sin(2\theta_1)\\ +3y(r_1-r_2)+yr_1\cos(2\theta_2)-yr_2\cos(2\theta_1)\Big)\Big/\\ \Big(a(r_1+r_2)+(a+x)r_1\cos(2\theta_2)+(a-x)r_2\cos(2\theta_1)\\ +3x(r_1-r_2)-2yr_1\sin(2\theta_2)+yr_2\sin(2\theta_1)\Big)\end{array}\right]. \quad \text{(C.2)}$$

When $|\nu| \to \infty$, the director lies parallel (perpendicular) to the principal axis

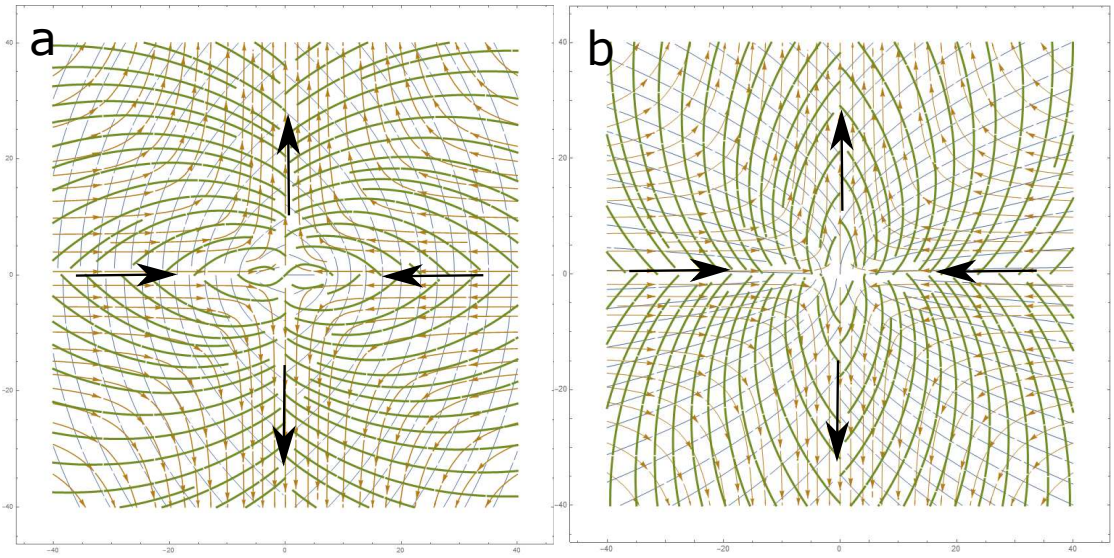

Figure C.2: Analytical prediction of director reconfiguration in response to active flows of $+1/2$ defect pairs in the limit of $\nu \to \pm\infty$. (a) Initial vortex-like configuration for contractile activity and $\nu \to +\infty$. (b) Initial aster-like configuration for extensile activity and $\nu \to -\infty$. Blue dotted lines indicate the initial director field and their associated flow fields are illustrated with the orange streamlines. The green dotted lines indicate the expected reconfiguration of the director field in response to the active flows in the limit of $|\nu| \to 1$. The resulting active forces along the x-axis and y-axis (black arrows) lead to unstable defect pair configurations as the defects will rotate around each other.

if ν is positive (negative). This results in a preferred director field as depicted in **Fig. C.2** for the bound defect state (**Eq. 5.1**). We find splay deformations along the axis, resulting in active forces (black arrows) that are aligned with the flows for the contractile and extensile cases. This means that bound defects become unstable for this flow-aligning parameter as $+1/2$ defects are pulled along the x-axis and pushed along the y-axis, which causes the defects to rotate around each other.

However, when we decrease $|\nu|$, the director aligns with a Leslie angle with respect to the principal axis of flow deformation (**Eq. 2.24**), where the vorticity sets the rotation direction. The maximum stable angle is $\theta_P = \pi/4$ at the crossover from flow-tumbling to flow-aligning when $|\nu| \to 1$ for shear flows. As the director reorientates to this angle, we recover the bound defect state configuration, causing a positive feedback (**Fig. 5.2**). Hence, the bound defect is stable for $|\nu| \to 1$.

This explains why the bound defect density decreases for high flow-aligning parameters. Once the Leslie angle becomes too small, the configuration goes from

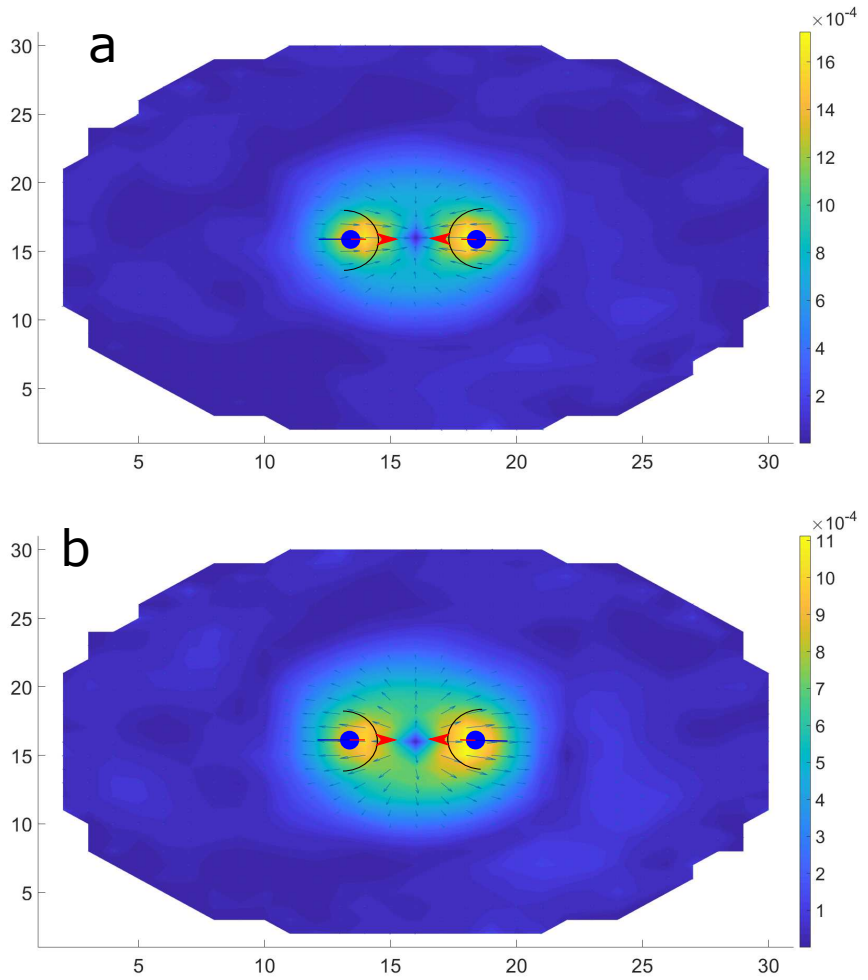

Figure C.3: The average dominant forces around bound defects for the parameter values $\zeta = 0.025$ and $\nu = -1.2$. (a) The active forces act as an attractive forces. (b) The elastic forces counteract activity-induced attraction. Colormap denotes the magnitude of the forces and the arrows denote the force directions.

a stable state that favours the bound defect state, as depicted in Chapter 5, to the director field where the defect positions are unstable with respect to each other, as depicted in **Fig. C.2**.

C.4 Dominant forces around bound defects

Using the same procedure for finding the average velocity profile (Appendix C.2), we measure the average forces around bound defects (**Fig. C.3**). We confirm that the active forces act as the attractive forces, and the elastic interactions act as repulsive forces causing a stable bound state (**Fig. 5.5**c).

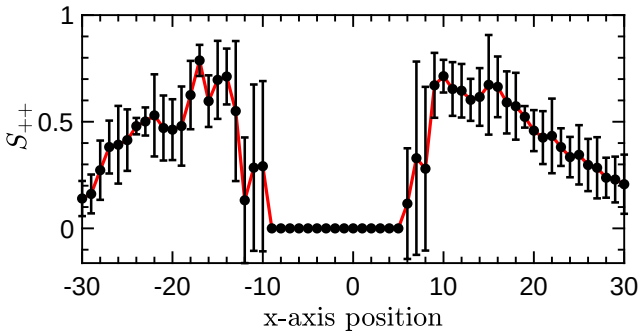

Figure C.4: Orientational distribution function S_{++} along the x-axis with the associated error for $F = 0.023$. The typical error $\sim 10\%$.

C.5 Statistics of the orientation distribution function

Fig. C.4 shows the error of an orientational distribution function, S_{++}, defined in **Eq. 6.2**, for specific coordinates along the x-axis for friction $F = 0.023$. The typical error per lattice site is $\sim 10\%$. This error size is similar for all measurements in Chapter 6. We find that the error is relatively large per lattice site as the number of defects that occupy a specific lattice site will be small. This is why we emphasise that the numerics are demanding. The number of defect pairs per simulation needs to be over 10^6 to obtain satisfactory statistics, significantly higher than in previous works studying defect behaviours. In addition, to avoid statistically insignificant data, we set $g(r, \theta) = 0$ and $\vec{S}(r, \theta) = 0$ when the defect count for any site (r, θ) is lower then 5, which would otherwise result in $g(r, \theta) < 0.1$ and an undefined $\vec{S}(r, \theta)$ value.

C.6 Finite-size effects of the orientation distribution function

In Chapter 6, we present results for a system of size $L \times L = 250 \times 250$, which is ~ 15 times the active length-scale. The effect of friction on the nematic ordering of the defects S_d is measured in **Fig. 6.3**e. The range of the ordering increases and spans the system size for $F \sim 0.11$. We now try to establish whether we measure a true transition, corresponding to infinite range ordering, by obtaining results for

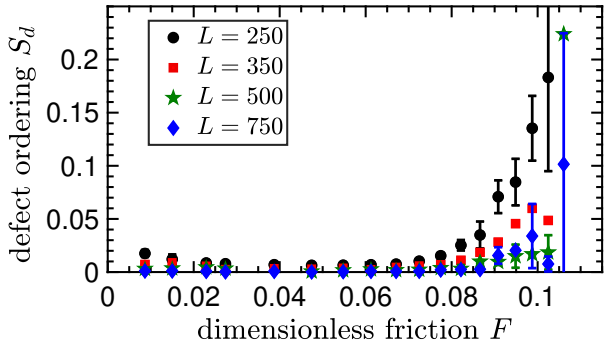

Figure C.5: Nematic order of the defects S_d as a function of friction for different system sizes L. The system size is varied from 250 by 250 ($\sim$ 15 times the active length scale) to 750 by 750 ($\sim$ 45 times the active length scale).

larger systems. These are very demanding simulations because of the large system sizes and the slow defect dynamics in these high friction regimes.

Results for system sizes up to $L = 750$, $\sim$ 45 times the active length scale, are shown in **Fig. C.5**. The ordering decreases with increasing L, showing that we observe coexisting domains with long-range, but not infinite-range order for at least these friction values. At yet higher frictions, the dynamics become too slow to allow feasible simulations. As is common in glassy systems, we cannot tell whether there is a true transition for higher friction values because of the very long time scales involved in defect rearrangements.

C.7 Additional depletion geometries

We observe a comparable depletion of concentration ϕ from the enclosed area when using a rectangular pillar (**Fig. C.6**) or a circular pillar (**Fig. 7.5**). Hence, we conclude that the pillar's curvature compared to the trench's boundaries is not the critical difference that causes depletion in the pillar geometry. We also consider an effective circular pit (**Fig. C.7**) and observe that active material accumulates in the enclosed area, consistent with the explanation of the depletion mechanism of Chapter 7.

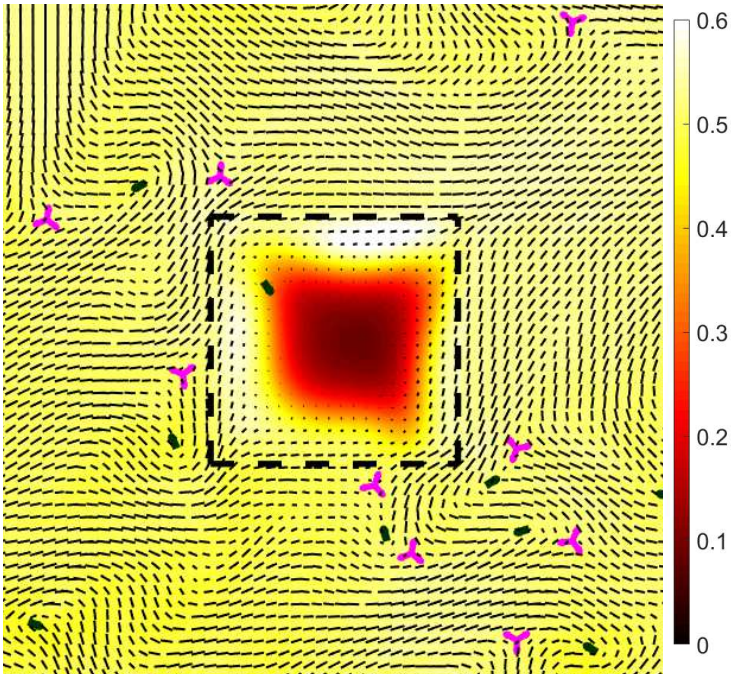

Figure C.6: Rectangular pillar causes depletion. When we apply high friction ($f = 0.5$) to a rectangular region (between the dashed lines), we observe a depletion of active material concentration ϕ (denoted by colour map).

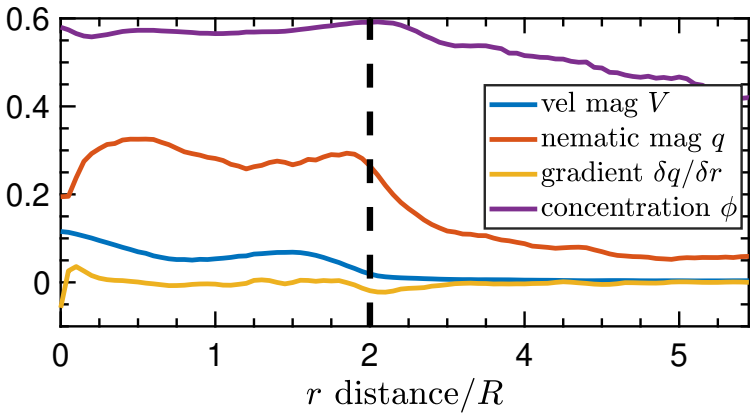

Figure C.7: We consider a circular pit where frictional damping ($f = 0.1$) is applied outside the circle $r > 2R$ (denoted with the dashed line). We observe accumulation of active material ϕ in the enclosed area, consistent with the explanation of the depletion mechanism of Chapter 7.

If I have seen further it is by standing on the shoulders of giants.

Isaac Newton

Bibliography

1. Purcell, E. M. Life at low Reynolds number. *American journal of physics* **45,** 3–11 (1977).
2. Bialek, W., Cavagna, A., Giardina, I., Mora, T., Silvestri, E., Viale, M. & Walczak, A. M. Statistical mechanics for natural flocks of birds. *PNAS* **109,** 4786–4791 (2012).
3. Becco, C., Vandewalle, N., Delcourt, J. & Poncin, P. Experimental evidences of a structural and dynamical transition in fish school. *Physica A: Statistical Mechanics and its Applications* **367,** 487 –493 (2006).
4. Volfson, D., Cookson, S., Hasty, J. & Tsimring, L. S. Biomechanical ordering of dense cell populations. *PNAS* **105,** 15346–15351 (2008).
5. Doostmohammadi, A., Thampi, S. P. & Yeomans, J. M. Defect-mediated morphologies in growing cell colonies. *Phys. Rev. Lett.* **117,** 048102 (2016).
6. Li, H., Shi, X.-q., Huang, M., Chen, X., Xiao, M., Liu, C., Chaté, H. & Zhang, H. Data-driven quantitative modeling of bacterial active nematics. *PNAS* **116,** 777–785 (2019).
7. Duclos, G., Erlenkämper, C., Joanny, J. & Silberzan, P. Topological defects in confined populations of spindle-shaped cells. *Nat. Phys.* **13,** 58–62 (2017).
8. Saw, T. B., Doostmohammadi, A., Nier, V., Kocgozlu, L., Thampi, S., Toyama, Y., Marcq, P., Lim, C. T., Yeomans, J. M. & Ladoux, B. Topological defects in epithelia govern cell death and extrusion. *Nature* **544,** 212–216 (2017).
9. Kawaguchi, K., Kageyama, R. & Sano, M. Topological defects control collective dynamics in neural progenitor cell cultures. *Nature* **545,** 327–331 (2017).
10. Sanchez, T., Chen, D. T. N., DeCamp, S. J., Heymann, M. & Dogic, Z. Spontaneous motion in hierarchically assembled active matter. *Nature* **491,** 431–434 (2012).
11. Keber, F. C., Loiseau, E., Sanchez, T., DeCamp, S. J, Giomi, L., Bowick, M. J., Marchetti, M. C., Dogic, Z. & Bausch, A. R. Topology and dynamics of active nematic vesicles. *Science* **345,** 1135–1139 (2014).
12. Guillamat, P., Ignés-Mullol, J. & Sagués, F. Control of active liquid crystals with a magnetic field. *PNAS* **113,** 5498–5502 (2016).
13. Kumar, N., Zhang, R., de Pablo, J. J. & Gardel, M. L. Tunable structure and dynamics of active liquid crystals. *Science Advances* **4,** eaat7779 (2018).
14. Reynolds, C. W. Flocks, Herds and Schools: A Distributed Behavioral Model. *SIGGRAPH Comput. Graph.* **21,** 25–34 (1987).
15. Vicsek, T., Czirók, A., Ben-Jacob, E., Cohen, I. & Shochet, O. Novel type of phase transition in a system of self-driven particles. *Phys. Rev. Lett.* **75,** 1226 (1995).

16. Toner, J. & Tu, Y. Flocks, herds, and schools: A quantitative theory of flocking. *Phys. Rev. E* **58,** 4828–4858 (1998).

17. Toner, J. & Tu, Y. Long-Range Order in a Two-Dimensional Dynamical XY Model: How Birds Fly Together. *Phys. Rev. Lett.* **75,** 4326–4329 (1995).

18. Marchetti, M. C., Joanny, J.-F., Ramaswamy, S., Liverpool, T. B., Prost, J., Rao, M. & Simha, R. A. Hydrodynamics of soft active matter. *Reviews of Modern Physics* **85,** 1143 (2013).

19. Pooley, C., Alexander, G. & Yeomans, J. Hydrodynamic interaction between two swimmers at low Reynolds number. *Physical review letters* **99,** 228103 (2007).

20. Simha, R. A. & Ramaswamy, S. Hydrodynamic fluctuations and instabilities in ordered suspensions of self-propelled particles. *Phys. Rev. Lett.* **89,** 058101 (2002).

21. Ramaswamy, S. The Mechanics and Statistics of Active Matter. *Annu. Rev. Cond. Mat. Phys.* **1,** 323–345 (2010).

22. Dombrowski, C., Cisneros, L., Chatkaew, S., Goldstein, R. E. & Kessler, J. O. Self-concentration and large-scale coherence in bacterial dynamics. *Physical review letters* **93,** 098103 (2004).

23. Sumino, Y., Nagai, K. H., Shitaka, Y., Tanaka, D., Yoshikawa, K., Chaté, H. & Oiwa, K. Large-scale vortex lattice emerging from collectively moving microtubules. *Nature* **483,** 448–452 (2012).

24. Doostmohammadi, A., Ignés-Mullol, J., Yeomans, J. M. & Sagués, F. Active nematics. *Nat. Comm.* **9,** 1–13 (2018).

25. De Gennes, P.-G. & Prost, J. *The physics of liquid crystals* (Oxford university press, 1993).

26. Bechinger, C., Di Leonardo, R., Löwen, H., Reichhardt, C., Volpe, G. & Volpe, G. Active particles in complex and crowded environments. *Rev. Mod. Phys.* **88,** 045006 (2016).

27. Jülicher, F., Grill, S. W. & Salbreux, G. Hydrodynamic theory of active matter. *Reports on Progress in Physics* **81,** 076601 (2018).

28. Guillamat, P., Ignés-Mullol, J. & Sagués, F. Taming active turbulence with patterned soft interfaces. *Nature communications* **8,** 1–8 (2017).

29. Meacock, O. J., Doostmohammadi, A., Foster, K. R., Yeomans, J. M. & Durham, W. M. Bacteria solve the problem of crowding by moving slowly. *arXiv preprint arXiv:2008.07915* (2020).

30. Blanch-Mercader, C, Yashunsky, V, Garcia, S, Duclos, G, Giomi, L & Silberzan, P. Turbulent dynamics of epithelial cell cultures. *Physical review letters* **120,** 208101 (2018).

31. Meyer, R. B. On the existence of even indexed disclinations in nematic liquid crystals. *The Philosophical Magazine: A Journal of Theoretical Experimental and Applied Physics* **27,** 405–424 (1973).

32. Giomi, L., Bowick, M. J., Mishra, P., Sknepnek, R. & Cristina Marchetti, M. Defect dynamics in active nematics. *Philosophical Transactions of the Royal Society A: Mathematical, Physical and Engineering Sciences* **372,** 20130365 (2014).

33. Livshits, A., Shani-Zerbib, L., Maroudas-Sacks, Y., Braun, E. & Keren, K. Structural inheritance of the actin cytoskeletal organization determines the body axis in regenerating hydra. *Cell reports* **18,** 1410–1421 (2017).

34. Maroudas-Sacks, Y., Garion, L., Shani-Zerbib, L., Livshits, A., Braun, E. & Keren, K. Topological defects in the nematic order of actin fibers as organization centers of Hydra morphogenesis. *bioRxiv* (2020).

35. Yaman, Y. I., Demir, E., Vetter, R. & Kocabas, A. Emergence of active nematics in chaining bacterial biofilms. *Nature communications* **10,** 1–9 (2019).

36. Ramaswamy, S. & Rao, M. Active-filament hydrodynamics: instabilities, boundary conditions and rheology. *New J. Phys.* **9,** 423 (2007).

37. Wensink, H. H., Dunkel, J., Heidenreich, S., Drescher, K., Goldstein, R. E., Löwen, H. & Yeomans, J. M. Meso-scale turbulence in living fluids. *PNAS* **109,** 14308–14313 (2012).

38. Giomi, L., Bowick, M. J., Ma, X. & Marchetti, M. C. Defect Annihilation and Proliferation in Active Nematics. *Phys. Rev. Lett.* **110,** 228101 (2013).

39. Thampi, S. P., Golestanian, R. & Yeomans, J. M. Velocity Correlations in an Active Nematic. *Phys. Rev. Lett.* **111,** 118101 (2013).

40. Martínez-Prat, B., Ignés-Mullol, J., Casademunt, J. & Sagués, F. Selection mechanism at the onset of active turbulence. *Nature Physics* **15,** 362–366 (2019).

41. Tan, A. J., Roberts, E., Smith, S. A., Olvera, U. A., Arteaga, J., Fortini, S., Mitchell, K. A. & Hirst, L. S. Topological chaos in active nematics. *Nature Physics* **15,** 1033–1039 (2019).

42. Giomi, L. Geometry and Topology of Turbulence in Active Nematics. *Phys. Rev. X* **5,** 031003 (2015).

43. Avila, K., Moxey, D., de Lozar, A., Avila, M., Barkley, D. & Hof, B. The Onset of Turbulence in Pipe Flow. *Science* **333,** 192–196 (2011).

44. Shi, X. & Ma, Y. Topological structure dynamics revealing collective evolution in active nematics. *Nat. Commun.* **4,** 3013 (2013).

45. Thampi, S. P., Golestanian, R. & Yeomans, J. M. Vorticity, defects and correlations in active turbulence. *Philosophical Transactions of the Royal Society A: Mathematical, Physical and Engineering Sciences* **372,** 20130366 (2014).

46. Hemingway, E. J., Mishra, P., Marchetti, M. C. & Fielding, S. M. Correlation lengths in hydrodynamic models of active nematics. *Soft Matter* **12,** 7943–7952 (2016).

47. Doostmohammadi, A., Adamer, M. F., Thampi, S. P. & Yeomans, J. M. Stabilization of active matter by flow-vortex lattices and defect ordering. *Nat. Comm.* **7,** 10557 (2016).

48. Chen, C., Liu, S., Shi, X., Chaté, H. & Wu, Y. Weak synchronization and large-scale collective oscillation in dense bacterial suspensions. *Nature* (2017).

49. Thampi, S. P., Doostmohammadi, A., Shendruk, T. N., Golestanian, R. & Yeomans, J. M. Active micromachines: Microfluidics powered by mesoscale turbulence. *Science advances* **2,** e1501854 (2016).

50. Wioland, H., Lushi, E. & Goldstein, R. E. Directed collective motion of bacteria under channel confinement. *New Journal of Physics* **18,** 075002 (2016).

51. Edwards, S. & Yeomans, J. M. Spontaneous Flow States in Active Nematics: A Unified Picture. *Europhys. Lett.* **85,** 18008 (2009).

52. Voituriez, R, Joanny, J.-F. & Prost, J. Spontaneous flow transition in active polar gels. *Eur. Phys. Lett.* **70,** 404 (2005).

53. Doostmohammadi, A., Shendruk, T. N., Thijssen, K. & Yeomans, J. M. Onset of meso-scale turbulence in active nematics. *Nat. Comm.* **8,** 1–7 (2017).

54. Notbohm, J., Banerjee, S., Utuje, K. J. C., Gweon, B., Jang, H., Park, Y., Shin, J., Butler, J. P., Fredberg, J. J. & Marchetti, M. C. Cellular contraction and polarization drive collective cellular motion. *Biophys. J.* **110,** 2729 (2016).

55. Pearce, D. J. G., Ellis, P. W., Fernandez-Nieves, A. & Giomi, L. Geometrical Control of Active Turbulence in Curved Topographies. *Phys. Rev. Lett.* **122,** 168002 (2019).

56. Shendruk, T. N., Doostmohammadi, A., Thijssen, K. & Yeomans, J. M. Dancing disclinations in confined active nematics. *Soft Matter* **13,** 3853–3862 (2017).

57. Opathalage, A., Norton, M. M., Juniper, M. P. N., Langeslay, B., Aghvami, S. A., Fraden, S. & Dogic, Z. Self-organized dynamics and the transition to turbulence of confined active nematics. *PNAS* **116,** 4788–4797 (2019).

58. Hardoüin, J., Hughes, R., Doostmohammadi, A., Laurent, J., Lopez-Leon, T., Yeomans, J. M., Ignés-Mullol, J. & Sagués, F. Reconfigurable flows and defect landscape of confined active nematics. *Communications Physics* **2,** 1–9 (2019).

59. Kempf, F., Mueller, R., Frey, E., Yeomans, J. M. & Doostmohammadi, A. Active matter invasion. *Soft matter* **15,** 7538 (2019).

60. Wioland, H., Woodhouse, F. G., Dunkel, J., Kessler, J. O. & Goldstein, R. E. Confinement stabilizes a bacterial suspension into a spiral vortex. *Phys. Rev. Lett.* **110,** 268102 (2013).

61. Doxzen, K., Vedula, S. K., Leong, M. C., Hirata, H., Gov, N. S., Kabla, A. J., Ladoux, B. & Lim, C. T. Guidance of collective cell migration by substrate geometry. *Integr. Biol.* **5,** 1026–1035 (2013).

62. Wu, K.-T., Hishamunda, J. B., Chen, D. T., DeCamp, S. J., Chang, Y.-W., Fernández-Nieves, A., Fraden, S. & Dogic, Z. Transition from turbulent to coherent flows in confined three-dimensional active fluids. *Science* **355,** eaal1979 (2017).

63. Čopar, S., Aplinc, J., Kos, Ž., Žumer, S. & Ravnik, M. Topology of three-dimensional active nematic turbulence confined to droplets. *Physical Review X* **9,** 031051 (2019).

64. Binysh, J., Kos, Ž., Čopar, S., Ravnik, M. & Alexander, G. P. Three-Dimensional Active Defect Loops. *Physical Review Letters* **124,** 088001 (2020).

65. Duclos, G., Adkins, R., Banerjee, D., Peterson, M. S., Varghese, M., Kolvin, I., Baskaran, A., Pelcovits, R. A., Powers, T. R., Baskaran, A., *et al.* Topological structure and dynamics of three-dimensional active nematics. *Science* **367,** 1120–1124 (2020).

66. Ruske, L. J. & Yeomans, J. M. Morphology of active deformable 3D droplets. *arXiv preprint arXiv:2010.10427* (2020).

67. Chandragiri, S., Doostmohammadi, A., Yeomans, J. M. & Thampi, S. P. Flow States and Transitions of an Active Nematic in a Three-Dimensional Channel. *Physical Review Letters* **125,** 148002 (2020).

68. Thampi, S. P., Golestanian, R. & Yeomans, J. M. Active nematic materials with substrate friction. *Phys. Rev. E* **90,** 062307 (6 2014).

69. Pearce, D. Activity driven orientational order in active nematic liquid crystals on an anisotropic substrate. *Phys. Rev. Lett.* **122,** 227801 (2019).

70. DeCamp, S. J., Redner, G. S., Baskaran, A., Hagan, M. & Dogic, Z. Orientational order of motile defects in active nematics. *Nat. Mat.* **14,** 1110–1115 (2015).

71. Reinken, H., Nishiguchi, D., Heidenreich, S., Sokolov, A., Bär, M., Klapp, S. H. & Aranson, I. S. Organizing bacterial vortex lattices by periodic obstacle arrays. *Communications Physics* **3,** 1–9 (2020).

72. Furter, M., Sellin, M. E., Hansson, G. C. & Hardt, W.-D. Mucus architecture and near-surface swimming affect distinct Salmonella Typhimurium infection patterns along the murine intestinal tract. *Cell Rep.* **27,** 2665–2678 (2019).

73. Figueroa-Morales, N., Dominguez-Rubio, L., Ott, T. L. & Aranson, I. S. Mechanical shear controls bacterial penetration in mucus. *Sci. Rep.* **9,** 1–10 (2019).

74. Ranjbaran, M., Solhtalab, M. & Datta, A. K. Mechanistic modeling of light-induced chemotactic infiltration of bacteria into leaf stomata. *PLoS Comput. Biol.* **16,** e1007841 (2020).

75. Moriarty, T., Norman, M. U., Colarusso, P., Bankhead, T., Kubes, P. & Chaconas, G. Real-time high resolution 3D imaging of the Lyme disease spirochete adhering to and escaping from the vasculature of a living host. *PLoS Pathog.* **4** (2008).

76. Zusman, D., Scott, A. E., Yang, Z. & Kirby, J. R. Chemosensory pathways, motility and development in Myxococcus xanthus. *Nat. Rev. Microbiol.* **5,** 862–872 (2007).

77. Lee, H. Y. & Kardar, M. Macroscopic equations for pattern formation in mixtures of microtubules and molecular motors. *Physical Review E* **64,** 056113 (2001).

78. Kruse, K., Joanny, J.-F., Jülicher, F., Prost, J. & Sekimoto, K. Asters, vortices, and rotating spirals in active gels of polar filaments. *Physical review letters* **92,** 078101 (2004).

79. Husain, K. & Rao, M. Emergent structures in an active polar fluid: Dynamics of shape, scattering, and merger. *Physical review letters* **118,** 078104 (2017).

80. Endresen, K. D., Kim, M. & Serra, F. Topological defects of integer charge in cell monolayers. *arXiv preprint arXiv:1912.03271* (2019).

81. Guillamat, P., Blanch-Mercader, C., Kruse, K. & Roux, A. Integer topological defects organize stresses driving tissue morphogenesis. *bioRxiv* (2020).

82. Turiv, T., Krieger, J., Babakhanova, G., Yu, H., Shiyanovskii, S. V., Wei, Q.-H., Kim, M.-H. & Lavrentovich, O. D. Topology control of human fibroblast cells monolayer by liquid crystal elastomer. *Science Advances* **6,** eaaz6485 (2020).

83. Rivas, D. P., Shendruk, T. N., Henry, R. R., Reich, D. H. & Leheny, R. L. Driven topological transitions in active nematic films. *Soft Matter* **16,** 9331–9338 (2020).

84. Pearce, D., Nambisan, J, Ellis, P., Dogic, Z, Fernandez-Nieves, A & Giomi, L. Scale-free defect ordering in passive and active nematics. *arXiv preprint arXiv:2004.13704* (2020).

85. Chandrasekhar, S, Sadashiva, B. & Suresh, K. Liquid crystals of disc-like molecules. *pramana* **9,** 471–480 (1977).

86. Liang, Q., Liu, P., Liu, C., Jian, X., Hong, D. & Li, Y. Synthesis and properties of lyotropic liquid crystalline copolyamides containing phthalazinone moiety and ether linkages. *Polymer* **46,** 6258–6265 (2005).

87. Reinitzer, F. Beiträge zur kenntniss des cholesterins. *Monatshefte für Chemie und verwandte Teile anderer Wissenschaften* **9,** 421–441 (1888).

88. Friedel, G. Les états mésomorphes de la matière. *AnPh* **9,** 273–474 (1922).

89. Onsager, L. The effects of shape on the interaction of colloidal particles. *Annals of the New York Academy of Sciences* **51,** 627–659 (1949).

90. Maier, W. & Saupe, A. Eine einfache molekulare Theorie des nematischen kristallinflüssigen Zustandes. *Zeitschrift für Naturforschung A* **13,** 564–566 (1958).

91. Landau, L. D. *Collected papers of LD Landau* (Pergamon, 1965).

92. Longa, L. & Tomczyk, W. Twist-bend nematic phase from Landau-de Gennes perspective. *arXiv preprint arXiv:2005.02455* (2020).

93. Vink, R. L. Crossover from a Kosterlitz-Thouless phase transition to a discontinuous phase transition in two-dimensional liquid crystals. *Physical Review E* **90,** 062132 (2014).

94. Matsuyama, A, Evans, R. & Cates, M. Non-uniformities in polymer/liquid crystal mixtures. *Eur. Phys. J. E.* **9,** 79–87 (2002).

95. Demus, D., Goodby, J. W., Gray, G. W., Spiess, H. W. & Vill, V. *Handbook of liquid crystals, volume 2A: low molecular weight liquid crystals I: calamitic liquid crystals* (John Wiley & Sons, 2011).

96. Schiele, K. & Trimper, S. On the elastic constants of a nematic liquid crystal. *Physica Sta. Solid.* **118,** 267–274 (1983).

97. Yamaguchi, H., Wyckoff, J. & Condeelis, J. Cell migration in tumors. *Current opinion in cell biology* **17,** 559–564 (2005).

98. Cahn, J. W. & Hilliard, J. E. Free energy of a nonuniform system. I. Interfacial free energy. *J. Chem. Phys.* **28,** 258–267 (1958).

99. Harth, K. & Stannarius, R. Topological Point Defects of Liquid Crystals in Quasi-Two-Dimensional Geometries. *Frontiers in Physics* **8,** 112 (2020).

100. Saupe, A. in *Plenary and Invited Lectures* 583–592 (Elsevier, 1977).

101. Beris, A. N. & Edwards, B. J. *Thermodynamics of Flowing Systems: With Internal Microstructure* (Oxford University Press, 1994).

102. Marenduzzo, D., Orlandini, E., Cates, M. E. & Yeomans, J. M. Steady-state hydrodynamic instabilities of active liquid crystals: Hybrid lattice Boltzmann simulations. *Phys. Rev. E* **76,** 031921 (2007).

103. Van Horn, B. L. & Winter, H. H. Dynamics of shear aligning of nematic liquid crystal monodomains. *Rheologica acta* **39,** 294–300 (2000).

104. Aigouy, B., Farhadifar, R., Staple, D. B., Sagner, A., Röper, J.-C., Jülicher, F. & Eaton, S. Cell flow reorients the axis of planar polarity in the wing epithelium of Drosophila. *Cell* **142,** 773–786 (2010).

105. Ericksen, J. Anisotropic fluids. *Rational Mech. Anal.* **4,** 231–237 (1960).

106. Ericksen, J. Inequalities in liquid crystal theory. *The Physics of Fluids* **9,** 1205–1207 (1966).

107. Leslie, F. M. Some constitutive equations for anisotropic fluids. *The Quarterly Journal of Mechanics and Applied Mathematics* **19,** 357–370 (1966).

108. Leslie, F. M. Some constitutive equations for liquid crystals. *Archive for Rational Mechanics and Analysis* **28,** 265–283 (1968).

109. Parodi, O. Stress tensor for a nematic liquid crystal. *Journal de Physique* **31,** 581–584 (1970).

110. Edwards, B. J., Beris, A. N. & Grmela, M. Generalized constitutive equation for polymeric liquid crystals Part 1. Model formulation using the Hamiltonian (poisson bracket) formulation. *Journal of non-newtonian fluid mechanics* **35,** 51–72 (1990).

111. Giomi, L., Mahadevan, L., Chakraborty, B. & Hagan, M. F. Excitable patterns in active nematics. *Phys. Rev. Lett.* **106,** 218101 (2011).

112. Krüger, T., Kusumaatmaja, H., Kuzmin, A., Shardt, O., Silva, G. & Viggen, E. M. The lattice Boltzmann method. *Springer International Publishing* **10,** 4–15 (2017).

113. Yeomans, J. M. The hydrodynamics of active systems. *La Rivista del Nuovo Cimento* **40,** 1–31 (2017).

114. Lighthill, M. On the squirming motion of nearly spherical deformable bodies through liquids at very small Reynolds numbers. *Communications on pure and applied mathematics* **5,** 109–118 (1952).

115. Riley, E. E., Das, D. & Lauga, E. Swimming of peritrichous bacteria is enabled by an elastohydrodynamic instability. *Scientific reports* **8,** 1–7 (2018).

116. Lauga, E. & Powers, T. R. The hydrodynamics of swimming microorganisms. *Reports on Progress in Physics* **72,** 096601 (2009).

117. Thampi, S. P., Doostmohammadi, A., Golestanian, R. & Yeomans, J. M. Intrinsic free energy in active nematics. *Eur. Phys. Lett.* **112,** 28004 (2015).

118. Nejad, M. R., Doostmohammadi, A. & Yeomans, J. Memory effects, arches and polar defect ordering at the cross-over from wet to dry active nematics. *Soft Matter* (2021).

119. Di Leonardo, R, Keen, S, Ianni, F, Leach, J, Padgett, M. & Ruocco, G. Hydrodynamic interactions in two dimensions. *Physical Review E* **78,** 031406 (2008).

120. Shankar, S., Ramaswamy, S., Marchetti, M. C. & Bowick, M. J. Defect unbinding in active nematics. *Physical review letters* **121,** 108002 (2018).

121. Meneveau, C. & Katz, J. Scale-invariance and turbulence models for large-eddy simulation. *Annual Review of Fluid Mechanics* **32,** 1–32 (2000).

122. Thampi, S. P., Golestanian, R. & Yeomans, J. M. Instabilities and topological defects in active nematics. *EPL (Europhysics Letters)* **105,** 18001 (2014).

123. Blow, M. L., Thampi, S. P. & Yeomans, J. M. Biphasic, lyotropic, active nematics. *Physical review letters* **113,** 248303 (2014).

124. Hobdell, J. & Windle, A. A numerical technique for predicting microstructure in liquid crystalline polymers. *Liquid crystals* **23,** 157–173 (1997).

125. Chandrasekhar, S. *Liquid Crystals* (Cambridge University Press, 1980).

126. Oswald, P. & Pieranski, P. *Nematic and cholesteric liquid crystals: Concepts and physical properties illustrated by experiments* (CRC Press, 2005).

127. Čopar, S., Porenta, T. & Žumer, S. Visualisation methods for complex nematic fields. *Liquid Crystals* **40,** 1759–1768 (2013).

128. Doostmohammadi, A. & Yeomans, J. M. Coherent motion of dense active matter. *Eur. Phys. J. Spec. Top.* **227,** 2401–2411 (2019).

129. Oza, A. U. & Dunkel, J. Antipolar ordering of topological defects in active liquid crystals. *New Journal of Physics* **18,** 093006 (2016).

130. Lubensky, D. K. & Goldstein, R. E. Hydrodynamics of monolayer domains at the air–water interface. *Physics of fluids* **8,** 843–854 (1996).

131. Putzig, E., Redner, G. S., Baskaran, A. & Baskaran, A. Instabilities, defects, and defect ordering in an overdamped active nematic. *Soft Matter* **12,** 3854–3859 (2016).

132. Shankar, S. & Marchetti, M. C. Hydrodynamics of Active Defects: from order to chaos to defect ordering. *Phys. Rev. X* **9,** 041047 (2019).

133. Thijssen, K., Nejad, M. R. & Yeomans, J. M. Role of Friction in Multidefect Ordering. *Physical Review Letters* **125,** 218004 (2020).

134. Srivastava, P., Mishra, P. & Marchetti, M. C. Negative stiffness and modulated states in active nematics. *Soft Matter* **12,** 8214–8225 (2016).

135. Santhosh, S., Nejad, M. R., Doostmohammadi, A., Yeomans, J. M. & Thampi, S. P. Activity induced nematic order in isotropic liquid crystals. *Journal of Statistical Physics,* 1–11 (2020).

136. Chandragiri, S., Doostmohammadi, A., Yeomans, J. M. & Thampi, S. P. Active transport in a channel: stabilisation by flow or thermodynamics. *Soft matter* **15,** 1597–1604 (2019).

137. Vafa, F., Bowick, M. J., Marchetti, M. C. & Shraiman, B. I. Multi-defect dynamics in active nematics. *arXiv preprint arXiv:2007.02947* (2020).

138. Patelli, A., Djafer-Cherif, I., Aranson, I. S., Bertin, E. & Chaté, H. Understanding dense active nematics from microscopic models. *Phys. Rev. Lett.* **123,** 258001 (2019).

139. Vromans, A. J. & Giomi, L. Orientational properties of nematic disclinations. *Soft matter* **12,** 6490–6495 (2016).

140. Tang, X. & Selinger, J. V. Orientation of topological defects in 2D nematic liquid crystals. *Soft Matter* **13,** 5481–5490 (2017).

141. Ginelli, F., Peruani, F., Bär, M. & Chaté, H. Large-Scale Collective Properties of Self-Propelled Rods. *Phys. Rev. Lett.* **104,** 184502 (18 2010).

142. Bertin, E., Baskaran, A., Chaté, H. & Marchetti, M. C. Comparison between Smoluchowski and Boltzmann approaches for self-propelled rods. *Phys. Rev. E* **92,** 042141 (2015).

143. Van Damme, R., Rodenburg, J., van Roij, R. & Dijkstra, M. Interparticle torques suppress motility-induced phase separation for rodlike particles. *The Journal of Chemical Physics* **150,** 164501 (2019).

144. Nagel, A. M., Greenberg, M., Shendruk, T. N. & de Haan, H. W. Collective dynamics of model pili-based twitcher-mode Bacilliforms. *Scientific Reports* **10,** 1–16 (2020).

145. Chaté, H. Dry Aligning Dilute Active Matter. *Annual Review of Condensed Matter Physics* **11,** 189–212 (2020).

146. Bär, M., Großmann, R., Heidenreich, S. & Peruani, F. Self-Propelled Rods: Insights and Perspectives for Active Matter. *Annual Review of Condensed Matter Physics* **11,** 441–466 (2020).

147. Galajda, P., Keymer, J., Chaikin, P. & Austin, R. A wall of funnels concentrates swimming bacteria. *J. Bacteriol.* **189,** 8704–8707 (2007).

148. Mahmud, G., Campbell, C. J., Bishop, K. J. M., Komarova, Y. A., Chaga, O., Soh, S., Huda, S., Kandere-Grzybowska, K. & Grzybowski, B. A. Directing cell motions on micropatterned ratchets. *Nat. Phys.* **5,** 606–612 (2009).

149. Katuri, J., Caballero, D., Voituriez, R., Samitier, J. & Sanchez, S. Directed Flow of Micromotors through Alignment Interactions with Micropatterned Ratchets. *ACS Nano* **12,** 7282–7291 (2018).

150. Angelani, L., Di Leonardo, R. & Ruocco, G. Self-Starting Micromotors in a Bacterial Bath. *Phys. Rev. Lett.* **102,** 048104 (2009).

151. Sokolov, A., Apodaca, M. M., Grzybowski, B. A. & Aranson, I. S. Swimming bacteria power microscopic gears. *PNAS* **107,** 969–974 (2010).

152. Pietzonka, P., Fodor, E., Lohrmann, C., Cates, M. E. & Seifert, U. Autonomous Engines Driven by Active Matter: Energetics and Design Principles. *Phys. Rev. X* **9,** 041032 (2019).

153. Sunyer, R., Conte, V., Escribano, J., Elosegui-Artola, A., Labernadie, A., Valon, L., Navajas, D., García-Aznar, J. M., Muñoz, J. J., Roca-Cusachs, P. & Trepat, X. Collective cell durotaxis emerges from long-range intercellular force transmission. *Science* **353,** 1157–1161 (2016).

154. DuChez, B. J., Doyle, A. D., Dimitriadis, E. K. & Yamada, K. M. Durotaxis by Human Cancer Cells. *Biophysical Journal* **116,** 670 –683 (2019).

155. Sunyer, R. & Trepat, X. Durotaxis. *Current Biology* **30,** R383–R387 (2020).

156. Row, H. & Brady, J. F. Reverse osmotic effect in active matter. *Phys. Rev. E* **101,** 062604 (2020).

157. Pismen, L. M. & Sagués, F. Viscous dissipation and dynamics of defects in an active nematic interface. *The European Physical Journal E* **40,** 92 (2017).

158. Zhou, Z., Joshi, C., Liu, R., Norton, M. M., Lemma, L., Dogic, Z., Hagan, M. F., Fraden, S. & Hong, P. Machine learning forecasting of active nematics. *Soft Matter,* – (2020).

159. Zhang, R., Redford, S. A., Ruijgrok, P. V., Kumar, N., Mozaffari, A., Zemsky, S., Dinner, A. R., Vitelli, V., Bryant, Z., Gardel, M. L., *et al.* Structuring Stress for Active Materials Control. *arXiv preprint arXiv:1912.01630* (2019).

160. Fielding, S. M., Marenduzzo, D. & Cates, M. E. Nonlinear dynamics and rheology of active fluids: Simulations in two dimensions. *Phys. Rev. E* **83,** 041910 (2011).

161. Zhang, B., Hilton, B., Short, C., Souslov, A. & Snezhko, A. Oscillatory chiral flows in confined active fluids with obstacles. *Phys. Rev. Research* **2,** 043225 (2020).

162. Guillamat, P., Ignés-Mullol, J., Shankar, S., Marchetti, M. C. & Sagués, F. Probing the shear viscosity of an active nematic film. *Physical review E* **94,** 060602 (2016).

163. Sokolov, A., Mozaffari, A., Zhang, R., de Pablo, J. J. & Snezhko, A. Emergence of Radial Tree of Bend Stripes in Active Nematics. *Phys. Rev. X* **9,** 031014 (2019).

164. Godeau, A. L., Leoni, M., Comelles, J., Delanoe-Ayari, H., Ott, A., Harlepp, S., Sens, P. & Riveline, D. A scallop theorem for cells moving in 3D. *bioRxiv* (2020).

165. Mathijssen, A. J., Jeanneret, R. & Polin, M. Universal entrainment mechanism controls contact times with motile cells. *Physical Review Fluids* **3,** 033103 (2018).

166. Kaiser, A. & Löwen, H. Unusual swelling of a polymer in a bacterial bath. *The Journal of chemical physics* **141,** 044903 (2014).

167. Foffano, G, Lintuvuori, J., Stratford, K, Cates, M. & Marenduzzo, D. Colloids in active fluids: Anomalous microrheology and negative drag. *Physical review letters* **109,** 028103 (2012).

168. Marenduzzo, D., Orlandini, E. & Yeomans, J. M. Hydrodynamics and Rheology of Active Liquid Crystals: A Numerical Investigation. *Phys. Rev. Lett.* **98,** 118102 (2007).

169. Guo, Z., Zheng, C. & Shi, B. Discrete lattice effects on the forcing term in the lattice Boltzmann method. *Phys. Rev. E* **65,** 046308 (2002).

170. DeVries, P. L. & Wolf, R. P. A first course in computational physics. *Computers in Physics* **8,** 178–179 (1994).

171. Denniston, C., Orlandini, E. & Yeomans, J. M. Lattice Boltzmann simulations of liquid crystal hydrodynamics. *Phys. Rev. E* **63,** 056702 (2001).

172. Mottram, N. J. & Newton, C. J. P. Introduction to Q-tensor theory. *arXiv:1409.3542* (2014).

173. Hatwalne, Y., Ramaswamy, S., Rao, M. & Simha, R. A. Rheology of active-particle suspensions. *Physical review letters* **92,** 118101 (2004).